The visible rovibrational spectrum of the triatomic hydrogen ion via high-sensitivity chemical reaction spectroscopy in a cryogenic ion trap

Inaugural-Dissertation
zur
Erlangung des Doktorgrades
der Mathematisch-Naturwissenschaftlichen Fakultät
der Universität zu Köln
vorgelegt von

Max H. Berg
aus Mannheim

Heidelberg
2011

Berichterstatter: **Prof. Dr. Stephan Schlemmer**
(Gutachter) **Prof. Dr. Detlev Gotta**
Prof. Dr. Andreas Wolf

Tag der mündlichen Prüfung: 31.01.2011

Abstract

H_3^+ is the cornerstone of the interstellar chemistry and the dominant molecular ion in most hydrogen plasmas, natural or artifical. It is the simplest polyatomic molecule and therefore the perfect benchmark system for dedicated quantum mechanical calculations on polyatomic molecules, provided that relevant experimental data is available. The thesis at hand presents results of the visible rovibrational spectroscopy of the H_3^+ ion. First transitions far into the visible spectral region, almost reaching final levels half the way to dissociation, are reported. These highly excited final rovibrational levels, containing up to 9 vibrational quanta, are up to 6 orders of magnitude weaker than the ν_2 fundamental transition. Furthermore, first experimental Einstein B_{lu} coefficients for transitions from the cold lower levels to final levels above the barrier to linearity are reported. The experiments are performed in a cryogenic 22-pole trap where the H_3^+ ions are buffer-gas cooled by helium. The narrow initial rotational population allows for normalization and unique assignment of nearly all transitions. Laser-induced reactions with Ar, providing high sensitivity, are then used to measure the extremely weak transitions. The found transition frequencies provide benchmark data and have already led to an improvement in calculated energy levels. The obtained intensities agree well with the bulk transitions. However, they do not support the predicted high-intensities of the so-called horseshoe states, which in calculations are found to be localized in the otherwise highly chaotic excited region of H_3^+. The sensitivity limit of the spectroscopy technique has not yet been reached and investigation of states up to the dissociation limit may be possible.

Kurzfassung

H_3^+ ist ein Eckpfeiler der interstellaren Chemie und das dominante Ion in den meisten natürlichen oder künstlichen Wasserstoffplasmen. Da es das einfachste mehratomige Molekülion ist, dient es als Referenz für quantenmechanische Berechnungen mehratomiger Moleküle, sofern die entsprechenden, aus Experimenten gewonnenen Daten zur Verfügung stehen. Die hier vorliegende Arbeit stellt Ergebnisse der Vibrations-Rotations-Spektroskopie von H_3^+ im sichtbaren Spektralbereich vor. Erstmals wurden Übergänge zu Energieniveaus knapp unterhalb der halben Dissoziationsenergie gemessen. Diese hochangeregten Zustände, deren Übergangswahrscheinlichkeiten bis zu 6 Größenordnungen kleiner als die der ν_2-Grundschwingung sind, besitzen bis zu 9 Vibrationsquanten. Des Weiteren werden erste experimentell bestimmte Einstein B_{lu} Koeffizienten für Übergänge ausgehend von den Grundzuständen zu Zuständen oberhalb der "Linearitätsbarriere" vorgestellt. Die Messungen wurden in einer kryogenen 22-Pol-Falle, in der die H_3^+-Ionen mit Helium als Puffergas gekühlt werden, durchgeführt. Die wohldefinierte Population

der Rotationsniveaus im Ausgangszustand ermöglicht die eindeutige Zuordnung und das Normalisieren der Übergänge. Die sehr schwachen Übergänge werden anhand der äußerst empfindlichen Methode der laserinduzierten Reaktion nachgewiesen. Die gemessenen Übergangsfrequenzen bieten Referenzwerte, anhand derer bereits vorhergesagte Zustandsberechnungen verbessert wurden. Für die meisten Übergänge stimmen die gemessenen Übergangsstärken mit den theoretischen Vorhersagen überein. Die prognostizierten starken Intensitäten für die sogenannten "horseshoe" Übergänge wurden experimentell nicht bestätigt. Die Nachweisgrenze dieser Spektroskopiemethode ist noch nicht erreicht und die Untersuchung von Zuständen bis hin zur Dissoziationsgrenze scheint möglich.

Contents

1. Introduction

Spectroscopy is arguably the most important tool for gaining knowledge on the nature of atoms and molecules. During the 20th century a wealth of detailed intrinsic information about molecular structure and molecular dynamics has been revealed, honored by more than ten Nobel prizes. For the 21st century, ongoing developments of spectroscopic techniques along with improving theoretical calculations provide further insights in a way only spectroscopy can do [1].

This work is dedicated to the spectroscopy of H_3^+, an extraordinary jewel of nature, detected 100 years ago [2, 3]. An extensive source of information on H_3^+ can be found in the papers of the two discussion meetings of the Royal Society [4, 5]. After H_2, the triatomic molecular ion, H_3^+ is the second most abundantly formed interstellar molecule. It is also the dominant ion in any technical hydrogen plasma. Due to the low proton affinity of H_2, H_3^+ is the universal proton donor and therefore a key ion for the interstellar chemistry paving the way to form more complex molecules. These days, important insights on physical and chemical properties of interstellar objects are obtained by "astronomical" spectroscopy of H_3^+. Besides its astronomical impact, H_3^+ is the simplest stable polyatomic molecule consisting of three protons bound by two de-localized electrons. Therefore, H_3^+ is the polyatomic benchmark molecule against which theoretical calculations are tested, comparable to the hydrogen atom for general atomic theory. The theoretical treatment for small molecules near their equilibrium structure is qualitatively in terms of simple models and quantitatively via variational calculations well understood and achieves near spectroscopic accuracy for H_3^+. For higher energies far away from equilibrium up to dissociation the theoretical treatment is much more incomplete and here H_3^+ is a test system for the development of adequate, non-standard theoretical and numerical methods to account for adiabatic as well as non-adiabatic effects beyond the Born-Oppenheimer approximation. As there is no direct way of obtaining an

analytical expression for a potential energy surface (PES) from measured transition frequencies, only a strong interplay between theory and experiment can reveal the truth. The interactive process is the following: Theory provides transition frequencies and intensities from a reasonably assumed PES and dipole surface in known energy regions. Experiment can use these predictions to obtain measured transition frequencies and intensities, that in turn are used as input to extend the theoretical calculation to higher energies. Until recently the experimental side could not fulfill its duties to provide information on very weak transitions with the final level lying high in energy, and therefore since more than one decade only various theoretical results could be compared to each other. Here an experiment that can provide all the information theoreticians have been waiting for a long time is introduced. This work already initiated further theoretical studies [6]. For the first time high resolution and high sensitivity spectroscopic data for a polyatomic molecule half the way up to dissociation threshold is presented. The remarkable possibility to measure transition intensities allows to examine so-called horseshoe states and thereby to provide further insights into the outstanding Carrington pre-dissociation spectrum, one of the longest running problems in chemical physics. The knowledge of high-lying energy levels also provides interesting methods for *in-situ* diagnostics in storage ring experiments.

This thesis is divided into three parts. Part I "Motivation & Theory" introduces the triatomic molecular hydrogen ion H_3^+ in a brief historical review. The main theoretical aspects for this particular ion as well as the pivotal role in space and the outstanding rich pre-dissociation spectrum of H_3^+ are introduced. A rough overview on theoretical calculation methods for polyatomic molecules is depicted and the role of H_3^+ as a benchmark ion is enlighted. Part II "Experimental Setup & Measurement Technique introduces the experimental setup and describes the high-sensitivity chemical reaction spectroscopy technique. Improvements on the setup implemented during this thesis are also given. The last part presents the results from transition frequency and transition intensity measurements. The thesis closes with a conclusion and presents some perspectives on future work.

Part I.

Motivation & Theory

2. Triatomic hydrogen H_3^+

This chapter is dedicated to introduce the amazing triatomic hydrogen ion H_3^+, a little molecular ion with big impact in science. A Google scholar abstracts search reveals more than 250 publications in the past 10 years alone. The low terrestrial abundance results from the exceptional reactivity of this particular ion. In extraterrestrial hydrogen environments H_3^+ is quite common and plays a central role in the interstellar chemistry. At first, a short historical overview on H_3^+ is given. Afterwards, the theoretical background is presented. Selection rules and quantum numbers are provided, followed by highlighting the key role of H_3^+ with respect to the interstellar medium. A summary of the extraordinary pre-dissociation spectrum of H_3^+ is given and some attempts to explain this rich spectrum are depicted.

2.1. A brief history

In 1911, J. J. Thomson, the pioneer of early mass spectroscopy, measured during his study on “Rays of Positive Electricity" an ion with mass-to-charge ratio of 3:1 in a hydrogen discharge (see Fig. 2.1) [2]. However, as at that time H was known to be monovalent, the first denotation as H_3^+ was only published one year later, after excluding all other possibilities [3]. Further studies on hydrogen discharges revealed that H_3^+, as pressure increases, becomes the dominant ion in preference to either H^+

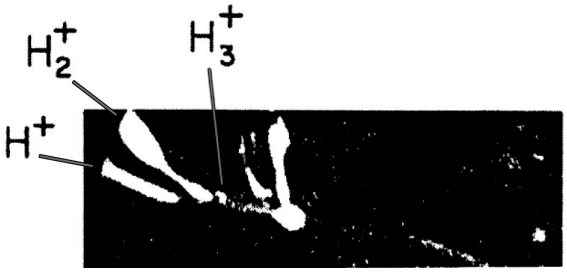

Figure 2.1 – A photograph from J. J. Thomson's work showing H^+ and H_2^+ together with H_3^+

or H_2^+ [7]. More than ten years later T. R. Hogness and E. G. Lunn [8] suggested the formation of H_3^+ via

$$H_2 + H_2^+ \rightarrow H_3^+ + H, \tag{2.1}$$

at that time the first ion-molecule reaction that proceeds with a large Langevin rate ($\sim 10^{-9}\,\mathrm{cm}^{-3}\,\mathrm{s}^{-1}$). After the discovery of deuterium in 1931 by H. C. Urey [9] many people, including J. J. Thomson [10], ascribed the former observations [2] to HD^+. The original H_3^+ assignment was only accepted again in the late 30's when theory made its first important contribution and Hirschfelder and co-authors showed in a series of five papers that H_3^+ is indeed a stable species (later calculations show that H_3^+ is even more stably bound than H_2 by 0.3 eV) [11, 12, 13, 14, 15]. The determination of the equilibrium structure was not possible at that time, changing between linear and some triangular shape from publication to publication. From a todays point of view the difficulties in determining the equilibrium structure are understandable as the potential energy surface for the ion is now known to be rather flat. For more than another 30 years the only thing that was known for sure on H_3^+ was its mere existence.

The expectation to detect H_3^+ in space as the most stable ionic form of hydrogen was stated in a short note from D. W. Martin *et al.* in 1961 [16]. Theoretical understanding in terms of symmetry properties and the development of a classification system of the energy levels is owed to the work of J. T. Hougen and J. K. G. Watson [17, 18, 19]. In 1964, R. E. Christofferson *et al.* succeeded in determining the equilibrium structure from *ab initio* calculations using an electronic computer [20]. The bonding can be regarded as similar to that of benzene. The two electrons can be considered to be delocalized across the three protons, resulting in an equilateral triangular equilibrium shape. At equilibrium, the three protons are separated by $1.65\,a_0$. This was experimentally confirmed in 1978 by Gaillard using the Coulomb explosion technique [21]. The most precise experimental value for the binding energy of H_3^+ is 4.337 eV [22]. Calculations show that H_3^+ does not have any stable excited electronic states except for a very shallow triplet state leading to the H_2^+ + H dissociation limit which is only 0.4 eV higher.

In 1976, G. D. Carney and R. N. Porter published a detailed *ab initio* prediction of the H_3^+ spectrum [23]. With these predictions at hand, T. Oka published, after four and a half years of search, in 1980 the first spectrum of H_3^+ [24]. From there on,

the interplay between theory and experiment began. W. Meyer, P. Botschwina, and P. Burton published a potential, which after a small scaling correction to match the observed ν_2 band origin, provides accurate values for the first few excited vibrational states of H_3^+ [25]. These calculated values proved to be helpful for the laboratory work on hot bands[1] [26], overtone bands [27], and forbidden transitions [28]. Up to 2001, in total 17 studies were conducted, revealing 895 observed transitions with frequencies as high as 8170 cm^{-1} well below the so-called barrier to linearity (see Sec. 2.2.1) [29]. Ongoing efforts from theoreticians and experimentalists led to the observation of the first transition to final levels above the barrier to linearity in a discharge tube experiment by J. Gottfried *et al.* in 2003 [30]. Since then, one further discharge tube experiment has been published [31]. In 2008, the first experiments with chemical probing spectroscopy reaching final levels between 11 200-13 400 cm^{-1}, well above the barrier to linearity, were published [32]. In App. B and App. C a comprehensive list of experiments on H_3^+ and an overview on the theoretical work considering this ion is given in Tab. B.1 and Tab. C respectively.

2.2. Theoretical background

As the equilibrium geometry of H_3^+ in its electronic ground state ($^1A_1'$) is an equilateral triangle, it belongs to the D_{3h} point group. The character and multiplication table for this symmetry group is given in App. D.

In Fig. 2.2 an overview on significant energies of H_3^+ is given. The zero-point of the energy scale is set according to the lowest allowed rovibronic state of H_3^+, which is $\sim$ 4426 cm^{-1} above the potential minimum. Around 10000 cm^{-1}, the barrier to linearity (see Sec. 2.2.1) is indicated and shortly above the sensitivity limit for traditional absorption spectroscopy is reached. Chemical probing spectroscopy, as described in Chap. 5, allows for investigation of energy levels above $\sim$ 4500 cm^{-1}, the upper limit not yet determined. The dissociation threshold into H_2 (v=0,J=0)+H^+ lies at 34955 cm^{-1}. The electronically excited triplet state and its dissociation channel H_2^+ ($v = 0, J = 0$)+H is also plotted.

[1] Explanation of vibration transitions types is given in App. A.

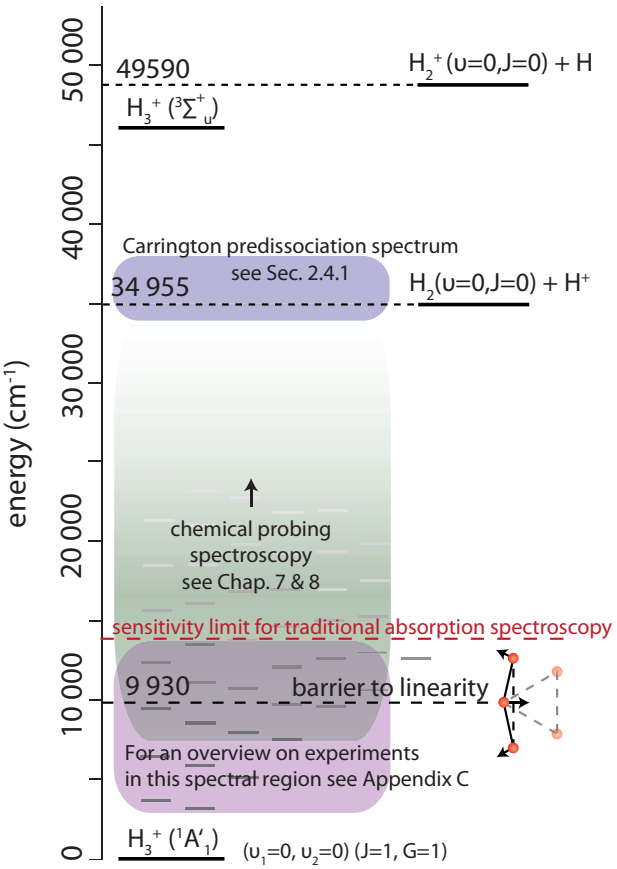

Figure 2.2 – Significant energy levels of H_3^+. The zero point of energy is set according to the lowest allowed state (J=1, G=1) of H_3^+, roughly 4426 cm^{-1} above the potential minimum (vibrational zero point energy is at ∼4362 cm^{-1}, slightly higher than $1/2(\nu_1 + 2\nu_2)$ indicating the large anharmonicity of the PES and ∼64 cm^{-1} as the J=0 rotational state is symmetry forbidden).

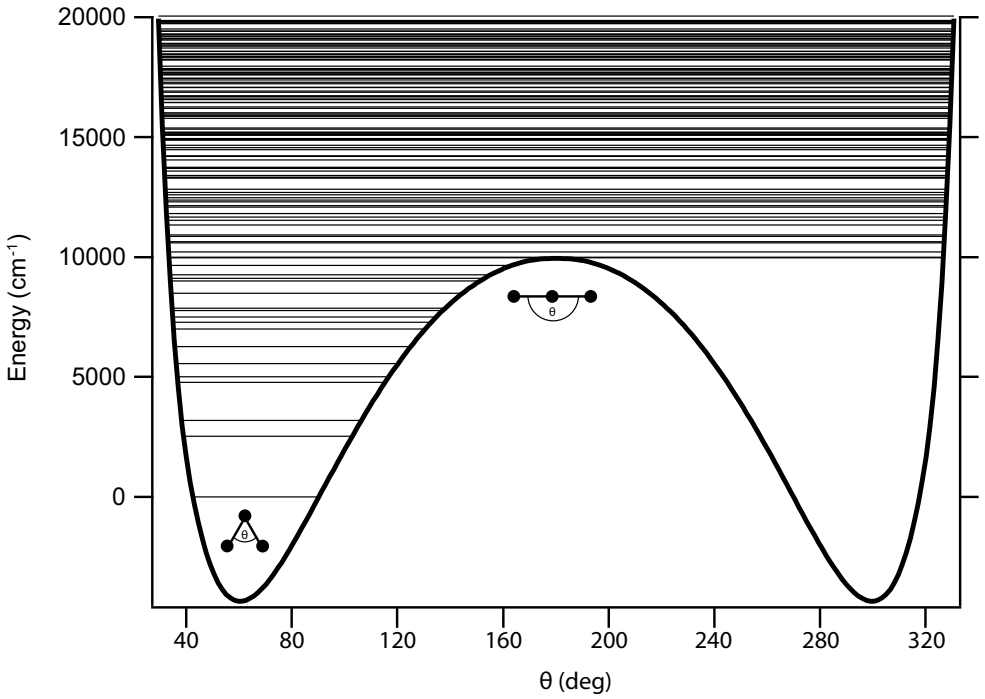

Figure 2.3. – Special one dimensional representation of the PES of H_3^+ along with band origins [34]. For any given angle the two H-H bond lengths are equally varied to obtain the minimum energy.

2.2.1. The barrier to linearity

In Fig. 2.3 a one dimensional representation of the PES, where two of the H-H bonds are forced to be equal but varied in length to minimize the energy at any given angle θ, is shown [33]. The barrier to linearity of H_3^+ lies near $10\,000\,\mathrm{cm}^{-1}$. Not regarding tunneling below this energy, the vibrational motion samples only "half" of the PES. Above the barrier to linearity the molecule possesses enough energy to sample linear geometries and can access the whole PES. For theoretical methods, that numerically calculate the matrix elements of the Hamiltonian, the ability of H_3^+ to sample linear configurations causes serious problems as there is a singularity in the kinetic energy operator at linearity. A simple work-around is to place an artificial wall in the potential and force the wave functions to vanish at linearity. The so obtained results can be used regarding energy levels well below the barrier to linearity. For higher energies the results poorly reflect the true nature. To obtain information on states above $10\,000\,\mathrm{cm}^{-1}$ more sophisticated methods, that use a basis set for which the

integrals over the singular term in the Hamiltonian can be calculated analytically, are needed. J. Tennyson *et al.* [35] implements such an approach and therefore the calculations of Neale, Miller, and Tennyson are also valid above the barrier to linearity. Another approach to circumvent the problem is to employ hyperspherical coordinates as A. Alijah does in his calculations [36].

2.2.2. Rotational spectrum

H_3^+ has a high symmetry, which has a number of consequences for its spectrum. The most evident one is the lack of a permanent dipole moment, i.e. H_3^+ has no ordinary pure rotational spectrum. However, Pan and Oka's [37] phenomenological-based and Miller and Tennyson's [38] ab initio calculations predict the existence of an observable "forbidden" rotational spectrum. In a classical picture, the centrifugal distortion caused by the rotation of the molecule leads to a temporary formation of a dipole moment, with the resulting intensity strongly depending on the amount of rotational excitation. Up until now, there exists no experimental confirmation of this rotational spectrum and rotational spectroscopy is not a convenient method to investigate H_3^+.

2.2.3. Electronic spectrum

The first electronically excited state is a triplet state ($^3\Sigma_u^+$) lying above the dissociation threshold $H_3^+ \rightarrow H_2 + H^+$ leading to the dissociation channel $H_3^+ \rightarrow H_2^+ + H$ (see Fig. 2.2). Symmetry restrictions prohibit the triplet state to access the lower dissociation pathway. Moreover, recent calculations show that although shallow (potential depth $0.37\,\mathrm{eV}/2951\,\mathrm{cm}^{-1}$), the potential surface can support a single vibrational excitation (zero point energy $0.21\,\mathrm{eV}/1722\,\mathrm{cm}^{-1}$). As consequence a hypothetical electronic spectrum of H_3^+ will lie in the deep ultraviolet spectral region and be extremely weak due to the singlet-triplet nature of the transition and the unfavorable Franck-Condon overlap. In addition, it might be broadened by predissociation. Electronic spectroscopy is therefore not a convenient method to investigate H_3^+ either.

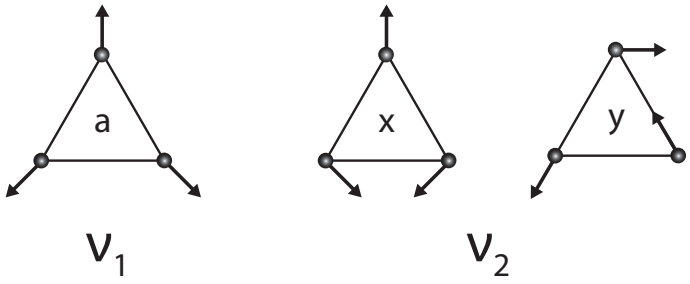

Figure 2.5. – H_3^+ normal modes

2.2.4. Rovibrational spectrum

Vibrational modes

A molecule with N nuclei has $3N$ nuclear coordinates to describe their positions in space. Three coordinates are chosen to define the center of mass and, for a non-linear molecule, three more describe the rotation of the molecular frame with respect to a space-fixed coordinate system. The remaining $3N-6$ coordinates describe the internal (vibrational) motion. H_3^+ possesses $3\cdot3-6=3$ internal coordinates which may be described by r_1, r_2 and r_3 as depicted in Fig. 2.4, with r_1 being the distance between proton 2 and 3, r_2 that between 1 and 3, and r_3 that between 1 and 2. Any combination of these three internal coordinates could be taken; however, vibrational modes are best described in normal coordinates that diagonalize the Hamiltonian operator and therefore decouple the vibrations. A normal-mode analysis results in two possible unique vibrational modes [39]. The first unique mode is the totally symmetric (A_1') and Raman active breathing mode ν_1, where the molecule expands and contracts as an equilateral triangle (see Fig. 2.5). In symmetry adapted deformation coordinates this mode is conventionally described as [40]

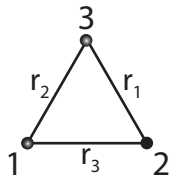

Figure 2.4.

$$s_a = \frac{1}{\sqrt{3}}(r_1 + r_2 + r_3). \tag{2.2}$$

The two vibrational modes described by

$$s_x = \frac{1}{\sqrt{6}}(2r_3 - r_1 - r_2) \tag{2.3}$$

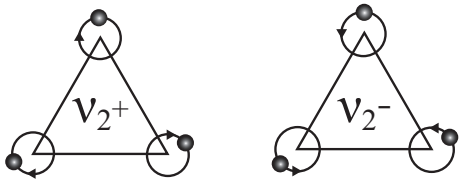

Figure 2.6. – Vibrational angular momentum

$$s_y = \frac{1}{\sqrt{2}}(r_1 - r_2) \tag{2.4}$$

form the asymmetric unique doubly degenerate bending mode ν_2. The deformation of the equilateral triangular shape by the ν_2 mode gives rise to a temporary formation of a dipole moment, making it infrared active. This is the basis for rovibrational spectroscopy of H_3^+.

Any linear combination of the two components ν_2 is possible and possesses vibrational angular momentum such as in any degenerate vibrational mode [41]. Figure 2.6 shows two combinations of s_x with s_y out of phase by $+90°$ (ν_2^+) and -90° (ν_2^-) where the circular motion of the nuclei clearly leads to angular momentum.

Quantum numbers

For any molecule, the total angular momentum ($F = J + I$) as well as the parity ($\pm$) are good quantum numbers as they depend on the isotropy and inversion symmetry of space rather than on molecular properties. The hyperfine interaction that couples the motional angular momentum J and the nuclear spin angular momentum I is very weak for H_3^+ and therefore to a good approximation I and J can be regarded as independent good quantum numbers. The quantum numbers I and J remain good quantum numbers even for energies far above the equilibrium state. Because the Hamiltonian is invariant to permutation of the three identical nuclei, symmetry labels for vibration-rotation wave functions are also good quantum numbers.

Additionally, approximate spectroscopic quantum numbers may be used at low to intermediate energies (up to $\sim$18000 cm^{-1}). These approximate good quantum numbers have been introduced to describe molecules close to their equilibrium geometry. They are based on the assumption that at sufficiently low energies the vibrations can be described by small harmonic displacements from this equilibrium geometry and that in a first approximation a separation between vibrational and

rotational motions can be made. H_3^+ exhibits a strong anharmonicity, even near the equilibrium geometry, as proven by the existence of intense overtones (for a harmonic potential there would be no intensity in overtones). Still, the spectroscopic approximate quantum numbers can be used.

The quantum numbers v_1 and v_2 denote the number of quanta in the ν_1 and ν_2 vibrational modes. The v_2 quantum number is complemented with its corresponding vibrational angular momentum quantum number l_2 (l_2=v_2,v_2-2,...,$-v_2$), which is strongly coupled to the rotation of the molecule. In contrast to most other molecules, neither the projection k of J onto the molecular symmetry axis nor l_2, also a projection along the same axis, are good quantum numbers. Therefore Hougen introduced $G = |g| = |k - l_2|$, representing the component of the projection of J onto the molecular axis that is due to rotation of the molecular frame only [17].

Nuclear Spin effect

Protons are fermions with spin $I = 1/2$ and so the H_3^+ molecule obeys the Fermi-Dirac statistic. Two possible spin combinations are the quadruply degenerate ortho state $I = 3/2$ with A_1' symmetry and the doubly degenerate para state $I = 1/2$ having E' symmetry. According to the Pauli principle the complete wave function must change its sign under the odd permutations of the nuclei (12),(23),(31) and it must be invariant to the even permutations (123) and (132). Appendix D lists the symmetry considerations relevant to H_3^+. From the character table Tab. D.1 it follows that the complete wave function of H_3^+ can only have the symmetries A_2' and A_2''. The possible combinations of rovibronic wave functions and nuclear spin are listed in Tab. D.3. As the electronic ground state of H_3^+ is totally symmetric (A_1' symmetry), rovibrational levels with A_1' symmetry (J even, G=0) are not allowed. Therefore the $J = G = 0$ level in the vibrational ground state is non-existent. Experimental observation of a gap ($> 100\,\mathrm{cm}^{-1}$) in the fundamental ν_2 spectrum is a clear evidence of the missing $J = G = 0$ state and therefore a proof for the equilateral shape of H_3^+.

Selection rules

To calculate the intensities in a molecular spectrum one needs the line strengths. The line strength of an electric dipole transition between the rovibronic state Φ'_{rve}, where rve stands for any rovibrational electronic state in general, having energy E'_{rve} and the state Φ''_{rve} having energy E''_{rve} is given by

$$S(f \leftarrow i) = \sum_{\Phi'_{rve},\Phi''_{rve}} \sum_{A=X,Y,Z} \left| \int \Phi'^{*}_{rve}\, \mu_A\, \Phi''_{rve} d\tau \right|^2, \tag{2.5}$$

where μ_A is the component of the molecular electric dipole moment along the A axis and $d\tau$ is the volume element for integration over the internal coordinate space of all particles of the molecule (electrons and nuclei). The sum over Φ'_{rve} and Φ''_{rve} accounts for possible degeneracies. To simplify the calculations and to determine selection rules for molecular transitions, the vanishing integral rule for integrals (I) of the form

$$I = \int \Psi'^{*}\, \hat{O}\, \Psi'' d\tau, \tag{2.6}$$

can be used, where Ψ', Ψ'' are wave functions and $\hat{O}$ is an operator [42]. The integral will vanish if the product of the symmetry species of Ψ'^{*}, $\hat{O}$, and Ψ'' does not contain the totally symmetric symmetry species $\Gamma^{(s)}$

$$I = \int \Psi'^{*}\, \hat{O}\, \Psi'' d\tau = 0 \qquad \text{if } \Gamma(\Psi'^{*}) \otimes \Gamma(\hat{O}) \otimes \Gamma(\Psi'') \not\supset \Gamma^{(s)} \tag{2.7}$$

or, equivalent

$$I = \int \Psi'^{*}\, \hat{O}\, \Psi'' d\tau = 0 \qquad \text{if } \Gamma(\Psi'^{*}) \otimes \Gamma(\Psi'') \not\supset \Gamma(\hat{O}) \tag{2.8}$$

Considering rovibrational transitions in the ground electronic state of H_3^+ where $\Gamma(\mu_A) = A''_1$ and $\Gamma^{(s)} = A'_1$, only ortho-transitions $A'_2 \Leftrightarrow A''_2$ and para-transitions $E' \Leftrightarrow E''$ are allowed. Further symmetry considerations lead to the set of selection rules given in Tab. 2.1 [19]. The parity of a certain level is given by $(-1)^k$ [40]. There are no rigorous selection rules for vibrational quantum numbers. The quantum

Table 2.1. – Selection rules for H_3^+

$+ \leftrightarrow -$
$\Delta J = 0, \pm 1; \quad J = 0 \nleftrightarrow J = 0$
$\Delta I = 0$
$\Delta K = 2n + 1$
$\Delta G = 3n$

number g [17] is connected with the nuclear spin in the following way [43]

$$ortho - H_3^+ \Longleftrightarrow g = 3n \tag{2.9}$$

$$para - H_3^+ \Longleftrightarrow g = 3n \pm 1, \tag{2.10}$$

where n is an integer.

Transition labels

The labeling used for the transitions presented in this thesis follows the convention reported by Lindsay and McCall [29]. As our experiment provides H_3^+ in the lowest rotational states of the vibrational ground state (see Chap. 5), all transitions are labeled by the upper state only,

$$v_1\nu_1 + v_2\nu_2^{|l_2|}. \tag{2.11}$$

The rotational states are specified by

$$^{[n|t|\pm 6|\pm 9|...]}\{P|Q|R\}\,(J,G)^{[u|l]}_{[u|l]} \tag{2.12}$$

where (J, G) describes the lower state (J=1 and G=0 or 1). The choice among $\{P|Q|R\}$ denotes $\Delta J = -1$,0, or $+1$ respectively. The left superscript describes ΔG. For brevity no superscript is used if the upper and the lower energy level have the same G. For $\Delta G = +3$, the superscript t is used while a superscript n indicates changes $\Delta G = -3$ or $\Delta G = 1$ if the lower level has G<3. Larger changes in G are indicated by the numerical value. When needed, the right superscript (subscript)

distinguishes the energetically upper (u) or lower (l) one of a pair of levels with the same G for the upper (lower) state.

2.3. H_3^+ in space

The H_3^+ ion is of great astronomical impact as illustrated in Fig. 2.7. Currently, about 160 molecules have been detected in the interstellar medium (ISM) or circumstellar shells [44]. This variety can be explained by fast two-body ion-molecule reactions that mostly proceed without any reaction barrier at the so called Langevin rate. As about 75% of the normal mass in the universe consists of hydrogen and the major component of the ISM is molecular hydrogen, the most stable ionic form H_3^+ is considered to be the key ion for understanding the interstellar chemistry [45]. H_3^+ is the perfect proton donor as almost all atoms and molecules have higher proton affinity than H_2. Exceptions with lower proton affinity are shown in Tab. 2.2.

Table 2.2. – Proton affinities for H_2 and all species with even lower proton affinity. The eight lowest proton affinity of H_2 renders H_3^+ the ultimate proton donor. [46]

	Proton affinity [eV]	Δ [eV]	Δ [cm^{-1}]
H_2	4.392	—	—
O_2	4.378	0.014	112.92
Ar	3.840	0.552	4452.18
N	3.559	0.833	6718.60
F	3.537	0.855	6896.04
F_2	3.453	0.939	7573.55
Ne	2.068	2.324	18744.33
He	1.849	2.543	20510.68

The formation of more complex molecules starts with the proton hop reaction

$$H_3^+ + X \rightarrow HX^+ + H_2 \tag{2.13}$$

followed by the efficient reaction pathway

$$HX^+ + Y \rightarrow XY^+ + H. \tag{2.14}$$

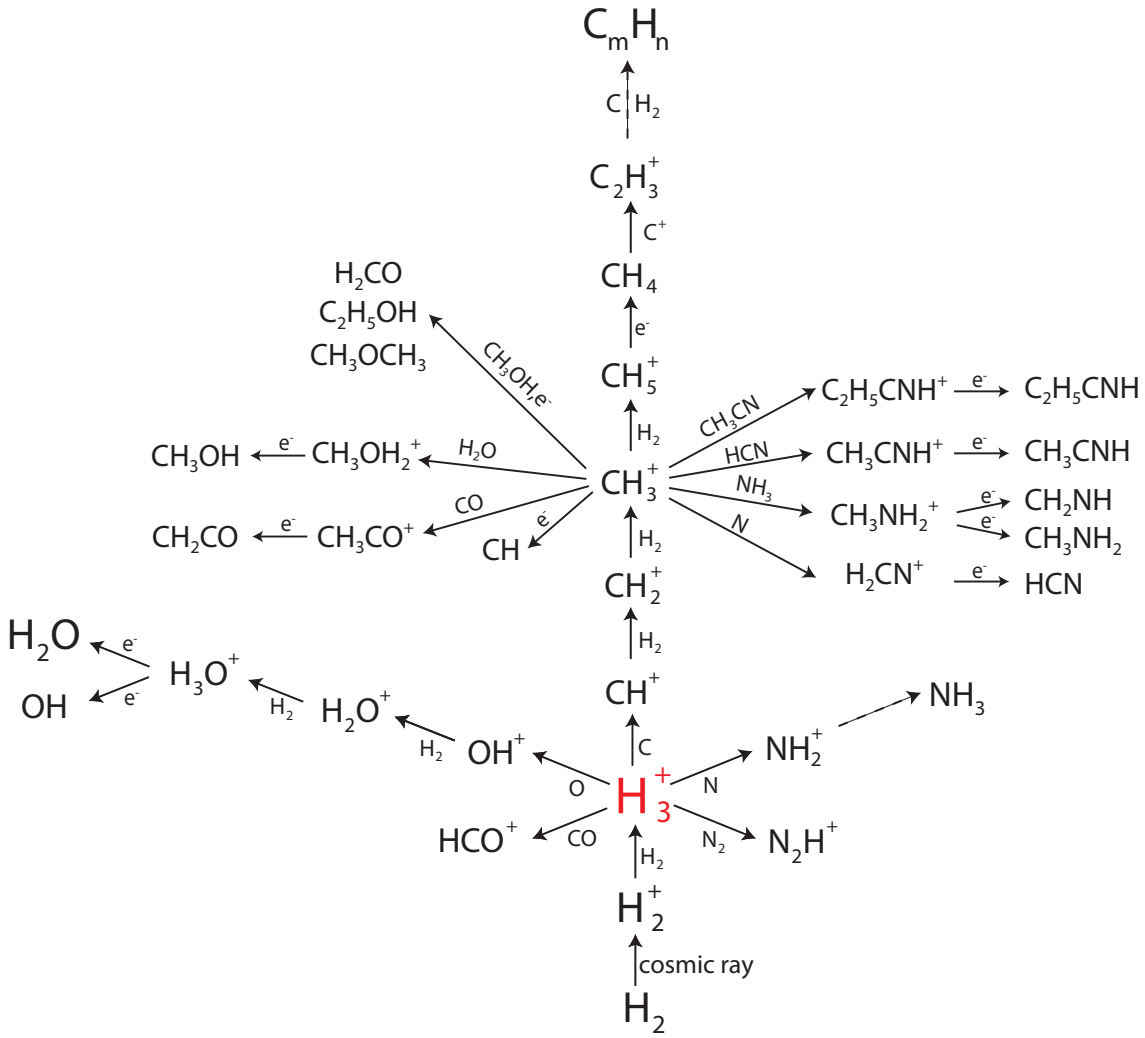

Figure 2.7. – Interstellar chemical network of ion-neutral chemistry. H_3^+ as universal proton donor is the initiator of interstellar chemistry leading to larger molecules such as water and hydrocarbons. Based on Ref. 43

A cut-out of the interstellar chemistry network is shown in Fig. 2.7. As fast production of molecules is essential for cooling gravitationally condensing gas, the reigning amount of H_3^+ plays a pivotal role in star formation. The production of H_3^+ follows Eq. (2.1) where the H_2^+ is predominantly formed by cosmic ray (cr) ionization

$$H_2 + (cr) \rightarrow H_2^+ + e^- + (cr). \tag{2.15}$$

Minor contributions come from the formation

$$H(n \geq 2) + H \rightarrow H_2^+ + e^- \tag{2.16}$$

in hot stellar winds or supernovae. In shocked molecular clouds the formation can occur by [47]

$$H^+ + H_2(n \geq 4) \rightarrow H_2^+ + H. \tag{2.17}$$

Besides chemical reactions removing H_3^+ from the interstellar medium (ISM), the dissociative recombination (DR) with electrons determines the steady-state concentration of H_3^+ and therefore the DR rate is a crucial parameter for the chemistry in the ISM [48]. In the last decades many experiments on determining this DR rate have been performed of which many at the MPI-K, resulting in a convergence of $10^{-7}\,\mathrm{cm^3 s^{-1}}$ [48, 49]. This allows astrophysicists to model the H_3^+ abundance in the interstellar medium. For further astrophysical interests such as the reigning H_3^+ ortho-para spin temperature [50] rotational state-specific rate coefficients are needed [51].

H_3^+ is also of great importance to the enhancement of deuterated species in space [52]. The cosmic D/H ratio is about 10^{-5}. So far, more than ten deuterated molecules have been detected in space, showing an enhancement compared to the cosmic D/H ratio by a factor of 100 to 1000. The process leading to this enhancement is known as deuterium fractionation where H_3^+ and H_2D^+ play a key role due to the slight difference in zero point energy. In general the exchange of a hydrogen atom by a deuteron leads to stronger bonding and thus energy is gained.

2.4. H_3^+ at dissociation

The rotational and vibrational behavior of H_3^+ and other polyatomic molecules with low excitation has been investigated extensively using high-resolution spectroscopy techniques. A general understanding of this behavior is provided by simple models of nuclei moving on simplified potentials close to the minimum equilibrium state. The understanding of nuclear motion near dissociation remains very limited for any polyatomic molecule. In comparison to diatomic systems where the situation is relatively straight forward, polyatomic systems are much more complicated. In polyatomic systems, energy can be stored in non-dissociating vibrational modes resulting in quasi-bound vibrational states lying above the dissociation limit. Furthermore, dissociation can lead to atomic as well as molecular fragments that also possess internal energy. The extraordinary complex and interesting photodissociation spectrum recorded by A. Carrington in 1982 was the first spark to enlighten the in depth investigation of rotation-vibration energy levels at dissociation for polyatomic chemically bound molecules. This investigation has been going on for over 30 years now, and similar spectra have been obtained for D_3^+, H_2D^+, and D_2H^+. Till this day only the behavior with respect to isotopic substitution can be explained by classical calculations, tempting Eyring to call it "the scandal of modern chemistry" [53].

2.4.1. The Carrington pre-dissociation spectrum

In the 80's, Carrington and co-workers published an extremely complex photodissociation spectrum [54, 55, 56, 40]. Approximately 27000 lines were detected within the $222\,cm^{-1}$ tuning range of the employed laser system. They produced hot H_3^+ by electron-impact ionization, selected these ions with a magnetic mass spectrometer to overlap them collinearly in an adjacent drift tube with an infra-red line tunable CW carbon dioxide laser operated with either $^{12}CO_2$ or $^{13}CO_2$ (see Fig 2.8). By tuning the ion velocity and therefore tuning the Doppler shift in combination with parallel and antiparallel alignment of the ion and laser beam, a frequency range from $872\,cm^{-1}$ to $1094\,cm^{-1}$ could be nearly completely covered. The spectra were detected through the increase in H^+ fragments induced by photodissociation and recorded by an electron multiplier after an electrostatic analyzer (ESA). Whereas many of the lines are associated with small energy releases of 10-$500\,cm^{-1}$, also

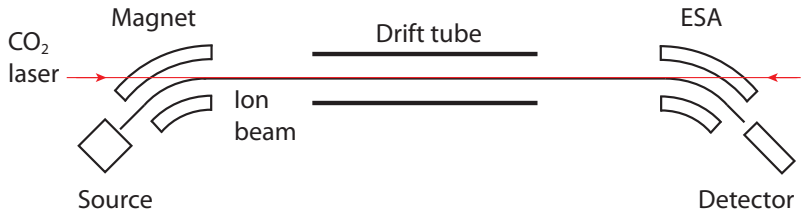

Figure 2.8. – Sketch of the Carrington experiment. Adapted from Ref. 55.

protons with more than 3500 cm^{-1} energy were observed, indicating that these latter transitions originate from transitions between states that lie both well above the dissociation limit. The lifetimes of the states that could be observed were restricted by the experimental procedure. Only ions with lifetimes above 1 μs could get from the source into the drift tube and the there excited ions fragmenting within 0.7 μs could be detected by the ESA. Detailed analysis of measured line profiles suggests lifetimes of the excited states of up to 20 ns, which is rather lengthy for molecular time scales[1] [59]. In addition, it was found that more intense transitions correlate with longer lifetimes of the upper state. The high-resolution spectra show no obvious structure and assignment is probably not possible at all, but when Carrington and collaborators convolved their high-resolution spectrum to create a low-resolution one, a coarse-grained structure arose showing four peaks at 876, 928, 978, and 1034 cm^{-1}. This coarse-grained regular feature has attracted many theoretical studies since then and the most commonly accepted concept involves a bright gateway state, a so-called horseshoe state, that is coupled to a bath of other nearby states [60, 61]. Presently, two recent publications brought up alternatives and additional states for explanation [62, 63].

2.4.2. Horseshoe states

A comprehensive overview on early attempts to explain the pre-dissociation spectrum can be found in a review of J. Tennyson [61]. The initial studies focused on revealing the nature of the Carrington-spectrum using classical or semi-classical techniques [64, 65, 66, 67]. One point of origin have been the lifetime restrictions, in particular the long lifetime of the upper state. Pollak and Schlier [68] as well as

[1] Application of Rice-Ramsprenger-Kassel-Marcus theory predicts that excited fragments with excess energy in the 2000-3000 cm^{-1} range dissociate within 3 ps [57, 58]

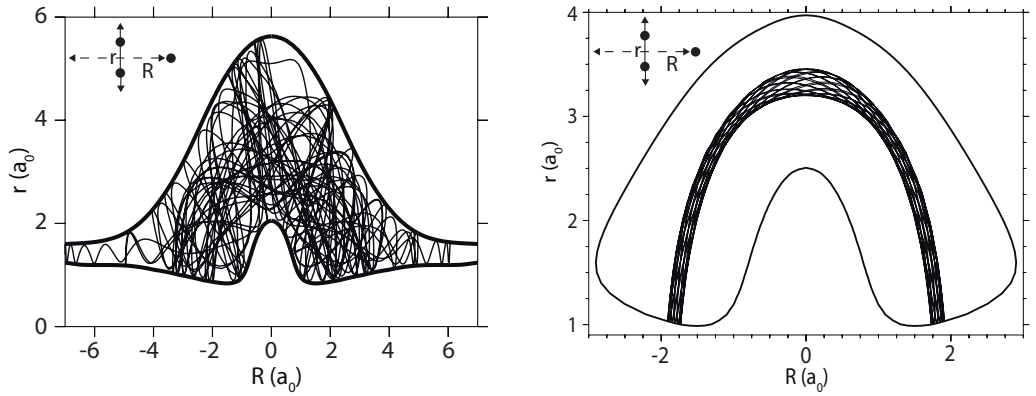

(a) Typical classical chaotic trajectory

(b) Classical trajectory of a stable periodic horseshoe state

Figure 2.9. – Classical trajectory of a bulk (a) and a horseshoe (b) state, taken from Ref. 72

Drohlshagen *et al.* [69] recognized that the strong vibrational coupling in the system redistributes vibrational excess energy too fast for Feshbach-type resonances to play a significant role. Therefore, the focus was put on quasi-bound states trapped behind a rotational barrier, so-called shape resonances [70, 71].

wave functions and energy-level distributions reflect the underlying structure of the phase space. At high energies, phase space is chaotic and therefore the high-lying vibrational states are expected to be irregular. Already above the barrier to linearity, classical trajectory studies on H_3^+ show the system to be highly chaotic [64] as can be seen in Fig. 2.9a. Berblinger *et al.* [64] were the first to find small regions in the phase space that displayed regular features in 2D calculations. The wave functions of these states do not sample all of the available phase space. Out of these localized modes, the so-called horseshoe states (see Fig. 2.9b) were the only ones to be stable also in 3D. Further investigations of Gomez Llorente and Pollak show that the horseshoe states are stable to rotational excitation with an effective rotational constant of $2B \approx 60\,\mathrm{cm}^{-1}$. This rotational spacing reconciles with the spacing of the peaks in the coarse grained spectrum [67]. Up to this day, this identification is the most specific one made to the Carrington spectrum. The horseshoe states were approved in early quantal studies on H_3^+ and it was stated that "the existence and strength of the horseshoe motion is beyond doubt" ([61] p.463). The build-up of amplitude for wave functions in the region of the horseshoe periodic orbit is

known as scarring. Le Sueur *et al.* [60] computed vibrational band intensities for H_3^+ from the vibrational ground and some other low lying states to all the other bound vibrational states. They reveal periodic structures in the transition strengths (similar to Fig. 5.3) where each peak in intensity corresponds to a horseshoe state. These results suggest that H_3^+ should have a strong observable rotation-vibration spectrum in the visible spectral region. Horseshoe states have been predicted for Ar_3 [73], Na_3, LiCN, and KCN [74]. In fact, no experimental data is available at all to either confirm or discard the existence of localized horseshoe states. Recently, a regular progression of vibrational states at the dissociation limit has been detected for $SCCL_2$. No theoretical calculations exist for this molecule [75, 76].

In the past few years, criticism has arisen commenting on the fact that all studies so far have used non-dissociative PES, which cannot be expected to give correct behavior for either bound or resonance states lying near the dissociation threshold. In 2005, Munro *et al.* [62] performed calculations on a PES with the correct properties at dissociation. They found horseshoe states at low to intermediate but not at high energies. Instead, they predict a new class of so called $H^+ - H_2$ asymptotic vibrational states near dissociation which are a type of shape resonances. More recently Silva *et al.* [63] suggest that also Feshbach-type resonances may play an important role for the spectrum.

3. Calculations on molecules

In 1929, Paul Adrien Maurice Dirac stated:

> "The general theory of quantum dynamics is now almost complete [...] The underlying physical laws necessary for the mathematical theory for large parts of physics and the whole of chemistry are thus completely known and the difficulty is only that the exact application of these laws leads to equations much too complicated to be soluble. It therefore becomes desirable that approximate practical methods of applying quantum mechanics should be developed" [77].

Early practical methods for describing small-amplitude vibrations about the equilibrium geometry neglect rotation-vibration interaction and provide a qualitative view by treating vibrational wave functions as products of harmonic oscillators and rotational wave functions by rigid rotor models [78, 79]. Most of the labeling schemes used today result from that time. This simple picture was quantitatively improved by using perturbation theory introducing couplings between rotation and vibration. For large-amplitude vibrations the perturbation theory approach is inadequate and modern, presently strongly evolving, *ab initio* methods have to be applied [80]. This chapter gives a general overview on the theoretical treatment of molecules and presents recent theoretical work on H_3^+.

3.1. Quantum-mechanical description of molecules

The key to the description of molecular systems is quantum mechanics, specifically the Schrödinger equation. The most general form of the Schrödinger equation is its

time-dependent formulation given by

$$-i\hbar\frac{\partial}{\partial t}\Psi = \hat{H}\Psi, \tag{3.1}$$

where $\hbar$ is Planck's constant h divided by 2π, Ψ is the wave function of the system containing all the information for all times t, and $\hat{H}$ is the Hamilton operator. For most spectroscopic studies involving the interaction between photons and molecules no time-dependent details on the molecular states and the transitions between them are necessary. It is sufficient to calculate the energy levels and the wave functions of the molecules to determine the possible transition frequencies. Therefore, the time-independent Schrödinger equation

$$\hat{H}\Psi = E\Psi, \tag{3.2}$$

where the Hamilton operator is given by

$$\hat{H} = \hat{T} + \hat{V} = -\frac{\hbar}{2m}\sum_{i=1}^{N}\nabla_i^2 - \frac{\hbar}{2}\sum_{k=1}^{K}\frac{1}{M_k}\nabla_k^2 + V(\vec{r},\vec{R}), \tag{3.3}$$

the sum of the kinetic energy of all (N) electrons and all (K) nuclei and the potential energy $V(\vec{r},\vec{R})$. Electron coordinates are given by small characters $\vec{r}_i$ and nuclei coordinates by capital letters $\vec{R}_k$. The potential energy is a sum of three terms

$$\begin{aligned} V(\vec{r},\vec{R}) &= V_{KK} + V_{Ke} + V_{ee} \\ &= \frac{e^2}{4\pi\epsilon_0}\left[\sum_{k>k'}\sum_{k=1}^{K}\frac{Z_k\cdot Z_{k'}}{R_{k,k'}} - \sum_{k=1}^{K}\sum_{i=1}^{N}\frac{Z_k}{r_{i,k}} + \sum_{i>i'}\sum_{i'=1}^{N}\frac{1}{r_{i,i'}}\right], \\ &\text{with } R_{k,k'} = \left|\vec{R}_k - \vec{R}_{k'}\right|, \quad r_{i,k} = \left|\vec{r}_i - \vec{R}_k\right|, \quad r_{i,i'} = \left|\vec{r}_i - \vec{r}_{i'}\right|, \end{aligned} \tag{3.4}$$

the first describing the Coulomb repulsion between the nuclei, the second describing the attraction of the electrons by the nuclei and the third describing the repulsion of the electrons among each other. Remembering the words of Dirac, even for the most simple molecular ion H_2^+, the Schrödinger equation (3.2) is not exact soluble. There are two approximate methods to treat real molecules. One approach solves the Schrödinger equation numerically. The obtained (generally poor) accuracy then depends on the program and computer power used. The thus obtained results

cannot easily be transferred to other problems. The second more elegant way is to apply physically founded approximations to simplify the molecular model and add refinements later on.

Considering the large mass difference, an electron roughly being 2000 times lighter than the proton, it is appropriate to consider the protons moving much slower than the electrons, so that the electron cloud can be regarded as instantaneously adapting to a particular nuclei configuration. Treating this approximation by perturbation theory leads to the following ansatz,

$$\hat{H} = \hat{H}_0 + \hat{H}', \qquad \hat{H}_0 = \hat{T}_e + V, \quad \hat{H}' = \hat{T}_K. \tag{3.5}$$

The unperturbed Schrödinger equation

$$\hat{H}_0 \cdot \Phi^{el}(\vec{r}, \vec{R}) = E^{(0)}(\vec{r}, \vec{R}) \tag{3.6}$$

describes a rigid molecule where the nuclear configuration $\vec{R}$ is kept fixed. $|\Phi_n^{el}(\vec{r}, \vec{R})|^2$ describes the electron cloud in a particular electronic state $|n\rangle$ with energy $E_n^{(0)}(\vec{R})$ for any arbitrary rigid nuclear configuration. The wave functions $\Phi_n^{el}(\vec{r}, \vec{R})$ of Eq. (3.6) can be chosen to form a complete orthonormal system, so that the wave functions of the complete Schrödinger equation (3.2) can be written as

$$\Psi(\vec{r}, \vec{R}) = \sum_m \chi_m(\vec{R}) \cdot \Phi_m^{el}(\vec{r}, \vec{R}) \tag{3.7}$$

Following this ansatz the following set of equations can be derived (see Sec. 2.1.2 in Ref. 81)

$$H_0\Phi(\vec{r}, \vec{R}) = E^0(\vec{R})\Phi(\vec{r}, \vec{R}), \tag{3.8a}$$

$$(H' + E_n^0(\vec{R}))\chi_n(\vec{R}) + \sum_m c_{nm}\chi_m(\vec{R}) = E\chi_n(\vec{R}), \tag{3.8b}$$

with

$$c_{nm} = \int \Phi_n^* H' \Phi_m d\vec{r} - \frac{\hbar^2}{2}\left[\int \Phi_n^* \sum_m \frac{1}{M_k}\frac{\partial}{\partial R_k}\Phi_m d\vec{r}\right]\frac{\partial}{\partial R_k}. \tag{3.9}$$

The two equations (3.8a) and (3.8b) form a coupled system of equations for the electronic Φ and the nuclear χ_n wave functions, being equivalent to the Schrödinger

Equation (3.2). The coupling results from the c_{nm} coefficients that are according to Eq. (3.9), dependent on the electronic wave functions Φ and describe how different electronic states Φ_n and Φ_m are coupled by the movement of the nuclei.

3.1.1. Born-Oppenheimer approximation

In the framework of the Born-Oppenheimer (BO) approximation the coupling between the nuclei and the electrons is completely neglected by setting all c_{nm} to zero, leading to the picture of nuclei moving in an effective potential generated by the electronic structure. This potential is the interpolation of energy values, obtained by solving the electronic problem at various fixed nuclear configurations, through a real continuous function of the nuclear coordinates, referred to as potential energy surface (PES). Within the BO approximation the Schrödinger equation leads to two uncoupled equations

$$\hat{H}_0 \Phi_n^{el}(\vec{r}) = E_n^{(0)} \Phi_n^{el}(\vec{r}), \tag{3.10a}$$

$$(\hat{T}_K + E_n^{(0)}) \chi_n(\vec{R}) = E_{n,i} \chi_{n,i}(\vec{R}) \tag{3.10b}$$

where E_n^{el} can be regarded as the potential U_n in which the nuclei move. The equations (3.10) form the basis for quantum chemistry.

3.1.2. Adiabatic correction

The BO approximation can be refined by taking the coupling expressed by the matrix elements c_{nm} into account. These matrix elements can be split in diagonal c_{nn} and non-diagonal c_{nm} $(n \neq m)$ parts. The diagonal terms c_{nn}

$$c_{nn} = \int \Phi_n^* H' \Phi_n d\vec{r} - \frac{\hbar^2}{2} \left[\int \Phi_n^* \sum_m \frac{1}{M_k} \frac{\partial}{\partial R_k} \Phi_n d\vec{r} \right] \frac{\partial}{\partial R_k} \tag{3.11}$$

can be simplified to

$$c_{nn} = \sum_K \frac{\hbar^2}{2M_K} \int \left(\frac{\partial \Phi_n^{el}}{\partial \vec{R}_K} \right)^2 d\vec{r}, \tag{3.12}$$

depending quadratically on the change of the electronic wave function Φ_n^{el} by variation of the nuclei coordinates. This adiabatic correction is essentially the expectation value of the kinetic energy of the nuclei, evaluated with the electronic wave functions Φ_n that parametrically depend on the nuclear coordinates. Using the diagonal matrix elements in (3.8b) and neglecting the non-diagonal elements, instead of the BO approximation Eq. (3.10b), the adiabatic approximation

$$(H' + U'_n(\vec{R}))\chi_n = E\chi_n \tag{3.13}$$

is obtained. In comparison to the BO approximation the potential in the adiabatic approximation

$$U'_n(\vec{R}) = E_n^{(0)}(\vec{R}) + \sum_K \frac{\hbar^2}{2M_K} \int \left(\frac{\partial \Phi_n^{el}}{\partial \vec{R}_K} \right)^2 d\vec{r} \tag{3.14}$$

contains a mass dependent correction term. This results in slightly different final PES for different isotopes. In the framework of the adiabatic approximation the movement of the nuclei does not lead to a mixing of electronic wave functions.

3.1.3. Non-adiabatic effects

In case that the non-diagonal elements c_{nm} are not negligible, the adiabatic approximation breaks down. This means that nuclear motion mixes several electronic states. These non-adiabatic effects cannot simply be taken care of by another additional correction to the PES. Instead, estimations for non-negligible non-diagonal elements can be determined using perturbation theory. Equation (3.5) can be written as

$$\hat{H} = \hat{H}_0 + \hat{T}_K = \hat{H}_0 + \lambda \cdot W, \tag{3.15}$$

$\hat{H}_0$ being the operator of the unperturbed rigid molecule and the perturbation operator describing the kinetic energy of the nuclei. The parameter $\lambda < 1$ gives the magnitude of perturbation depending on the ratio (m_e/M) of electron mass m_e to nuclear mass M. Appropriate perturbation theory leads to

$$E_n = \underbrace{E_0^{(0)}}_{BO} + \underbrace{W_{nn}}_{AC} + \underbrace{\sum_{k \neq n} \frac{W_{nk} \cdot W_{kn}}{E_n^{(0)} - E_k^{(0)}}}_{non-AC} + O(\lambda^3) + \cdots, \tag{3.16}$$

with

$$W_{nk} = \int \Phi_n^{el(0)*} \hat{T}_N \Phi_k^{el(0)} d\vec{r}. \tag{3.17}$$

providing the coupling between different electronic states. In the perturbation calculation with $\hat{T}_K$ as perturbation operator, the unperturbed term equals the BO approximation, the 1^{st} order perturbation term $W_{nn} = c_{nn}$ equals the adiabatic correction (AC), and the non-adiabatic effects (non-AC) are described by the 3^{rd} order perturbation term. From the 3^{rd} term it can be seen that the adiabatic approximation breaks down when $E_n^{(0)} - E_k^{(0)}$ becomes small. For H_3^+, the presence of the two dissociation channels H_2 ($^1\Sigma_g^+$)+H^+ and H_2^+ ($^2\Sigma_u^+$)+H leads to an avoided crossing between the lowest electronic states of the $^1A_1$ symmetry [40], making the non-adiabatic effects relevant for energetically high lying states.

The available computer power is insufficient to directly take non-adiabatic effects into account for high accuracy calculations. Even with large advances in computational power (assuming Moore's law [82] to be valid for the next decades), these calculations will still be too complex to be solved. Therefore, theoretical studies have focused on modeling the non-adiabatic effects as described below.

3.2. H_3^+ as benchmark for theory

Ab initio (first principle) calculations are advancing from qualitative and semi-quantitative understanding of molecular spectra towards achieving predictive power with considerable accuracy and confidence. Theoretical spectra are routinely calculated to develop computational methods that can determine accurate PES further and to help assigning experimental spectra. The ability to compute large datasets, far greater than is feasible with experiments, enable the calculations to move from microscopic spectroscopy to the macroscopic level of modeling the interstellar medium, stellar evolution, the earth's atmosphere and various other chemical processes. Therefore, reliable theoretical calculations are essential and must be tested against experiment when possible.

When a PES has been obtained, the choice of the coordinate system and axes, in which the nuclear motion Schrödinger equation will be solved, must be made according to the two criteria: 1) do the wave functions meet the boundary conditions

and 2) are the calculations computational efficient. These considerations become particularly important for the energy regime above the barrier to linearity where H_3^+ can sample linear configurations leading to a singularity in kinetic energy operator $\hat{T}_k$. Several coordinate systems have been employed to study the H_3^+ ion. Two coordinate systems suitable for calculations above the barrier to linearity are Jacobi coordinates and hyperspherical coordinates. Jacobi coordinates treat the system as an atom interacting with a diatomic molecule and together with spherical oscillator functions are able to treat the singularities at linear geometries correctly [35]. Jacobi coordinates, however, suffer from poor convergence for high J as these coordinates cannot cover the full D_{3h} symmetry of H_3^+ [29, 83]. In contrast, hyperspherical coordinates together with hyperspherical harmonics perform especially well for linear geometries. The singularities appearing in the Hamiltonian are treated exactly as boundary conditions of the hyperspherical harmonics [84, 85, 86, 87].

Experimental high-resolution spectroscopic data possesses a lot of information on details of the PES. Unfortunately, it is only possible in the case of simple diatomic systems to directly derive the PES from observed energy levels. For polyatomic molecules, the PES must be constructed in an iterative way, as illustrated in Fig. 3.1. The first step is to solve the Schrödinger equation for the electrons (see Eq. 3.8a). This allows for creating a dipole moment surface and the BO part of the PES. Solving for the motion of the nuclei provides rovibrational energies and rovibrational wave functions. The rovibrational energies and the information from the dipole moment surface together lead to predictions on transition intensities. From the rovibrational energies, together with appropriate selection rules, transition frequencies are calculated. Experimental data can be used to test the accuracy of the predicted transition intensity and thereby test the goodness of the rovibrational wave functions and allow for refinement of the PES. In an analog way, experimental data can be used to test the calculated transition frequencies and so to probe the quality of the rovibrational energy levels. A simple approach to increase the predictive power of the calculations is to apply an empirical correction based on the deviations between theory and experiment directly on the calculated rovibrational energies. It is clear that the relatively simple approach is limited in obtaining further understanding. In 2001, C. M. Lindsay and B. J. McCall [29] performed an extensive comparison of experimental data with various theoretical calculations including adiabatic corrections up to $9000\,\mathrm{cm}^{-1}$. The deviations increasing with higher energies

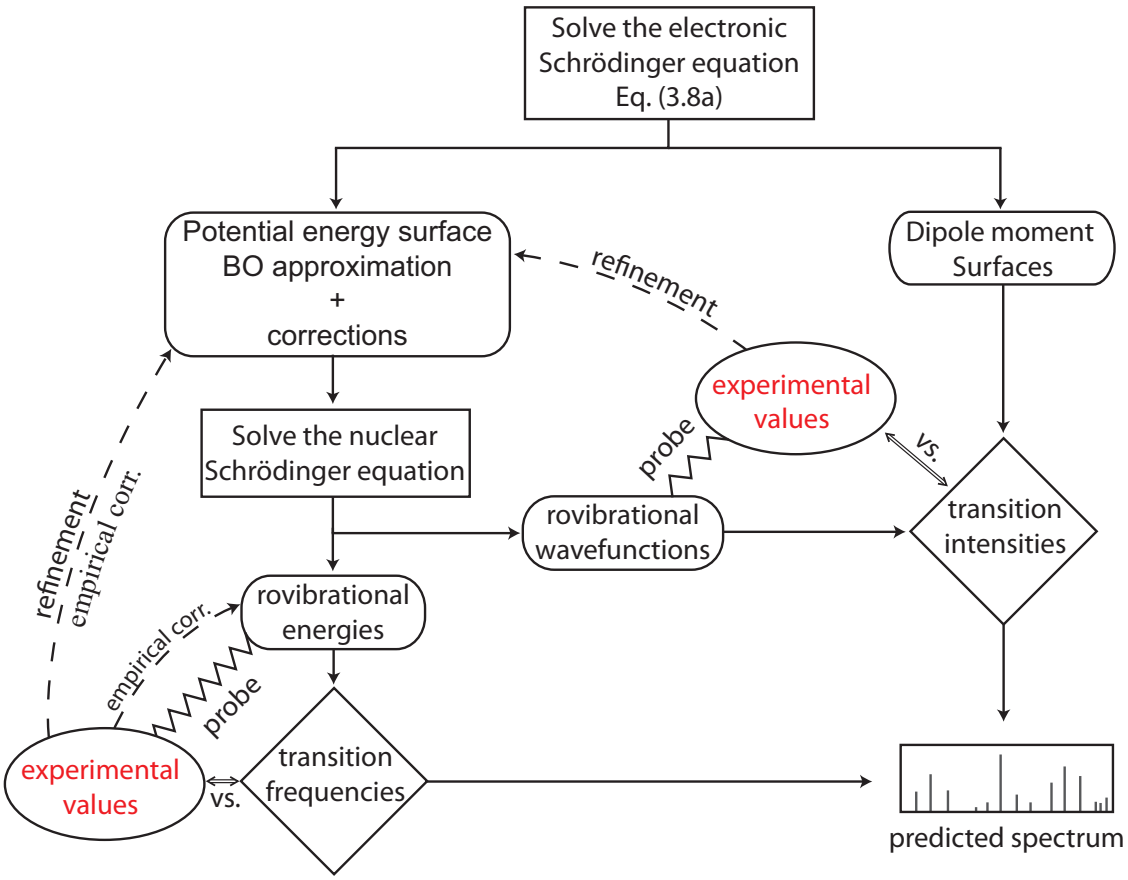

Figure 3.1. – Flow diagram for *ab initio* calculations to predict spectra of polyatomic molecules. Experimental data on both transition frequencies and intensities can be used to test the accuracy of the predictions, that means to probe the rovibrational energies and wave functions. Empirical corrections can be implemented to increase the accuracy of the predictions. The experimental data may also be used to test the refinements on the BO approximation, leading to improved treatments of (non) adiabatic corrections

are definitely a clear evidence that non-adiabatic have to be taken into account to reach spectroscopic accuracy.

3.3. Line lists

Nearly all advances made in H_3^+ spectroscopy have so far relied on *ab initio* calculations that in return have been improved by experimental data. Our search for transitions in the NIR to VIS spectrum of cold H_3^+ relied on the predictions of A. Alijah and co. and J. Tennyson and co.[88]. These predictions have been essential in selecting observable transitions, narrowing down our search, and afterwards assigning the measured transition. Below the various line lists that we have used are described.

3.3.1. Line lists of J. Tennyson and collaborators

J. Tennyson and collaborators provide two valuable sources of information that can aid our spectroscopic studies on H_3^+. The first line list dates back to 1996 [88] and is labeled TEN96. All calculations by J. Tennyson and collaborators are performed in Jacobi coordinates. Only transitions from the J=1 (G=0,1) ground states have been regarded in this thesis. A follow up publication [89] assigned all spectroscopic quantum numbers up to 9000 cm^{-1} and $J \leq 9$. The traditional spectroscopic quantum numbers v_1,$v_2^{l_2}$ for the higher energy region are not given. The data sets do, however, contain expected transition intensities. This has been of particular importance for selecting transitions, that we estimated to be observable within our sensitivity limit. The second line list denoted as TEN09 [90] providing also J,G quantum numbers and transition intensities, is based on a pure *ab initio* calculated PES [91].

Ten96

The TEN96 from L. Neale, S. Miller and J. Tennyson was the first comprehensive line list, containing more than 3×10^6 lines for $J \leq 20$, intended for modeling purposes [88]. The calculation is based on the PES of B. Dinelli *et al.* [92] which in principle is an empirically adjusted PES of Frye *et al.* and thereby includes to some

extent non-adiabatic effects. Eleven parameters have been optimized to reproduce the experimental data of 243 H_3^+ energy levels up to $3\nu_2$ and $J = 9$. The calculated wave functions and the highly accurate dipole moment surface of Röhse *et al.* [33] are used to determine transition intensities. The values provided in this line list are J', E', J'', E'', ω, A_{if}, g where J', E', J'', E'' are the rotational quantum number and energy level of the upper and lower state, respectively. The energies are given relative to the lowest allowed state $J = 1$, $G = 1$. The symbol ω denotes the transition frequency $E' - E''$. A_{if} is the Einstein A coefficient in s^{-1} and g is the nuclear spin degeneracy factor. For technical reasons according to Ref. 88 the ortho/para labeling resulting in $g = 4$ and 2 has to be performed manually. The authors expect the energy levels to be converged to about $0.05\,cm^{-1}$ for energies below $5000\,cm^{-1}$ increasing to $\sim 1\,cm^{-1}$ around $15000\,cm^{-1}$.

Ten09

The TEN09 line list is a higher energy extension to the published calculations of O. L. Polyanski and J. Tennyson in 1999. They use the highly accurate PES of Cencek *et al.* [91] which includes adiabatic corrections, shifting the energies by $\sim 100\,cm^{-1}$, and relativistic corrections, shifting the energies by $\sim 2\,cm^{-1}$. Non-adiabatic effects are modeled in a similar way as previously performed for diatomics, by using different but constant mass for the rotational and the vibrational term. The predicted transition intensities are similar for both line lists. The deviations in frequencies between experiment and theory are smaller than in TEN96 for the energy regime below $9000\,cm^{-1}$ treated in the original paper. However, the energy levels that are poorly reproduced within Ten96 are even worse reproduced in this new line list, specifically above $10000\,cm^{-1}$. This indicates that the non-adiabatic effects are still not accounted for in an adequate manner. For a better treatment either the constant masses must be adjusted further or as stated already by Moss and Bunker [39], the scaling of the mass should be a function of $\vec{R}$.

3.3.2. Line lists of A. Alijah and collaborators

In contrast to the calculations of J. Tennyson and collaborators, A. Alijah and collaborators employ hyperspherical coordinates that are in principle better adapted

to the H_3^+ molecule. The obtained "hyperspherical states" are characterized by exact quantum numbers I, J, $\Gamma_{(rv)}$. Assignments to the traditional spectroscopic quantum numbers ν_1, $\nu_2^{l_2}$, J, G are made semi automatically using the algorithm developed in Ref. 93. This algorithm is based on the symmetry properties of H_3^+ and relies on recognizing energetic progression patterns. A drawback, so far not solved, is the fact that in the hyperspherical approach the Hamiltonian does not split into the traditional rotational and vibrational parts, preventing the use of a mass-scaling approach such as the one performed by J. Tennyson to account for non-adiabatic effects. Instead, these effects are handled by a simple empirical correction formula adjusting the calculated energy values. A. Alijahs line lists are expected to provide more accurate transition frequencies. No transition intensities are included. We have employed two different data sets during our search for NIR to VIS transitions.

Ali03 & Alic03$_c$

The Ali03 predictions use the same PES as Ten09 namely that of Cencek *et al.*. Analysis of the deviations between theoretical calculation on this surface and the experimental data listed in Ref. 29 reveal large deviations for the different vibrational bands and a rather small shift for rotations. These discrepancies are assumed to be due to non-adiabatic effects and following the approach from Wolniewicz for H_2, the adjusted rovibrational energy levels can be described by

$$E_c^{(vr)} = E_t - b_1 E_t^{(0)} - \overline{a_1} J(J+1) - \overline{a_2} G^2, \tag{3.18}$$

where E_t is the calculated value without non-adibatic corrections, $E_t^{(0)}$ is the calculated band origin and the numerical values of the coefficients are $b_1 = 1.0123 \times 10^{-4}$, $\overline{a_1} = 2.0436 \times 10^{-3}\,\mathrm{cm}^{-1}$, and $\overline{a_2} = -1.3600 \times 10^{-3}\,\mathrm{cm}^{-1}$ [36]. As the non-adiabatic shifts caused by rotation are about the same in any vibrational band, these effects cancel out in the calculation of the transition frequency and therefore the even simpler correction formula

$$E_c^{v} = E_t - b_1 E_t^{(0)} \tag{3.19}$$

can be applied. In a private communication, A. Alijah provided us with an extension up to $20\,000\,\mathrm{cm}^{-1}$ on the calculation from the original paper [36].

Ali10a

The Ali10a line list was produced using the same formalism as for Ali03 but instead of the Cencek PES the "accurate *ab initio* based multisheeted double many-body expansion potential energy surface for the three lowest electronic states of H_3^+" by L. P. Viegas, A. Alijah, *et al.* [94] has been used. This is an accurate global PES that should be adequate for studying non-adiabatic effects.

Part II.

Experimental Setup & Measurement Technique

4. The 22-pole trap setup

This chapter describes the 22-pole trap setup and the utilized laser systems. The first near-infrared (NIR) measurements were performed in the experimental setup as specified here. For later measurements on visible (VIS) transitions, modifications were implemented to increase the sensitivity of our spectroscopy method. These modifications are described later in Chap. 6, preceded by an explanation of the measurement procedures in Chap. 5, which treats the limiting factors of the sensitivity. Below, the individual elements of the trap setup are presented, followed by a description of the laser systems and their implementation into the spectroscopy procedure.

4.1. Overview

A variety of 22-pole traps are being operated worldwide. The range of applications vary from collisions with small molecules to photodissociation of large biomolecules. This includes the investigation of ion-neutral collisions particularly at low, astrophysically relevant, temperatures to measure rate coefficients, reaction barriers, branching ratios, and to study cluster formation [95, 96]. Studies on photodetachment of anions as well as associative detachment in 22-pole traps have been presented [97] and, recently, spectroscopy and the investigation of dissociation dynamics of cold biomolecular ions have been reported [98, 99]. The 22-pole trap setup that is used for the experiment presented here, was initially build at the Max-Planck Institut für Kernphysik to investigate the temperature dependent dissociative recombination of H_3^+ with electrons in the storage ring TSR [100]. Besides its application as a temperature-variable ion source for the storage ring, it can be operated as a stand-alone device, as presented in this thesis, to perform spectroscopic experiments [100, 101, 102]. The setup is shown in Fig. (4.1) and consists of

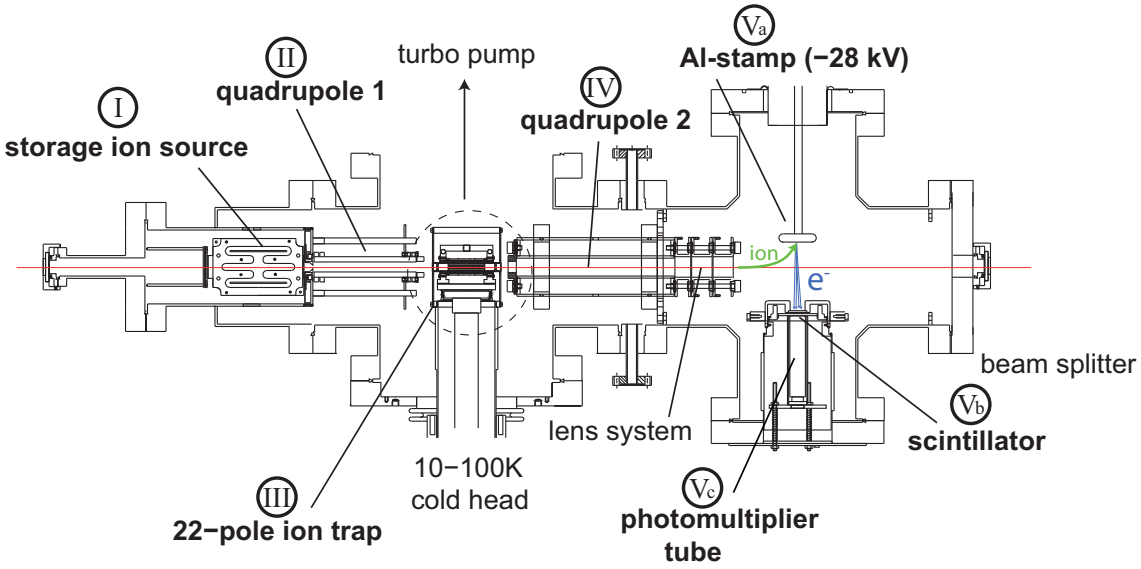

Figure 4.1. – Original scheme of the 22-pole trap setup: The H_3^+ ions are produced in the storage ion source (I), guided with the 1^{st} quadrupole (II) into the 22-pole trap (III), and are there laser excited. Mass selected (IV) ions are counted with the Daly-type detection system (V) consisting of an Al-converter (Va), an Al-covered plastic scintillator (Vb), and a single photon counting PMT (Vc).

five main parts, namely

I. the radio-frequency storage ion source [103, 104],

II. the 1^{st} linear quadrupole, operated as an ion guide,

III. the 22-pole trap mounted on a cold head,

IV. the 2^{nd} linear quadrupole, operated as a mass filter,

V. and the Daly-type detection system.

I. Radio-frequency storage ion source

The H_3^+ ions are produced in a rf storage ion source (15.9 MHz, 37 V_{pp})(see Fig. 4.1) whose geometry is optimized to lengthen the residence time of the ions inside the source as long as possible [105]. This allows for radiative and collisional relaxation processes down to the source temperature of around $\sim$ 400-500 K, leading to a

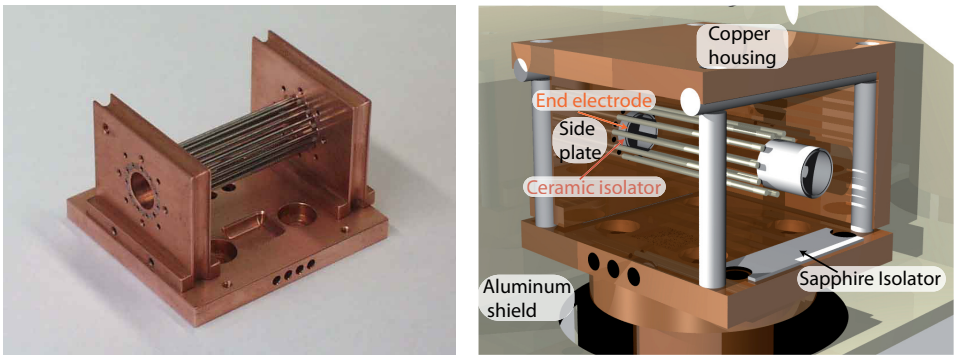

(a) (b)

Figure 4.2. – The design of the 22-pole trap at the Max-Planck-Institut für Kernphysik.

smaller energy spread compared to traditional discharge sources. In addition, lower extraction voltages ($-0.5\,\mathrm{V}$) can be used to guarantee a good ion capture of the 22-pole trap. The formation of H_3^+ is a two-step process. First, H_2^+ is formed via electron-impact ionization from a tunable rhenium filament and then the subsequent reaction

$$H_2 + H_2^+ \rightarrow H_3^+ + H + 1.6\,\mathrm{eV} \tag{4.1}$$

forms H_3^+. These H_3^+ ions are to a greater or lesser extent excited depending on the H_2 pressure inside the ion source and the dwell time. The experiments are performed in a pulsed mode and therefore confinement and ejection of H_3^+ ions is controlled by applying a positive or negative voltage on the source exit electrode.

II. First quadrupole

A short (90 mm) linear quadrupole (9.4 MHz, $38\,\mathrm{V}_{pp}$) is fixed directly after the ion source. This small quadrupole with an inner radius of 4.3 mm and a length of 90 mm, guides the ions from the source to the ion trap. The quadrupole is operated in rf-only mode. This indirect connection between the source and the trap is preferential, because it reduces the leaking of neutral H_2 from the source into the trap by roughly a factor of four.

III. Cryogenic 22-pole trap

The heart of the setup is a cryogenic 22-pole rf trap (see Figs. 4.1 and Fig. 4.2) embedded in a massive copper housing mounted on the second stage of a cold head (Leybold Coolpower 2/10). The cold head can reach temperatures down to 10 K and has a cooling power of 2 W at 10 K. An aluminum shield is attached to the first stage of the cold head at 40 K and encloses the copper housing. This shield protects the trap from undesired heating by the surrounding 300 K blackbody radiation. Two gas-lines guided along the Al shield end in the bottom copper plate providing a constant flux of cold Ar and He gas. In order to perform experiments at temperatures higher than 10 K, where most gases freeze out, two capton heating foils are mounted below the copper ground plate allowing for temperature variations between 10 - 100 K. Two Si diodes (type Lakeshore DT-470-CU-11A) are attached on opposite sides of the copper housing and monitor the temperature. The details of 22-pole traps are extensively described in literature [95, 106] and hence only a brief summary is given here. The trap consists of 22 surgeon steel rods alternatingly planted into the copper side plates. An appropriate rf voltage (19 MHz, 44 V_{pp}) applied to the two side plates result into an effective cylindrical potential similar to that of a classical Paul trap. The essential difference is a much steeper, nearly box-like radial potential with a wide effective-field free region increased by the multipole, minimizing the effect of rf heating. For axial confinement, a positive voltage is applied to two cylindrical dc electrodes encased by ceramic isolators (see Fig. 4.2b). The H_3^+ ions are cooled with He buffer gas, which couples the internal degrees of freedom of the injected ions to the cold environment. In the present experiments, the trap was operated at 60 K to prevent the Ar gas from freezing to the trap walls and housing.

IV. Second quadrupole

The second rf quadrupole is operated in mass-selective mode. A commercial EXTREL 150 QC power supply is used to drive the quadrupole and provides a fixed frequency of 1.2 MHz and a resolution of 2000 for a mass-to-charge ratio of 500. By changing simultaneously the amplitude of the ac and dc voltage, keeping the ratio V_{ac}/V_{dc} constant, the desired ion masses can be selected and guided to the detection system.

V. Daly-type detection system

The Daly detection system consists of an Al stamp, a scintillator, and a photomultiplier tube (PMT)(see Fig. 4.1V). The stamp is at a potential of $-28\,\mathrm{kV}$ to attract the cations (Va). About 3-4 secondary electrons are emitted per impinging ion and accelerated in the same high-voltage field onto a grounded aluminum coated plastic scintillator (Vb) on the opposite site. There the electrons are converted into photons that are detected by a PMT (Hamamatsu R4124) placed outside the vacuum chamber (Vc). The PMT is the most sensitive to 420 nm ($23810\,\mathrm{cm}^{-1}$) light ($\sim$ 11.5 % quantum efficiency), the quantum efficiency decreasing towards shorter and longer wavelengths. For VIS light at 600 nm ($16667\,\mathrm{cm}^{-1}$) the quantum efficiency is still 3 %. Therefore an optical filter, blocking $520-680\,\mathrm{nm}$ ($14706-19231\,\mathrm{cm}^{-1}$) is placed in front of the PMT. In the near infrared NIR region (close to the visible) the quantum efficiency dropped below 0.05 %. For all presented measurements, no optical filter is applied in the NIR. The design of the detection system is robust against degradation from successive ventings and provides near-unity detection efficiency without any mass dependency. As none of the components of the Daly detector lie on the central axis of the setup, laser beams can pass the 22-pole trap setup.

4.2. Laser systems

Three different laser systems have been used to cover the large frequency range of the spectroscopy measurements (see Tab. 4.1). An in-house constructed tunable NIR diode laser system covers the range for the $3v_2$ overtone band of H_3^+. The NIR to VIS Ti:sapphire laser systems, with either long- (LW), mid- (MW), or short-wave (SW) mirror sets, enables detection of vibrational states involving four to six vibrational quanta $v_1 + v_2 = 4, 5, 6$. The Dye laser system and respective dyes offers probing of energy levels with up to nine vibrational quanta. The Ti:sapphire and Dye lasers were pumped with either a Spectra Physics Millenia 10 W or a Coherent Verdi v10 10 W laser, which are both frequency doubled Nd:YVO_4 lasers at 532 nm. The wavelength of the laser light entering the trap setup is recorded by either an EXFO WA-1500 wavemeter (Michelson type interferometer) or a HighFinesse WS7 wavemeter (Fizeau type). Both wavemeters are calibrated by Doppler-free Li spec-

Table 4.1. – The laser systems used in the here presented spectroscopy measurements. The Ti:sapphire (TiSa) laser is operated with three different mirror sets denoted as long wave (LW), mid wave (MW), and short wave (SW). The dye laser is operated with two different dyes, DCM and Rhodamine B.

laser system	spectral range (cm^{-1})	scan range (cm^{-1})	typical output power (mW)
IR-diode[1]	$7\,100 - 7\,245$	0.3	$10 - 13$
Ti:sapphire[2] (LW)	$10\,101 - 11\,494$	1.0/3.0	$200 - 300$
Ti:sapphire[2] (MW)	$11\,494 - 12\,821$	1.0/3.0	$800 - 1100$
Ti:sapphire[2] (SW)	$12\,821 - 14\,286$	1.0/3.0	$600 - 800$
Dye (DCM)[3]	$15\,015 - 16\,268$	1.0	$650 - 850$
Dye (Rhod. B)[4]	$16\,155 - 17\,123$	1.0	$450 - 650$

[1] Toptica LD-1400-0020-AR-1
[2] Coherent 899 ($1.0\,cm^{-1}$) or Coherent MBR ring laser ($3.0\,cm^{-1}$)
[3] CAS number 51325-91-8
[4] CAS number 81-88-9

troscopy (^{6}Li D_2 line, $2^2S_{1/2} \rightarrow 2^2P_{3/2}$, $14903.633\,cm^{-1}$ [107]) on a regular basis, resulting in an absolute uncertainty of $0.005\,cm^{-1}$ for all measured transitions.

4.2.1. Alignment

The laser alignment is of great importance, specifically for the determination of the transition intensity (see Chap. 8). A schematic representation of the lasers, laser path, optics, and the trap is given in Fig. 4.3. For a diode laser measurement, the mirror M1 (mounted on a flip mount) is moved out of the beam path and the $\lambda/4$ and $\lambda/2$ wave plate as well as the polarizing beam splitter (PBS) are removed from the setup and the beam is blocked at the exit window of the 22-pole trap setup. For measurements with the diode laser the laser beam passes the trap only once.

The Dye and accordingly the Ti:sapphire laser are located in an adjacent room, the total length of the laser path from the laser systems to M1 being about 7.5 m. A lens and a telescope shape a parallel beam of about 3 mm in diameter. For the Dye and the Ti:sapphire laser, multiple crossings of the 22-pole trap setup are arranged. The multiple passings increase the available laser output power by a factor of two (see Tab. 4.2). To pass the trap four times, a $\lambda/2$ wave plate and an adjacent PBS

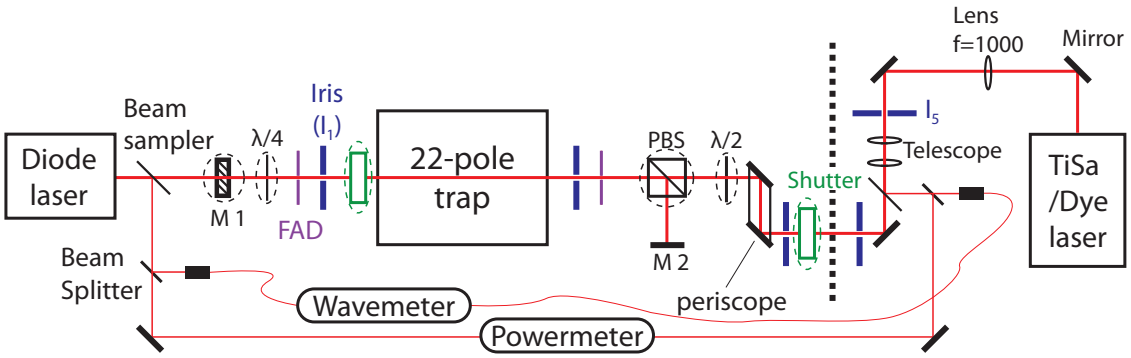

Figure 4.3. – Laser path alignment. The Dye and the Ti:sapphire laser are located in an adjacent room indicated by the black dashed line. The total distance of the laser path for any of these laser systems up to M1 is about 7.5 m

Table 4.2. – The estimated laser power available inside the 22-pole trap.

optical element	transmission
mirror	0.98
$\Lambda/2$	0.92
$\Lambda/4$	0.98
PBS	0.95
window	0.91

(a) Measured transmission for the given optical elements.

# of passings	relative power
1	0.72
2	0.56
3	0.38
4	0.30
sum	1.95

(b) Laser power per trap passing relative to the total laser output power.

let a defined polarization pass the trap the first time. After the trap, the laser-beam polarization is effectively rotated by 90° by a $\lambda/4$ wave plate, which is passed before and after the reflection on M1, respectively. The now back-traveling beam is directed from the PBS onto mirror M2, there reflected and then passes for a third time through the trap setup. The anew double passing of the $\lambda/4$ wave plate changes the polarization again by 90° and so the second back-traveling beam passes the PBS towards the periscope. In case of only passing the trap twice, the $\lambda/2$ and $\lambda/4$ wave plates as well as the PBS are removed and the laser beam is simply reflected at mirror M1. All backtraveling laser beams from multiple passing are dumped on iris I_5, horizontally right to the pinhole. The laser-beam path through the trap is fixed for all measurements by two fluorescing alignment discs (FAD) with a hole of 1.5 mm in diameter and two irises (1-20 mm), one of each placed on either side of

the 22-pole trap setup. During a transition intensity measurement (see Chap. 5), both FADs are flipped out and the irises are set to 2.5 mm in diameter to increase the overlap between the laser and the ions. The irises are not fully opened to ensure for all laser systems that always the exact same volume of the trap is passed by the laser-beam. For a line search and frequency determination, the irises are opened completely to maximize the available laser power.

Laser monitoring

The measurement procedure (see Chap. 5) requires the laser to be blocked from entering the trap most of the time (about 80% of the duty cycle there is no laser interaction). Therefore a mechanical shutter is positioned between the applied laser system and the 22-pole trap. The typical laser interaction time τ_{LIT} is $\sim$100 ms. This is too short to perform a laser-power measurement after passing the trap. Instead, a beam sampler diverts about 1-5% of the beam right after each laser system. This beam sample is further divided by a beam splitter, one part is fed into the wavemeter via a fiber, the other part is focussed onto the power meter. This means that only a fraction of the laser power is recorded. Normalization of this fraction is performed. Before and after each spectroscopy measurement, the laser power is calibrated at a fixed laser wavelength and at several positions before and after the 22-pole trap setup. The laser power is monitored by a Coherent FieldMaster-GS power meter [1]. Figure 4.4 left frame shows a typical laser frequency recording of the Dye laser illustrating the stability of the frequency scan covering multiple trap fillings. Adjacent, in the right frame, the corresponding laser-power recording is given. A run is defined as scanning the laser with particular frequency steps over the pre-selected wavelength range in any direction. As can be seen the laser power is dependent on the laser frequency and, in case of the Dye laser, a decay of the output power with time is clearly visible. The output power of the diode laser and the Ti:sapphire laser depend also on the set frequency but stay nearly constant over time.

[1] Ophir thermic sensor 3A-FS ,Coherent optical sensor LM-2-IR

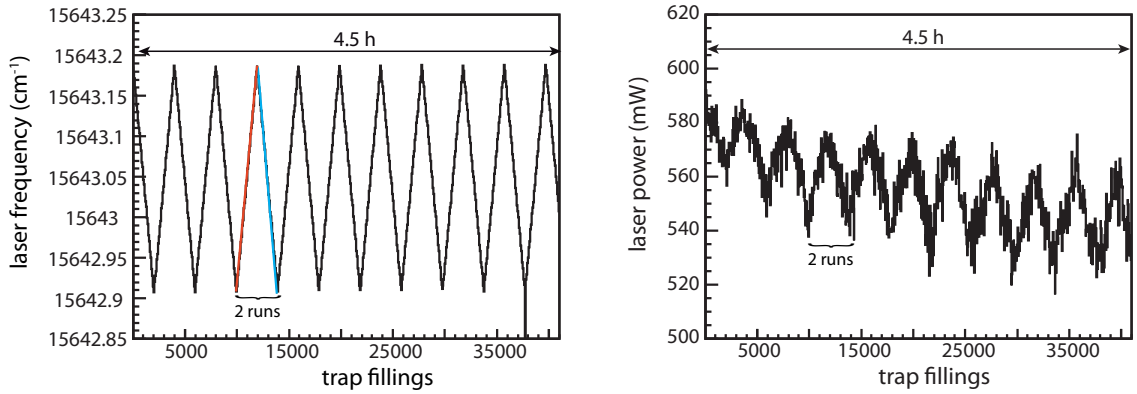

Figure 4.4. – Dye laser characteristics: On the left, the laser frequency vs. trap fillings is shown. One scan of the chosen frequency range, either up (red) or down (blue), is referred to as a run. On the right, the monitored laser power for the same measurement is depicted. The output power of the Dye laser is steadily decreasing with operation time. In the first few days of operation, it decreases about 10 mW per day. After 4-5 days, 20 mW can be lost within a few hours.

5. Chemical probing spectroscopy

As explained in Part I., the only accessible spectroscopic signature of H_3^+ is its comparatively weak vibrational spectrum. This chapter explains in detail the experimental procedure used to reveal the weakest rovibrational transitions of H_3^+ measured so far.

5.1. Chemical probing

Most previous spectroscopic studies on H_3^+ used conventional absorption spectroscopy in plasma discharge tubes. Appendix B gives an overview on the previous and current H_3^+ spectroscopy experiments. Even with long optical path lengths, high H_3^+ number densities, and elaborate lock-in techniques, the absorption spectroscopy, as stated in two recent papers of Oka and co-authors [30, 31], seems to have reached its sensitivity limit for transitions having an Einstein B_{lu} coefficient of $\sim 10^{18}\,\mathrm{cm^3 J^{-1} s^{-2}}$. This sensitivity limit restricts the investigation of energy levels to below $14\,000\,\mathrm{cm^{-1}}$. Plasma discharge tube experiments produce a broad distribution of rovibrational excited H_3^+ ions. This allows for measuring hot band transitions. However, the respective rovibrational populations are low and it is next to impossible to assign all energetically high-lying transitions from a hot discharge experiment, where a variety of lower states has to be considered. To facilitate the assignment in the higher energy regime, the study of overtone transitions with a restricted number of lower (higher populated) rotational starting states is crucial.

Here, laser-induced reactions (LIR) are used to pave the way to energy levels above the $14\,000\,\mathrm{cm^{-1}}$ above the ground state. LIR or chemical probing spectroscopy in an ion trap was first presented by S. Schlemmer *et al.* [108]. LIR represent a method of action spectroscopy where the laser interaction with trapped ions leads to changes in the chemical composition of the ion cloud. The technique relies on a well-defined cold

Table 5.1. – Typical pressures and densities of the different gases present inside the 22-pole trap setup.

	Source		Trap	
Gas	Pressure [mbar]	Density [cm^{-3}]	Pressure [mbar]	Density [cm^{-3}]
N_2	$< 5.0 \cdot 10^{-9}$	$\sim 1.2 \cdot 10^{8}$	$< 2.7 \cdot 10^{-9}$	$\sim 2.3 \cdot 10^{9}$
H_2	$3.4 \cdot 10^{-5}$	$\sim 8.1 \cdot 10^{11}$	$2.0 \cdot 10^{-8}$	$\sim 1.7 \cdot 10^{11}$
Ar	$9.6 \cdot 10^{-9}$	$\sim 2.3 \cdot 10^{8}$	$1.5 \cdot 10^{-5}$	$\sim 1.3 \cdot 10^{13}$
He	$3.0 \cdot 10^{-6}$	$\sim 7.1 \cdot 10^{10}$	$3.1 \cdot 10^{-3}$	$\sim 2.7 \cdot 10^{15}$

ion ensemble, which is unaffected by the probe gas. When ions are (laser) excited, they will react, leading to different-mass ions. After laser interaction, the extracted ions are mass selected and recorded by single ion counting detectors, giving rise to high sensitivity. As H_3^+ is a nearly universal proton donor (see Sec. 2.3), one of the exceptions from Tab. 2.2 has to be used as reactant partner to probe excited H_3^+ only. The measurements presented in this thesis were performed using the endothermic reaction

$$H_3^+ + Ar \leftrightarrow ArH^+ + H_2 - 0.55\,eV \tag{5.1}$$

to detect laser-excited H_3^+.

Figure 5.1 depicts a special representation of the H_3^+ PES, where two H-H bonds are forced to be equal, while varied in length to give the minimum energy for a given angle θ between them. As can be seen from this figure, H_3^+ ions in the vibrational ground state cannot react with Ar. In total, two or more vibrational quanta ($v_1 + v_2 \geq 2$) are needed to enable the formation of ArH^+ ions. These ArH^+ ions are single counted, making spectroscopy on only a few hundred H_3^+ ions possible [101].

5.2. Measurement procedure

For all measurements, the trap is kept at a nominal temperature of 60 K to prevent the Ar reactant gas to freeze out on the cold trap enclosure. At this temperature, the residual gas pressure, dominated by N_2, is 2.7×10^{-9} mbar, corresponding to a particle density of $\sim 2.3 \times 10^{9}\,cm^{-3}$ (see Tab. 5.1). The proton transfer reaction with N_2 governs the lifetime of H_3^+, which is around $2 - 3$ seconds. Ar and He are continuously fed into the trap. The argon number density is chosen in such a way

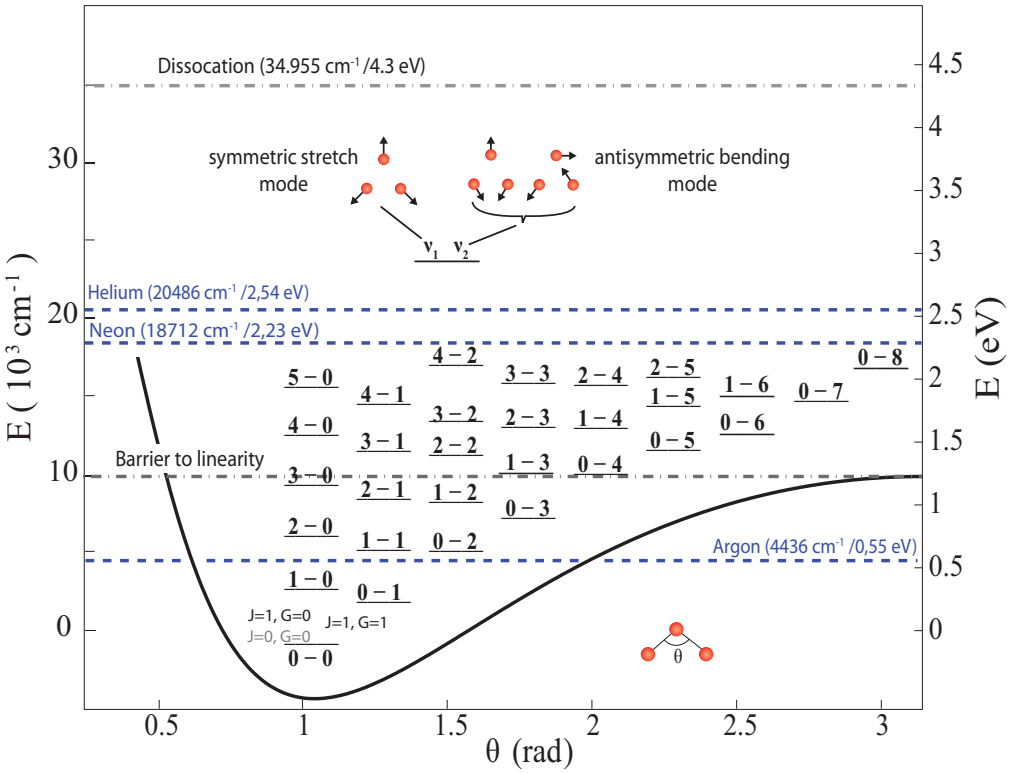

Figure 5.1. – Special representation of the H_3^+ potential energy surface [33]. Two H-H bond lengths are set to be equal and varied in length to find the minimum energy for a given angle θ between them. The barrier to linearity at around 10 000 cm^{-1} as well as the dissociation energy for the H_2 $+H^+$ channel at around 35 000 cm^{-1} are depicted by dash-dotted lines. Energetic thresholds for different probe gases are depicted by dashed lines. H_3^+ band origins are labeled according to the number of quanta in the symmetric stretch (degenerate antisymmetric) ν_1 (ν_2) mode [6]. The energy levels are given at arbitrary angles and illustrate the widening angle with increasing bending excitation.

that essentially all excited H_3^+ ions meet an Ar before they are cooled down below the Ar reaction barrier (4436 cm^{-1}) by the He buffer gas. In fact, the Ar most likely reacts with a particular laser-excited state of the H_3^+ ion as the time constant for Ar-H_3^+ collisions is shorter than the lifetime of the laser excited states (see App. E). The He pressure is set sufficiently high to quickly achieve thermalized translational cooling as well as cooling of the internal excitation of the trapped H_3^+ ions. H_2 from the ion source is permanently leaking into the trap and therefore restricting the pressure that may be used in the source. The residual H_2 pressure inside the trap determines the ArH^+ lifetime according to Eq. (5.1), which has an optimum

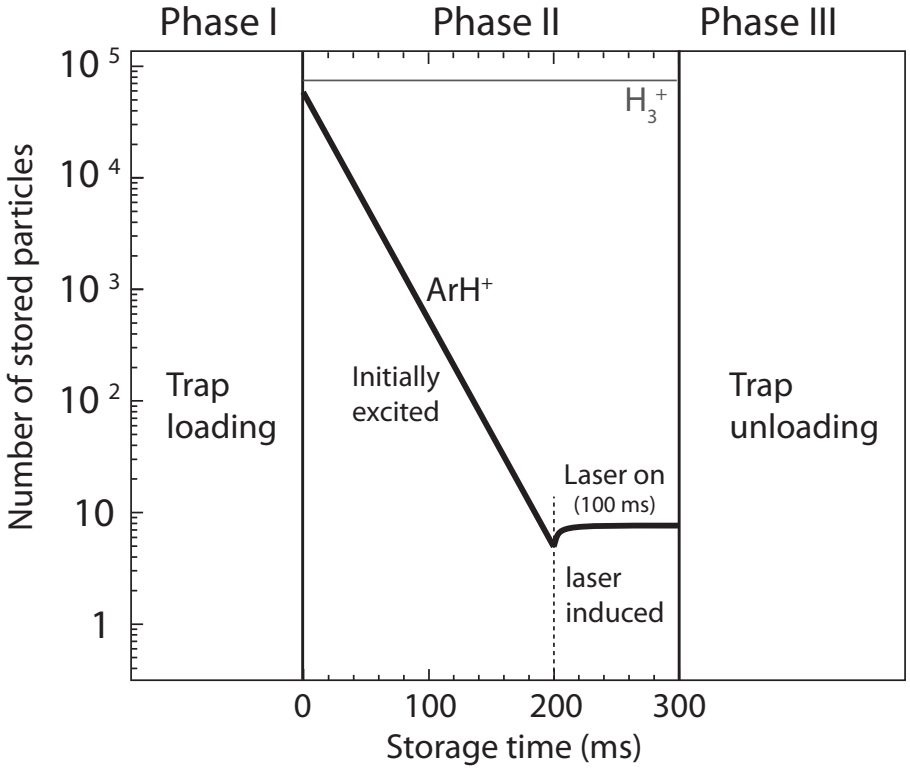

Figure 5.2. – Timing of a single trap filling at a specific laser frequency. The typical number of ArH^+ ions for a trap filling is shown schematically as a function of time after injection during a storage cycle (phase II). Preceding phase I, the desired laser wavelength is set and the actual wavelength and laser power are recorded. This takes about 600 ms and is therefore only repeated every 150 trap fillings (adjusted once in a minute). About 60 % of the produced H_3^+ are internally highly excited so that they immediatly form ArH^+. After 200 ms of storage, the average amount of ArH^+ ions, reacting back to H_3^+, has decayed to a small number and the laser is turned on for about 100 ms.

around ∼25 ms corresponding to 1.7 $\times 10^9$ H_2/cm^3. Long ArH^+ lifetimes increase the signal and therefore the sensitivity. The source, however, produces excited H_3^+ and before cooling, about 60% immediatly react to ArH^+, producing a non-laser induced background. A sufficiently low ArH^+ lifetime is therefore needed to allow for a fast decay (by back reaction) of this background, requiring an adequate H_2 trap pressure.

A typical trap filling is illustrated in Fig. 5.2. First the hot H_3^+ ions from the source are loaded into the 22-pole trap. Only a few ms are necessary to cool the H_3^+ ions to the lowest rotational states of the vibrational ground state but 200 ms

Table 5.2. – Measurements performed for each laser-frequency step within a frequency run. First, the number of H_3^+ is determined 10 times followed by the background measurement of ArH^+ (no laser). Then the ArH^+ is measured with laser and the whole procedure is repeated five times.

Trap fillings	Mass filter setting	Laser
1-10	H_3^+	off
11-20	ArH^+	off
21-30	ArH^+	on
31-40	H_3^+	off
...		
141-150	ArH^+	on

are needed to allow the ArH^+ background to decay to a level of typically 3-4 ions. Afterwards the laser interaction lasts for 100 ms to establish an equilibrium between laser excitation and decay. Directly after the laser interaction time τ_{LIT}, the ions are released, mass selected, and focused on the Daly type detection system where the single ions are counted. At each laser-frequency step within a frequency run, 150 trap fillings are completed (lasting $\sim$1 min) to successively count the H_3^+ and the ArH^+ ion number with and without laser interaction (see Tab. 5.2).

The ArH^+ count number is expected to be as small as 10^{-1} on average since we are searching for transitions as weak as $B_{lu} \sim 10^{16}\mathrm{cm^3J^{-1}s^{-2}}$. The H_3^+ number is orders of magnitude larger and maximized to attain the best signal-to-noise (S/N) ratio within the count range of the detection system. Here, the S/N ratio is defined as the number of laser-induced ArH^+ ions over the non-laser induced ions plus false counts due to ambient laser photons. Three distinct experimental schemes are used.

Scheme 1.: Line search

In the search for new transitions, a constant number of 10^5 H_3^+ ions are stored and cooled in the trap. The large amount of H_3^+ ions enhances the ArH^+ signal, but saturates the detection system. For the line search, the saturation is of no importance as the constant ion number eliminates the need to count the actual number of H_3^+ ions. In practice, the H_3^+ ion number is recorded to verify that it is steady. To minimize the search time, coarse laser frequency steps of $\sim$0.010 $\mathrm{cm^{-1}}$

are used. The speed of this scheme is faster than schemes 2 and 3 (explained next) by a factor of roughly 3. This step width ensures several measurement points to fall within the expected Doppler broadened line profile of the transition. The available laser output power is maximized by four passings through the trap setup as described in Sec. 4.2.1, Tab. 4.2. The rough scan for lines allow for $\sim$1 cm^{-1} to be covered a day.

Scheme 2.: Precise transition frequencies

Once a line is found, the precise transition frequency has to be determined. Therefore, finer laser frequency steps of 0.003 cm^{-1} are used. Again, four passings through the 22-pole trap as well as a large number of H_3^+ ions is employed. A transition frequency measurement takes typically 15 hours to reach good statistics. Precise transition frequencies (relative 0.001 cm^{-1}, absolute 0.005 cm^{-1}) are derived as center frequencies of Gaussian fits of the Doppler broadened line profiles.

Scheme 3.: Transition intensities

To determine the line intensities and to derive Einstein B_{lu} coefficients, extra care is taken to keep the experimental conditions constant, e.g., the pressure, lifetimes, and temperature. All parameters are carefully monitored. A single laser pass is used to accurately ascertain the laser power involved and fix the laser-ion-interaction region. The amount of H_3^+ ions is reduced to 10^4, preventing saturation of the detection system and correctly count the H_3^+ number. As the overlap of the laser beam with the ions is unknown, only relative intensities can be measured. Absolute normalization is achieved by normalizing to a reference line which is measured before and after each line-intensity measurement.

5.3. Sensitivity estimation

In the search for unmeasured predicted transitions, it is crucial to estimate the detection sensitivity of the chemical probing technique to select the expected observable transitions. The signal strength is given by the amount of laser-induced ArH^+ ions.

The formation rate, $k_{(J,G)}(\nu_L)$, of ArH^+ per H_3^+ ion for a transition with frequency ν_0 can be expressed by the following equation,

$$k_{(J,G)}(\nu_L) = \int f_{(J,G)}(\nu - \nu_0)\, B_{lu}\, \rho(\nu - \nu_L) d\nu, \tag{5.2}$$

where $f_{(J,G)}(\nu - \nu_0)$ denotes the fraction of the H_3^+ ions that resonantly interacts with the laser (center frequency ν_L, spectral energy density $\rho(\nu - \nu_L)$). The coupling strength of these ions to the laser field is given by the Einstein B_{lu} coefficient. The fraction $f_{(J,G)}(\nu - \nu_0)$ itself depends on the geometrical overlap between the ion distribution inside the trap and the laser beam. This overlap is unknown, but from the ratio of the laser cross-section and the trap cross-section can be estimated to be $A_L/A_{trap} \approx 5\,\%$. It is essential for relative normalization to retain the same overlap for all measurements by careful alignment of the laser beam (see Sec. 4.2.1), especially when considering the ion distribution inside the trap due to space charge effects and the influence of the trap end electrodes [109]. The interacting H_3^+ fraction is also dependent on the population of the initial rotational states $p_{(J,G)}$ and, due to the Doppler effect, also on the laser frequency. Thus $f_{(J,G)}(\nu - \nu_0)$ looks like

$$f_{(J,G)}(\nu - \nu_0) = p_{(J,G)}\, C\, e^{-(\nu-\nu_0)^2/2\sigma_D^2}\, \frac{A_L}{A_{trap}} \tag{5.3}$$

with the normalization constant $C = \sqrt{mc^2/2\pi k_B T \nu_0^2}$. The Doppler width, σ_D, can be described by the standard deviation

$$\sigma_D = \sqrt{\frac{k_B T}{mc^2}}\nu_0 \tag{5.4}$$

and reveals, due to the negligible laser line width, the translational temperature of the ions. This means that the spectral energy density $\rho(\nu - \nu_L)$ can be approximated by a δ-function times the energy density $P_L/A_L c$, with P_L denoting the laser power. Equation 5.2 can thus be simplified to

$$k_{(J,G)} = \frac{p_{(J,G)}\, B_{lu}\, P_L}{A_{trap}\, c} C e^{-(\nu_L-\nu_0)/2\sigma_D^2} \tag{5.5}$$

It should be noted here, that the formation rate is independent of the laser bandwidth, since at lower bandwidth less ions are addressed within the Doppler profile

but with higher spectral intensity. The number of ArH^+ ions that are formed can be given by the following differential equation

$$\frac{dN_{ArH^+}}{d\tau_{LIT}} = k_{(J,G)}(\nu_L)N_{H_3^+} - \frac{1}{\tau_{ArH^+}}N_{ArH^+} \tag{5.6}$$

where $(k_{(J,G)}(\nu_L)N_{H_3^+})$ is the formation rate of ArH^+ from H_3^+ and where the term $(\frac{1}{\tau_{ArH^+}}N_{ArH^+})$ describes the back reaction rate given in Eq. 5.1 with a time constant τ_{ArH^+}. The solution of this equation gives the total amount of ArH^+ ions that are formed within a given laser interaction time τ_{LIT}. When the number of H_3^+ ions is assumed to be constant during the τ_{LIT}, the total amount of ArH^+ ions is given by,

$$N_{ArH^+} = N_{H_3^+}k_{(J,G)}(\nu_L)\tau_{ArH^+}(1 - e^{-\tau_{LIT}/\tau_{ArH^+}}), \qquad N_{H_3^+} = const. \tag{5.7}$$

Assuming a simple, time-dependence of the H_3^+ ions, $N_{H_3^+} = N_0\, e^{-\tau_{LIT}/\tau_{H_3^+}}$, the total amount of ArH^+ ions is given by

$$N_{ArH^+} = -\frac{\tau_{H_3^+}\tau_{ArH^+}kN_0 \cdot \left(e^{-\tau_{LIT}(\tau_{ArH^+}-\tau H_3^+)/(\tau_{H_3^+}\tau_{ArH^+})} - 1\right) \cdot e^{-\tau_{LIT}/\tau_{ArH^+}}}{\tau_{ArH^+} - \tau_{H_3^+}} \tag{5.8}$$

with N_0 indicating the number of H_3^+ ions at the start of the laser interaction and $\tau_{H_3^+}$ indicating the H_3^+ lifetime. For H_3^+ lifetimes above 2 s, the time dependence of the H_3^+ is negligible as demonstrated in Ref. 102, p. 54. The Einstein B_{lu} coefficients enabling a pre-selection of expected observable transitions are obtained from theory. The calculations TEN96 and TEN07 (see Chap. 3) provide for all transitions Einstein A_{ul} coefficients for spontaneous decay. In the case of LIR experiments, the coefficient for laser absorption, the Einstein B_{lu} coefficient, is the crucial quantity. B_{lu} can be obtained through

$$B_{lu} = \frac{g_u}{g_l}\frac{c^3 A_{ul}}{8\pi h\nu^3}, \tag{5.9}$$

where g_u and g_l denote the rotational degeneracies $g = 2J + 1$ of the upper and lower states. Figure 5.3 shows the Einstein B_{lu} coefficients according to Ten96 for transitions starting from the two lowest rotational states (J=1, G=0,1) of the vibrational ground state. The red solid line indicates the expected detection sensitivity of the setup as follows from Eq. 5.7 assuming 0.6 W of laser power and 10 000 H_3^+

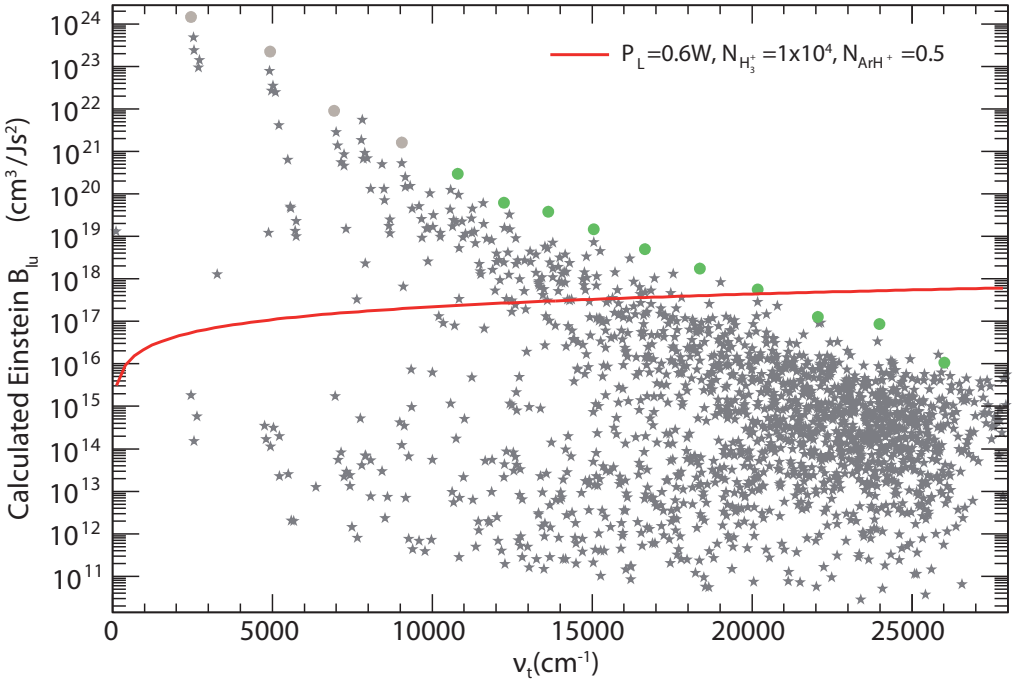

Figure 5.3. – Sensitivity estimation: Einstein B_{lu} coefficients from TEN96 [88] vs transition frequency. All transitions start from the vibrational ground state (J=1,G=0 or 1). The red solid line shows the expected sensitivity of our setup. The green filled circles indicate above the barrier to linearity transitions with higher transition intensity compared to the surrounding bulk states. Below the barrier to linearity these transitions are marked by filled grey circles.

ions. The minimum amount of laser-excited ArH^+ necessary for measuring a transition line profile depends on the particular settings of the experimental setup (ArH^+ background level) and measurement of interest and the measurement scheme used. In case of a line search, a S/N ratio of $\approx$1.125 is necessary. For precise frequency or intensity determination, a S/N$\approx$1.05 is sufficient. Assuming standard conditions of the experimental setup ($\sim$ 3-4 ArH^+ background ions), a signal of about 0.5 ArH^+ ions on average per trap filling are needed for the line search. As can be seen from Fig. 5.3, the current sensitivity limit should allow for observations of bulk states up to $\sim 18\,000\,\mathrm{cm}^{-1}$ and horseshoe states up to $\sim 20\,000\,\mathrm{cm}^{-1}$ should be observable.

6. Modifications on the 22 pole trap setup

This chapter treats the modifications on the experimental setup to render the measurements described in Chap. 7 and Chap. 8 possible. Below, first, the re-design of the 22-pole trap entrance- and exit electrodes is reported. Afterwards, an additional vacuum chamber for differential pumping that was installed between the ion source and the 22-pole trap is described. This includes the design of a bent rf quadrupole. Finally, the implementation of a slow extraction scheme for the H_3^+ ions is presented, which allows for the large dynamic count range required for measuring the number of H_3^+ and ArH^+ ions with the same detection system.

6.1. The entrance and exit electrodes of the trap

In the setup of the 22-pole trap described in Chap. 4, the end electrodes, used for confining the ions axially, consist of stainless steel tubes, 14 mm in length, 6.2 mm in diameter (see Fig. 6.1). They pass through the trap side plates (thickness 4 mm) protruding 4.5 mm inside the 22-pole trap and 6 mm outside. A ceramic tube (outer diameter 7.8 mm) is encasing the end electrodes to isolate them against the rf voltage applied to the side plates. No special dedicated mounting, fixing the electrode to the side plate, was foreseen. Two thin (0.4 mm in diameter) silver coated copper wires, connected to the electrode, deliver the selected voltage and are at the same time the fixing mechanism for the electrode. A Teflon plate is mounted onto the side plate on the outer side to prevent a shortcut between the silver coated copper wires and the trap side plates.

During the first NIR measurements above the barrier to linearity [32], strange fluctuations extending over many trap fillings occurred from time to time, even though

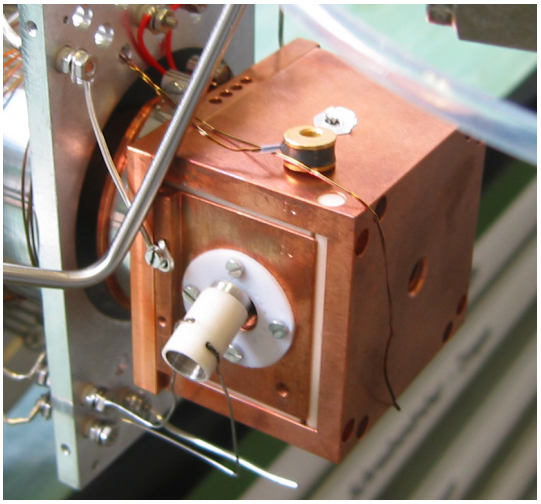

(a) Picture of the old electrode.

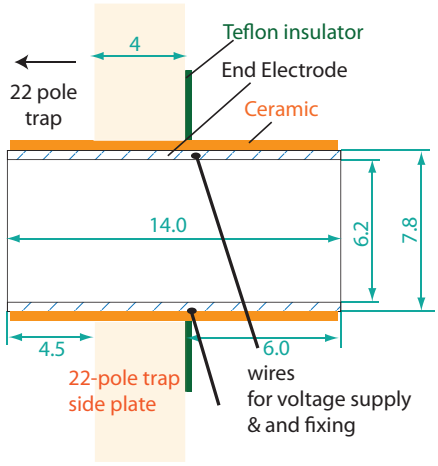

(b) Technical drawing of the old electrode design.

Figure 6.1. – The design of the old end electrodes used for the NIR measurements presented in this thesis.

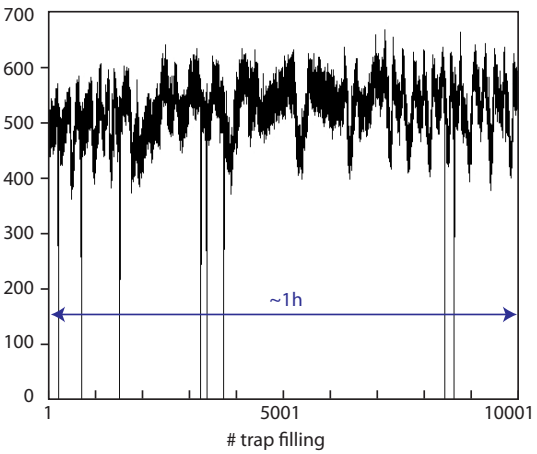

(a) The recorded H_3^+ ion number with the original trap electrodes.

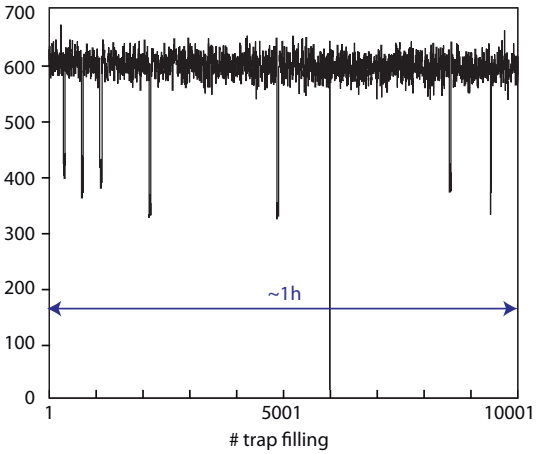

(b) The recorded H_3^+ ion number with the new trap electrodes.

Figure 6.2. – Number of H_3^+ ions vs. trap fillings as detected by the single-ion counting system (see Sec. 4.1).

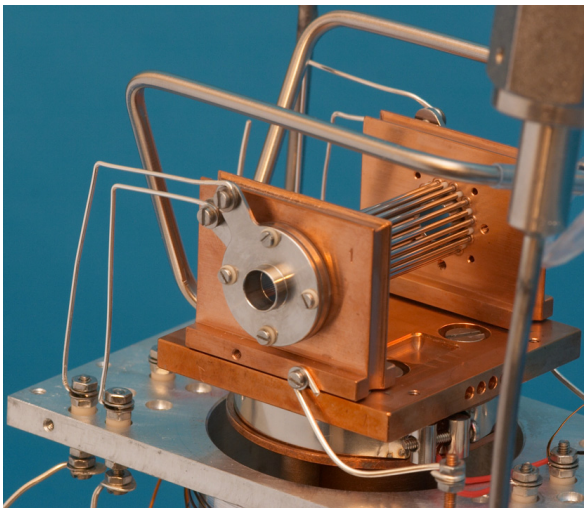

(a) Picture of the new electrode with their mounting.

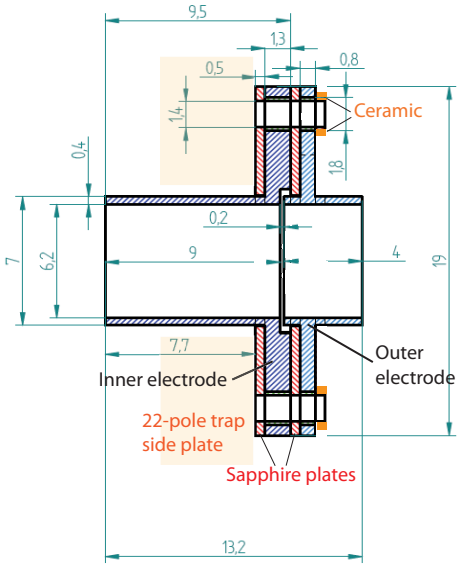

(b) Technical drawing of the new electrode design.

Figure 6.3. – The design of the new end electrodes used for the NIR to VIS measurements presented in this thesis.

experimental parameters were kept constant (see Fig. 6.2a). Remember that 150 trap fillings are needed for each single measurement point at a particular frequency (see Sec. 5.2). The fluctuations often occurred after several days of operation and were ascribed to charging up of mainly Ar-ice that might have been build up on any cold surface. The ceramic material was also suspected to be part of the problem. As the problem occasionally also occurred immediately after cooling down the 22-pole trap, another cause, either by itself or additionally, must be responsible. Careful inspection revealed that both end electrodes; the entrance and exit electrodes, had slightly moved from their initial position (1-2 mm). This motion can be caused by the vibrations of the cold head, where the trap is mounted on.

To solve this problem, new end electrodes have been designed. A photograph and the layout are shown in Fig. 6.3. The ceramic parts are located such that neither the ion beam nor the ions inside the trap can reach the ceramics, avoiding any possible charging effects. The new electrodes are split in an inner part passing the trap side plate and protruding inside the 22-pole trap and an outer part pointing outwards. Mounting of the electrode is done with 4 screws fixing the electrode directly onto the side plate. This anchorage allows for omitting the isolation between the inner

electrode and the duct of the trap side wall. Thin (0.5 mm) sapphire plates are utilized to isolate the inner electrode against the side plate and the outer electrode against the inner. The thermal conductivity κ of sapphire (κ=10 $\mathrm{Wcm^{-1}K^{-1}}$) is comparable to that of copper and more than one order of magnitude higher than that of a typical ceramic like Al_2O_3 (850 $\mathrm{mWcm^{-1}K^{-1}}$) [110]. Therefore, in contrast to the old electrodes, the new end electrodes are thermically well coupled to the copper trap housing.

The new end electrodes have led to fairly constant trap fillings, as can be observed in Fig. 6.2b. The few runaway values (<1%) where only about half the mean amount of ions is detected are negligible for the results of the measurements. Constant operation for more than 10 days has been successfully achieved.

6.2. Slow ion extraction

In Chap. 5 the need for a high dynamic range of the ion detection system is mentioned. The 22-pole trap is, in principle, able to store up to a few millions of H_3^+ ions. This was was demonstrated for operation at the storage ring TSR [111, 112]. For the first NIR spectroscopy experiments with the 22-pole trap setup, where single-ion counting is required, about 300 H_3^+ ions could be used. When planning to extend the spectroscopy of H_3^+ into the visible spectral region, detection limit estimations (see Sec. 5.3) showed that much more H_3^+ ions are needed. For the line search up to 18000 $\mathrm{cm^{-1}}$ at least 10000 H_3^+ ions are required. The expected corresponding ArH^+ signal is less than one on average. Therefore, a high dynamic detection system is required.

In previous trap experiments [32, 101], a fast extraction scheme was used. The ions were released by switching the exit electrode from a positive (+2 V) to a negative (−8 V) voltage, releasing all stored H_3^+ ions at once and, creating an H_3^+ pulse train of ∼40 μs (see Fig. 6.4a). This fast extraction limits the amount of H_3^+ ions that can be counted without saturating the detection system to a few hundred. Faster electronics and detectors can offer some enhancement, however, 10^4 timely equally distributed incoming ions within 40 μs already require a 250 MHz detection system. As the time between the impact of each single ion is not constant, an even higher count rate is required easily exceeding the MHz region. Ideas on using two different

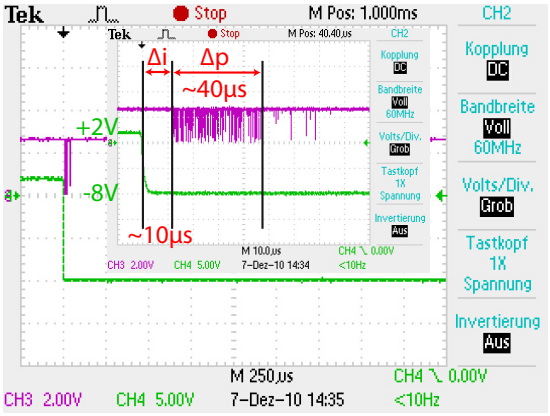

(a) H_3^+ ion-pulse train using the fast extraction. Delay $\Delta i \approx 10\,\mu s$ and pulse width $\Delta p \approx 40\mu s$.

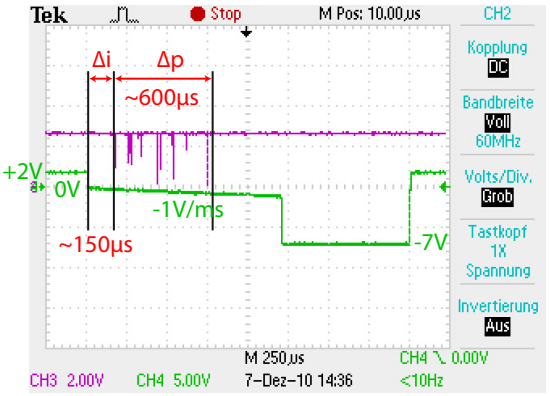

(b) H_3^+ ion-pulse train using a slow extraction. Delay $\Delta i \approx 150\,\mu s$ and pulse width $\Delta p \approx 600\mu s$.

Figure 6.4. – Comparison between the fast and slow ion extraction schemes of the 22-pole trap.

detectors, one single-ion counting for the ArH^+ measurement, and one integrating detector for the H_3^+ measurement were dismissed due to implementation difficulties.

A simpler and elegant solution is to lower the ion count rate for H_3^+ at the detector by lengthening the extracted ion-pulse train. A voltage ramp is applied to the inner exit electrode spreading the ion-pulse from $40\,\mu s$ to $0.5 - 1\,ms$, reducing the count rate to below 20 MHz for 10^4 ions. Figure 6.4b illustrates the pulse-train lengthening in the case of 10^4 ions. The voltage ramp may be adapted for any ion number or desired pulse length. By choosing the appropriate drop off voltage (0 V in Fig. 6.4b) the initial delay until the first ions arrive at the detector can be minimized to $\sim 10\mu s$. Detailed studies on the extraction ramp are given in Ref. 113. The proof of principle for this slow extraction scheme is demonstrated in Fig. 6.5. In this figure, the laser-induced ArH^+ signal is plotted against the number of stored H_3^+ ions as counted by the respective extraction schemes. In Fig. 6.5a, the amounts of ArH^+ and H_3^+ ions are measured using the fast extraction scheme. Clearly, above 1000 H_3^+ ions a non-linear behavior is observed. Recalling Eq. 5.7 into mind, the amount of laser formed ArH^+ ions should be linearly dependent on the number of H_3^+ stored inside the 22-pole trap. When using a slow extraction scheme for counting the H_3^+ ions, the expected linear behavior is observed (see Fig. 6.5b).

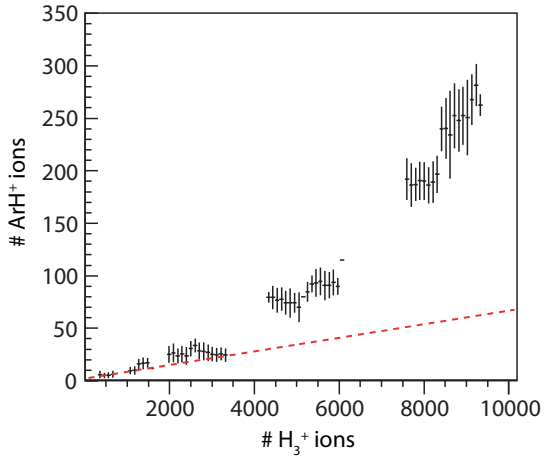

(a) The recorded laser-induced ArH^+ as function of H_3^+ number as counted by the fast extraction scheme. There is a clear non linearity due to the saturation of the detection system underestimating the real H_3^+ number.

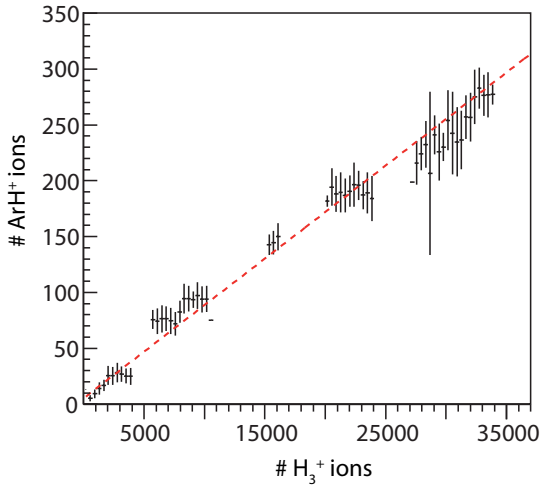

(b) The recorded laser-induced ArH^+ as function of H_3^+ number as counted by the slow extraction scheme. A clear linear behavior can be observed.

Figure 6.5.

6.3. Differential pumping section

A differential pumping section between the ion source and the 22-pole trap, reducing the flux of H_2 from the source into the trap, is favorable for two reasons. First, the allowed increase in H_2 pressure inside the ion source reduces the initial H_3^+ excitation and thereby the initial non-laser induced ArH^+. Second, the ArH^+ lifetime is not sacrificed by this H_2 pressure increase due to the differential pumping and optimal signal strengths may be achieved (see Sec 5.2). Additionally, low H_2 densities reduce the number of collisions between H_3^+ and H_2. This is of importance when studying or controlling the H_3^+ ortho and para populations and behavior. Such was the case for the investigation of the dissociative recombination of cold H_3^+, where the 22-pole trap setup was used as ion injector for the storage ring TSR. The reader is referred to Refs 51, 114, 112 for more detailed information. The application at the storage ring, or more precisely, the high-voltage platform cage supporting the TSR ion sources prohibited a linear extension of the setup as shown in Fig. 4.1. To stay within the spatial restrictions, the ion source of the 22-pole trap setup and the adjacent linear quadrupole had to be turned by 90° and moved upwards as shown in Fig. 6.6.

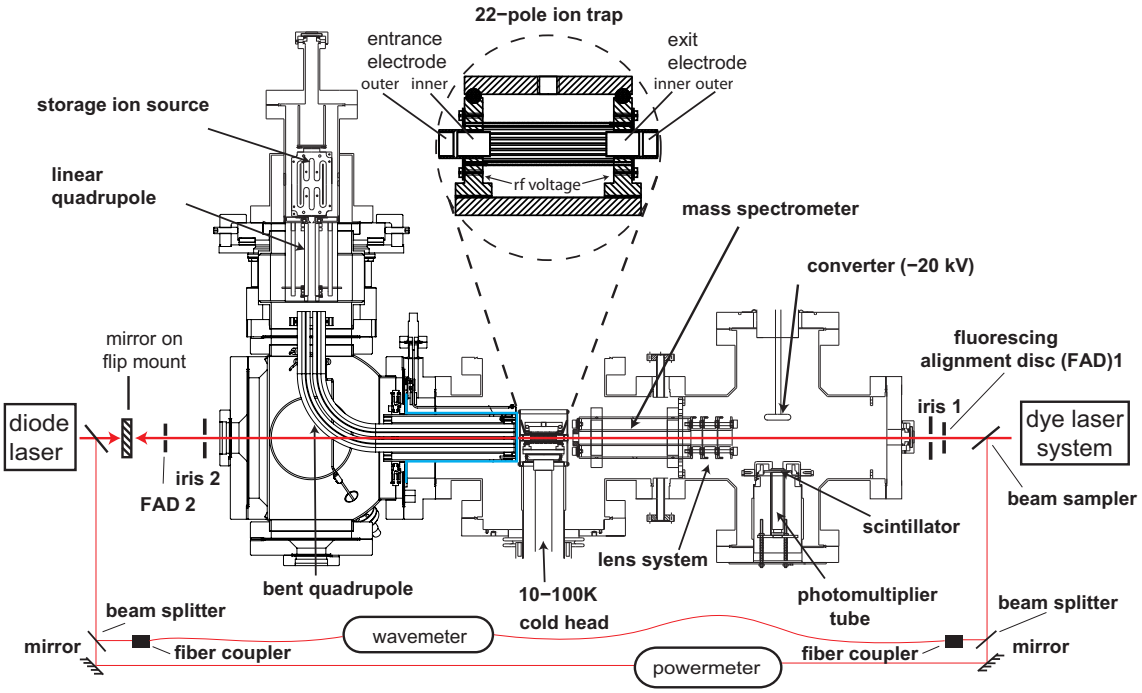

Figure 6.6. – The 22-pole trap setup after implementation of the new electrodes and the differential pumping chamber holding the bent quadrupole. Also shown is a schematic of the laser beam alignment and monitoring.

Conceptual design

Two different conceptual designs have been simulated with SIMION[1] as shown in Fig. 6.7. The first concept is a standard design to deflect ions by 90° (see Fig. 6.7a). It consists of two linear quadrupoles and, in between, a static quadrupole deflector to bend the ions. The inner free radius and the radius of the rods for the linear quadrupoles are chosen to be R_0 =4.36 mm and R_{rod} =5 mm, respectively. For ion mass 3 and 0.5 eV ion energy, the simulation shows that the first linear quadrupole is capable of collecting all ions from an assumed initial 3 mm parallel beam out of the ion source. For the low energetic ions the static quadrupole deflector looses about 50% of the ions. When assuming divergent ions coming from the source the simulation shows that for appropriate voltage and frequency settings up to ±40° of the tilted ions are still captured into the first linear quadrupole. Only ions up to ± 10° divergence pass all the way through both linear quadrupoles and the static

[1]SIMION Industry standard charged particle optics simulation software Version 8

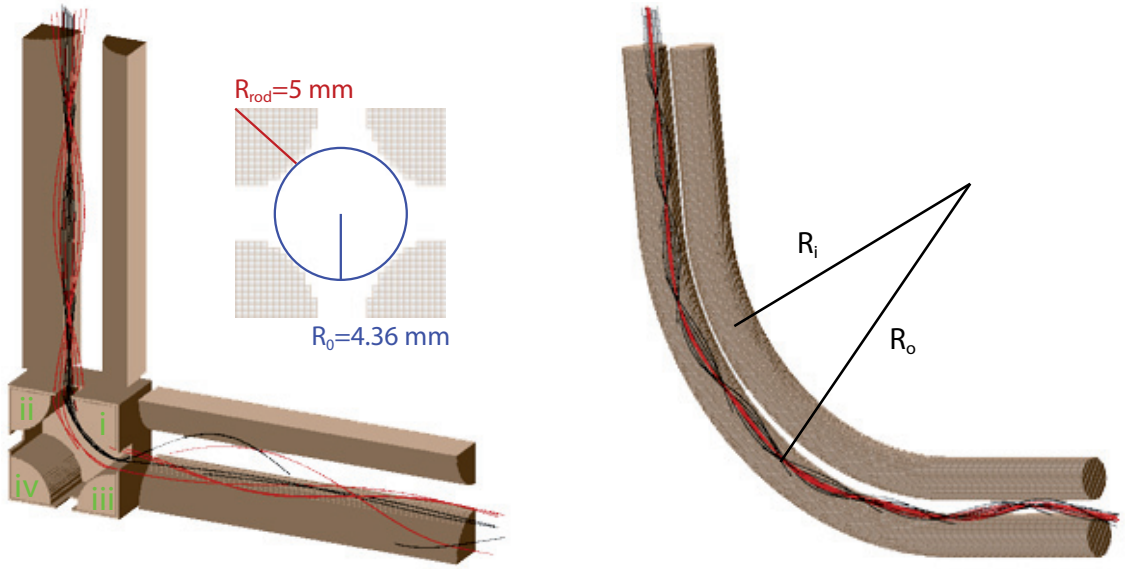

(a) Static quadrupole deflector **(b)** RF bent quadrupole

Figure 6.7. – SIMION simulations for the static quadrupole deflector and for the rf bent quadrupole. In both cases simulated ion traces are shown for different divergence of the ions coming from the source. The inner free radius and the radius of the rods for the linear quadrupoles in (a) being the same as for the bent rf quadrupole in (b) is given as inset. The used rf is 16 MHz at V_{pp} =10 V. The static voltages are i= −0.3 V, ii= +0.5 V, iii= +0.5 V, and iv= +0.4 V.

quadrupole deflector.

In Fig. 6.7b the static quadrupole deflector is replaced by a bent rf quadrupole directly connected to the linear ones. In fact, the bent quadrupole including the linear parts is one element. The dimensions of R_0 and R_{rod} are the same as above. The inner radius and the outer radius of curvature are R_i = 60.0 mm and R_o = 73.23 mm respectively. Simulations show that ions (mass 3 to mass 30 were tested) with up to 40° divergence are guided all the way through the bent rf quadrupole.

Realization

The bent rf quadrupole system was chosen due to its superior guidance performance. The technical sketch as well as a photograph of the realized bent rf quadrupole are shown in Fig. 6.8. It is made out of aluminum coated with a thin gold layer to offer the conductance needed for the rf. The dedicated mounting allows for proper

alignment of the bent quadrupole to the 22-pole trap (see Fig. 6.8b). The alignment to the ion source is realized via four adjustment screws tilting a bellow connection towards the ion source (6.8c). The measured capacitance between the two rod pairs of the quadrupole is 55 pF, the capacitance between each rod pair and ground is 60-70 pF. The Q-factor[2] is determined to be ∼36.

Vacuum considerations

The quality of the differential pumping is determined by the total conductance of the bent quadrupole chamber compared to a direct CF 100 connection as in the original setup. The housing of the bent quadrupole (see Fig. 6.8a) already confines the gas and reduces the conductance compared to a CF 100 connection ($\sim 2000\,\mathrm{ls}^{-1}$ for H_2) by a factor of 3. The shielding electrode has a thin (0.5 mm) aperture of 8.7 mm in diameter. The Conductance C for a thin aperture of area A is given by [115]

$$C = \frac{\bar{v}}{4}A \tag{6.1}$$

where $\bar{v}$ is the mean thermal speed assuming a Maxwell-Boltzmann velocity distribution

$$\bar{v} = \sqrt{\frac{8k_BT}{\pi m_p}}, \tag{6.2}$$

k_B being the Boltzmann constant, T the temperature, and m_p the mass of the gas particle. The conductance for the aperture is $25\,\mathrm{ls}^{-1}$. The total conductance between bent quadrupole chamber and trap chamber is $\sim 23\,\mathrm{ls}^{-1}$. Additionally, an Leybold Turbovac 361 turbomolecular pump is attached to the bent quadrupole vacuum chamber. The H_2 pressure inside the 22-pole trap chamber is reduced by one order of magnitude compared to the bent quadrupole chamber. The pressure difference between the ion source and the 22-pole trap is estimated to be more than two orders of magnitude.

[2] The quality factor Q is a measure of the sharpness of the resonance peak. It equals the resonant frequency divided by the width at -3 dB.

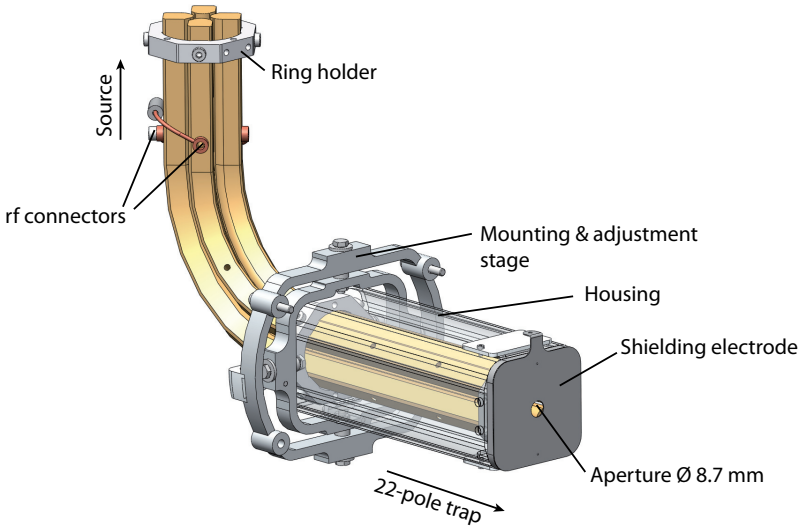

(a) Technical drawing of the bent quadrupole, its adjustment stage, and its housing to shield gas from flowing to the 22-pole trap other than through the 8.7 mm aperture.

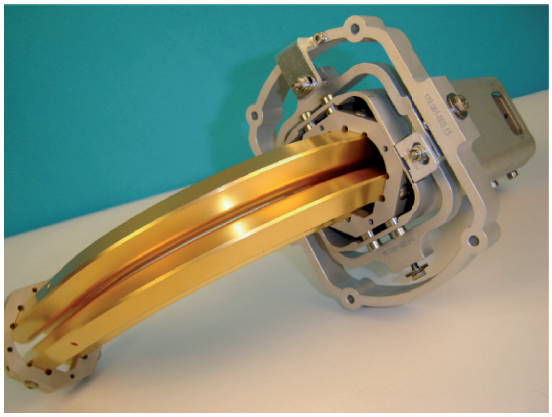

(b) The bent quadrupole mounting and housing.

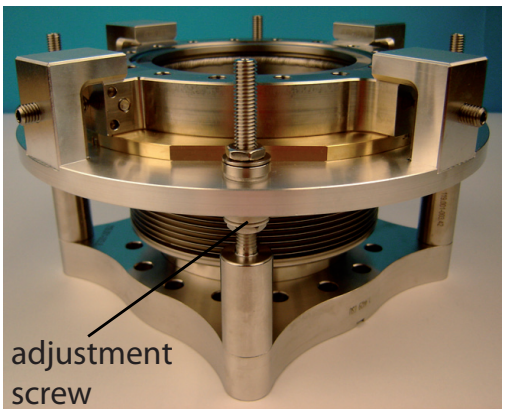

(c) The bellow adjustment stage for alignment to the ion source.

Figure 6.8. – Technical drawing and photographs of the bent quadrupole and the adjustment stages for alignment to the 22-pole trap and to the ion source.

Part III.

Results & Discussion

7. Transition frequencies

Precise transition frequencies are of utmost importance for theoretical progress in treating polyatomic molecules beyond the Born-Oppenheimer approximation as described in Chapter 3. This chapter presents the high-resolution spectroscopic results for transition frequencies from the two lowest rotational states of the vibrational ground state to final levels above the barrier to linearity using NIR to VIS light. The assignment of the observed transitions is described and a detailed discussion comparing the results with various theoretical predictions is given.

7.1. Results and data analysis

In this work, 37 transitions with frequencies between $10750 - 16700\,\mathrm{cm}^{-1}$ are reported in total. All experimental transition frequencies are listed in Tab. 7.1 along with the experimental parameters and theoretical strengths. Below $14000\,\mathrm{cm}^{-1}$, 23 transitions have been measured with the unmodified experimental setup (see Chap. 4) [32]. Three theoretically weaker transitions (see last column in Tab. 7.1) in this range and all transitions above $14000\,\mathrm{cm}^{-1}$ have been measured with the improved setup (see Chap. 6). Figure 7.1a shows a typical example for a measured transition in the NIR spectral region whereas Fig. 7.1b is a typical example for a measured transition in the VIS spectral region. For the first time seven transitions right into the visible spectral region are measured involving 7, 8, and 9 vibrational quanta in the ν_2 mode.

The natural line width of all measured transitions is below 1 kHz. The laser line width of the used laser systems (see Sec. 4.2) is large (>75 kHz) compared to the natural line width but small compared to the temperature induced Doppler width inside the trap (>300 MHz). The pressure inside the trap is low enough to prevent significant pressure broadening. Therefore, the natural line width as well as any

Table 7.1. – The experimentally determined transition frequencies and their reduced experimental parameters as well as their predicted transition strengths. The listed H_3^+ numbers are those directly counted and might for transitions labeled with superscript a include saturation effects. The used laser system (see Sec. 4.2) is given in the last column.

ν_m (cm^{-1})	$\#H_3^+$ ($\times 10^3$)	T (K)	runs	τ_{ArH^+} (ms)	$\overline{P_L}$ (mW)	$B_{lu,Ten96}$ ($cm^3 J^{-1} s^{-2}$)	laser system
10752.161(05)	8	86	5	21	135	2.18×10^{19}	TiSa (LW)
10798.777(05)	9	79	5	21	190	3.00×10^{20}	TiSa (LW)
10831.681(05)	7	84	8	22	250	9.40×10^{19}	TiSa (LW)
11228.598(10)[a]	0.4	76	2	31	570	2.59×10^{19}	TiSa (LW)
11244.350(10)[a]	5-6	73	4	17	460	1.19×10^{19}	TiSa (LW)
11258.975(10)[a]	3-4	71	16	23	470	4.47×10^{19}	TiSa (LW)
11342.587(10)[a]	4-5	77	17	23	380	6.78×10^{18}	TiSa (LW)
11465.505(10)[a]	4-5	75	11	23	420	2.20×10^{18}	TiSa (LW)
11511.373(10)[a]	4-5	70	20	22	420	1.29×10^{18}	TiSa (MW)
11594.276(10)[a]	3-4	71	13	27	400	6.08×10^{19}	TiSa (MW)
11707.257(10)[a]	3-5	67	3	25	490	5.83×10^{18}	TiSa (MW)
11707.797(10)[a]	4	82	3	21	470	1.16×10^{19}	TiSa (MW)
11882.376(10)[a]	15-16	68	12	16	500	1.68×10^{18}	TiSa (MW)
12018.812(10)[a]	4	71	2	21	480	2.46×10^{18}	TiSa (MW)
12086.738(10)[a]	4-11	69	29	12	500	2.77×10^{18}	TiSa (MW)
12239.242(10)[a]	4-5	74	12	15	580	6.15×10^{19}	TiSa (MW)
12373.526(10)[a]	6-7	71	3	30	500	4.04×10^{18}	TiSa (MW)
12381.137(10)[a]	6-7	73	12	19	600	1.48×10^{18}	TiSa (MW)
12413.247(10)[a]	3	72	8	29	450	3.36×10^{19}	TiSa (MW)
12419.127(10)[a]	5	81	6	21	530	1.16×10^{18}	TiSa (MW)
12588.951(05)	6-7	84	6	24	600	3.09×10^{17}	TiSa (MW)
12620.223(05)	12	85	6	24	650	1.75×10^{18}	TiSa (MW)
12623.160(10)[a]	3	76	19	23	450	9.05×10^{18}	TiSa (MW)
12678.688(10)[a]	2-11	83	3	24	480	2.88×10^{18}	TiSa (MW)
12881.635(05)[a]	10	83	4	24	450	4.54×10^{17}	TiSa (SW)
12897.877(10)[a]	1-3	68	12	27	400	2.68×10^{18}	TiSa (SW)
13055.994(10)[a]	0.6-0.9	69	11	25	320	4.33×10^{18}	TiSa (SW)
13071.590(10)[a]	2-3	>55	3	25	360	2.52×10^{18}	TiSa (SW)
13332.884(10)[a]	6	85	7	25	220	9.24×10^{17}	TiSa (SW)
13638.251(05)	13	81	84	25	398	3.72×10^{19}	TiSa (SW)
15058.680(05)	10	84	37	24	420	1.46×10^{19}	Dye (DCM)
15130.480(05)	22	86	25	23	348	7.12×10^{17}	Dye (DCM)
15450.112(05)	19	83	17	24	420	2.79×10^{17}	Dye (DCM)
15643.052(05)	11	84	35	23	420	3.65×10^{17}	Dye (DCM)
15716.813(05)	10	84	38	23	500	1.40×10^{18}	Dye (DCM)
16506.139(05)	18	89	15	25	480	5.31×10^{17}	Dye (Rhod. B)
16660.240(05)	21	88	12	27	450	4.90×10^{18}	Dye (Rhod. B)

[a] published in Ref. 32; higher uncertainty as Li-spectroscopy not available on a regularly basis

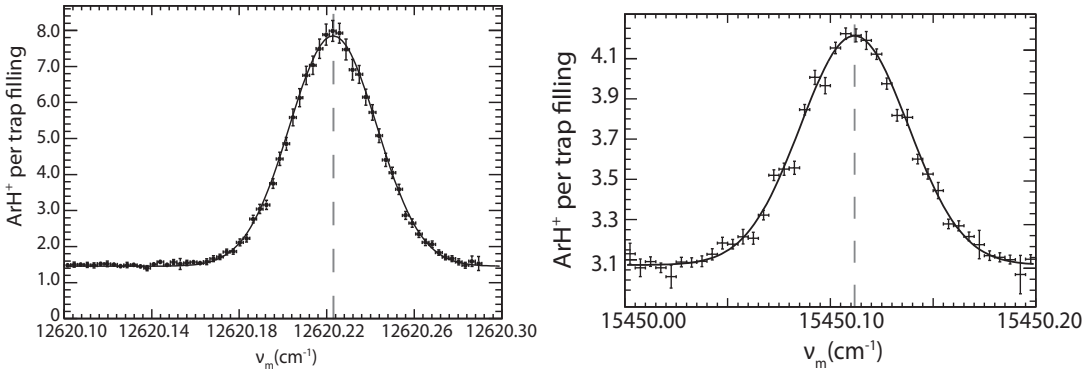

(a) The measured transition ${}^{n}\mathrm{R}(1,1)$, $2\nu_1{+}3\nu_2^3 \leftarrow 0$ with center frequency $(12620.223{\pm}0.005)\,\mathrm{cm}^{-1}$.

(b) The measured transition ${}^{t}\mathrm{R}(1,0)$, $1\nu_1{+}6\nu_2^2 \leftarrow 0$ with center frequency $(15450.112{\pm}0.005)\,\mathrm{cm}^{-1}$.

Figure 7.1. – Two measured lines illustrating the perfect Gaussian shape. The ArH^+ signal is recorded using scheme 2.

broadening effect apart from the Doppler broadening are negligible. The measured spectra show perfect Gaussian line profiles for all spectral regions as can be seen in Fig. 7.1. The Doppler profile f_D can be described by

$$f_D = \frac{1}{\sqrt{2\pi}\sigma_D} e^{-(\nu-\nu_m)^2/2\sigma_D^2}, \tag{7.1}$$

where ν_m is the center frequency and the Doppler width σ_D is given by

$$\sigma_D = \sqrt{\frac{k_B T}{mc^2}}\nu_m, \tag{7.2}$$

k_B being the Boltzmann constant, T the translational temperature, m the mass and c the speed of light.

The translational temperature of all measured transitions has been derived from this Doppler width. The determined temperature for all intensity measurements (see scheme 3 Chap. 8) is ∼85 K, about 25 K higher than the nominal temperature of the 22-pole trap. This deviation can be explained by the unfavorable ion-to-neutral mass ratio in collisions between H_3^+ and Ar in combination with a rather high voltage (+2 V) on the entrance and exit electrodes of the trap [109]. For the frequency determination measurements (see scheme 2 Chap. 5) the derived temperatures vary between 55-89 K as no extra care is taken for these kinds of measurements to keep

the translational temperature constant.

7.2. Assignment

The correct assignments of the energy levels involved in the respective transitions are not always trivial and essential to verify and help theory advance. For all transitions reported here, the corresponding J and G quantum numbers for each of the line lists TEN96, ALI03, and ALI03$_c$ match. Except for three cases, the vibrational quantum numbers (v_1,v_2) accordant to the line list ALI03 and ALI03$_c$ are also assigned.

In general, the assignment process becomes more and more difficult the higher the energy levels that are involved. This holds for the initial as well as the final levels. The assignment towards higher energies gets more complicated by the increasing state density and additionally the decreasing accuracy of theoretical predictions in general. This renders absorption spectroscopy in a discharge cell where many states are initially populated, an unfavorable approach for investigation of high lying states. Only two transitions starting from a vibrationally excited state ($1\nu_2$, $\sim 2600\,\mathrm{cm}^{-1}$) have been assigned so far [31]. Of all transitions measured with absorption spectroscopy, 25 transitions above $10\,800\,\mathrm{cm}^{-1}$ could not be assigned. Figure 7.2 demonstrates this issue. Figure 7.2a shows all possible candidate transitions, the lower level restricted to be below $2600\,\mathrm{cm}^{-1}$, within $\pm 10\,\mathrm{cm}^{-1}$ for the measured frequency at $(12678.688 \pm 0.010)\,\mathrm{cm}^{-1}$. Although the experimental uncertainty is low, the theoretical uncertainty can go up to several wavenumbers. Transitions that are predicted to be too weak to be observed could be excluded (in this case 29). This however still leaves 31 possible candidates and no definite assignment can be made.

The assignment process can be greatly simplified when starting from the two lowest rotational levels of the vibrational ground state only, as is the case for the action spectroscopy in the 22-pole trap. Not having the population distributed over many levels also benefits the signal strength. The cooling of the H_3^+ ions therefore reduces the amount of possible candidates tremendously as can be observed in Fig. 7.2b. A unique assignment is now possible as the second possible candidate only arises when the energetically seventh lowest rotational level ($J = 3, G = 1$) is significantly populated. At standard 22-pole trap conditions, this state, lying 619 K higher than the lowest rotational state is only populated by $10^{-2}\,\%$.

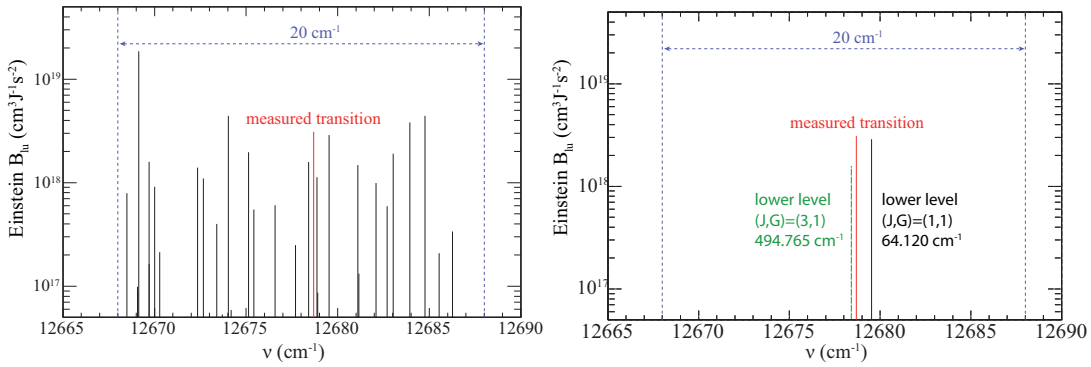

(a) high temperature **(b)** low temperature

Figure 7.2. – Assignment for the 12678.688 cm^{-1} transition. The experimental value for the frequency and Einstein B_{lu} coefficient is given as red solid line. Also shown are calculated transition frequencies and intensities from TEN96. In (a) the initial states lie below 2600 cm^{-1} and are restricted to $J \leq 10$, whereas in (b) one transition starts from the two lowest rotational states (black line) and one transition starting from the energetic seventh lowest rotational state (green dashed line)

The NIR to VIS transitions presented in Tab. 7.1 could be well assigned as the frequency spacing between predicted neighboring transitions is larger than the scattering of the different theories as displayed in Fig. 7.3a. In four cases a simple transition frequency analysis was insufficient. As shown in Fig. 7.3b, the line spacing overlaps the scattering between theories and no unique assignment can be given based on frequency analysis alone. Table 7.2 lists all measured lines and gives a comparison to values from the ALI03$_c$ line list. The last two columns indicate the difference in frequency from the experimental value to the next possible lower (higher) calculated transition frequency. This difference is in general much bigger than the deviation from the assigned theoretical value to the measured one given in column four. There are four exceptions, marked with light grey, where the allowed nearby transitions show about the same deviation as the assigned one. These transitions having ambivalent assignment are also listed in Tab. 7.3.

In the case of the 10 752.161(05) cm^{-1} transition, comparison to other line lists does not give a unique identification either. Also the Einstein B_{lu} coefficients are comparable and strong. The candidate from the energetic third rotational state denoted by P(2,2), although only weakly populated, would in this case still be more than strong enough to be measured. A unique identification could however be achieved through the characteristics of the initial state. The respective candi-

Table 7.2. – The assignments of the NIR to VIS measured transition frequencies ν_m. Vibrational and rotational transition labels are given according to Sec. 2.2 using A. Alijah corrected line list 2003 [36]. Predicted states that could also match the measured transition when considering frequency alone are marked in grey.

Vibration	Rotation	ν_m (cm^{-1})	ALI03$_c$-ν_m (cm^{-1})	ALI03$_{c,l}$-ν_m (cm^{-1})	ALI03$_{c,h}$-ν_m (cm^{-1})
$2\nu_1+2\nu_2^3 \leftarrow 0$	P(1,0)	10752.161(05)	−0.594	−45.944	0.176
$5\nu_2^1 \leftarrow 0$	P(1,1)	10798.777(05)	−0.046	−33.354	32.815
$5\nu_2^1 \leftarrow 0$	Q(1,0)	10831.681(05)	−0.089	−32.950	12.763
$5\nu_2^1 \leftarrow 0$	R(1,0)	11228.598(10)[a]	−0.060	−41.741	15.737
$5\nu_2^1 \leftarrow 0$	$R(1,1)^u$	11244.350(10)[a]	−0.015	−15.812	14.131
$3\nu_1+1\nu_2^1 \leftarrow 0$	P(1,1)	11258.975(10)[a]	−0.494	−14.640	45.376
$3\nu_1+1\nu_2^1 \leftarrow 0$	Q(1,1)	11342.587(10)[a]	−0.483	−25.037	10.264
$3\nu_1+1\nu_2^1 \leftarrow 0$	$R(1,0)^l$	11465.505(10)[a]	−0.557	−41.023	37.590
$3\nu_1+1\nu_2^1 \leftarrow 0$	$R(1,1)^u$	11511.373(10)[a]	−0.485	−8.278	6.360
$5\nu_2^5 \leftarrow 0$	$^{-6}$P(1,1)	11594.276(10)[a]	−0.412	−14.720	8.056
$5\nu_2^5 \leftarrow 0$	$^{-6}$R(1,1)	11707.257(10)[a]	−0.152	−12.425	0.118
$5\nu_2^5 \leftarrow 0$	$^{-6}$Q(1,1)	11707.797(10)[a]	−0.422	−0.692	11.711
$1\nu_1+4\nu_2^0 \leftarrow 0$	^{n}R(1,1)	11882.376(10)[a]	−0.616	−28.105	40.006
$1\nu_1+4\nu_2^2 \leftarrow 0$	^{t}Q(1,0)	12018.812(10)[a]	−0.626	−4.466	16.307
$1\nu_1+4\nu_2^2 \leftarrow 0$	^{t}R(1,1)	12086.738(10)[a]	−0.379	−51.619	10.410
$2\nu_1+3\nu_2^1 \leftarrow 0$	P(1,1)	12239.242(10)[a]	−0.598	−4.610	6.270
$2\nu_1+3\nu_2^1 \leftarrow 0$	Q(1,1)	12373.526(10)[a]	−0.516	−38.255	6.516
$2\nu_1+3\nu_2^1 \leftarrow 0$	R(1,1)	12381.137(10)[a]	−1.095	−8.127	31.584
$6\nu_2^2 \leftarrow 0$	P(1,1)	12413.247(10)[a]	−0.526	−33.205	3.457
$6\nu_2^2 \leftarrow 0$	^{t}Q(1,0)	12419.127(10)[a]	−0.711	−2.423	10.667
$2\nu_1+3\nu_2^1 \leftarrow 0$	R(1,1)	12588.951(05)	−0.366	−17.586	23.620
$2\nu_1+3\nu_2^3 \leftarrow 0$	^{n}R(1,1)	12620.223(05)	−1.214	−7.652	2.373
$6\nu_2^2 \leftarrow 0$	Q(1,1)	12623.160(10)[a]	−0.564	−4.151	8.981
$6\nu_2^2 \leftarrow 0$	^{t}R(1,1)	12678.688(10)[a]	−0.608	−15.389	22.320
$6\nu_2^2 \leftarrow 0$	$^{-6}$R(1,1)	12881.635(05)	−1.023	−62.188	15.354
$1\nu_1+4\nu_2^4 \leftarrow 0$	^{t}R(1,0)	12897.877(10)[a]	−0.888	−17.265	9.684
$6\nu_2^2 \leftarrow 0$	^{t}R(1,0)	13055.994(10)[a]	−0.822	−45.224	14.845
$2\nu_1+3\nu_2^3 \leftarrow 0$	R(1,1)	13071.590(10)[a]	−0.751	−16.418	20.771
$3\nu_1+1\nu_2^4 \leftarrow 0$	^{t}R(1,1)	13332.884(10)[a]	−1.183	−2.367	10.786
$7\nu_2^1 \leftarrow 0$	^{x}P(1,1)	13638.251(05)	−1.872	−26.362	8.333
$8\nu_2^2 \leftarrow 0^b$	^{n}P(1,1)	15058.680(05)	−2.653	−9.699	1.588
$1\nu_1+6\nu_2^2 \leftarrow 0^b$	^{n}Q(1,1)	15130.480(05)	−3.234	−7.486	3.254
$1\nu_1+6\nu_2^2 \leftarrow 0^b$	^{t}R(1,0)	15450.112(05)	−1.304	−2.038	18.466
$\geq 6^c$	^{x}R(1,0)	15643.052(05)	−1.914	−3.496	40.809
$\geq 6^c$	^{x}Q(1,1)	15716.813(05)	−2.501	−24.975	5.280
$\geq 6^c$	^{x}R(1,0)	16506.139(05)	−4.982	−13.300	18.651
$9\nu_2^1 \leftarrow 0^b$	^{x}P(1,1)	16660.240(05)	−5.089	−9.504	4.758

[a] published in Ref. 32

[b] Vibrational quantum numbers provided by ALI10b$_c$ (see Sec. 7.3)

[c] Exact vibrational quantum numbers unknown

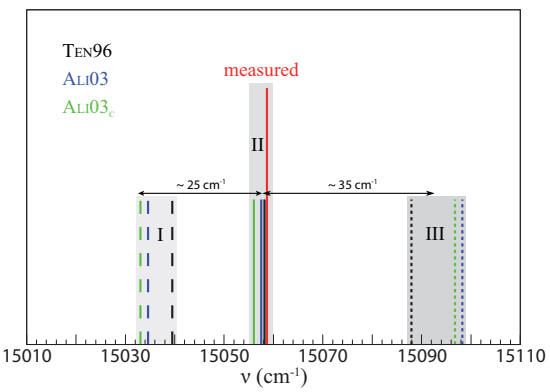

(a) The measured line frequency at $(15058.680 \pm 0.005)\,\mathrm{cm}^{-1}$. The line was identified to equal the ${}^{n}\mathrm{P}(1,1)$, $8\nu_2^2 \leftarrow 0$ transition as listed in Tab. 7.2.

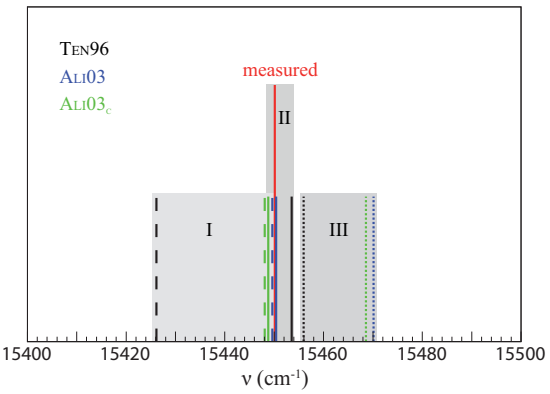

(b) The measured line frequency at $(15450.112 \pm 0.005)\,\mathrm{cm}^{-1}$. The line was finally identified to equal the ${}^{t}\mathrm{R}(1,0)$, $1\nu_1{+}6\nu_2^2 \leftarrow 0$ transition as listed in Tab. 7.2 using the transition intensity information of TEN96.

Figure 7.3. – Assignment for energetically high-lying transitions. The grey boxes labeled I, II, III, denote each the wavenumber interval spanned by various line lists for three transitions closest to the measured line frequency. In (a), the measured line is clearly assigned to the transition II. In (b) frequency considerations alone are insufficient to reach a definite assignment.

date transitions in this case start from the ortho (1,0) and para (2,2) levels. Their population may be modified by manipulation of the H_3^+ ortho-to-para spin ratios. This can be achieved by either changing the temperature inside the trap or by using para-H_2 as parent gas for the H_3^+ production, leading to an enhancement in para-H_3^+. Here, the assignment is based on comparison with a previous experiment from C. P. Morong *et al.* [31]. For their assignment C. P. Morong *et al.* use pressure variations and additional theoretical predictions by J. K. G. Watson as described in [116]. About ten of the transition frequencies reported in Ref. 31 have been remeasured here for comparison as well as for the intensity measurements. As can be observed in Tab. 7.4, the previous and current measurements agree within $10^{-2}\,\mathrm{cm}^{-1}$ [1]. The transition at $10752.161\,\mathrm{cm}^{-1}$ marked in grey, however, deviates by roughly $0.2\,\mathrm{cm}^{-1}$ from the transition reported in Ref. 31, indicating that these are not the same transitions. The one from Ref. 31 is stated to belong to the para species, i.e., the (2,2) initial state. The currently measured $10752.161\,\mathrm{cm}^{-1}$ is therefore assigned to the

[1] The results measured in the group of T. Oka [30, 117] show a systematic trend to lie slightly higher in frequency, although the values were already lowered in the latest publication [31]

Table 7.3. – Theoretical candidate transitions for measured lines that cannot be assigned based on transition frequency alone. The final assignments after further considerations are marked in grey. The Einstein B_{lu} coefficients are predictions from Ref. 88.

ν_m (cm^{-1})	ΔJ(J,G)$_l$	ALI10b$_c$ (cm^{-1})	ALI03$_c$ (cm^{-1})	TEN96 (cm^{-1})	$B_{lu,\mathrm{TEN96}}$ ($cm^3J^{-1}s^{-2}$)
10752.161					
	P(1,0)	10751.61	10751.567	10753.417	2.18×10^{19}
	P(2,2)	10752.42	10752,337	10752.270	9.39×10^{19}
11707.257					
	R(1,1)	11707.60	11707.105	11708.272	5.825×10^{18}
	P(1,1)	11707.87	11707.375	11708.855	1.159×10^{19}
11707.797					
	R(1,1)	11707.60	11707.105	11708.272	5.825×10^{18}
	P(1,1)	11707.87	11707.375	11708.855	1.159×10^{19}
15450.112					
	Q(1,1)	15434.55	15448.07	15426.16	3.25×10^{15}
	R(1,0)	15451.24	15448,81	15453.517	2.79×10^{17}

ortho transition denoted as P(1,0) in Tab. 7.3. For the two cases 11707.257 cm^{-1} and 11707.797 cm^{-1}, the assignment follows the ascending order of the transition frequency in the predictions as both are measured. The transition at 15450.112 cm^{-1} is assigned by using the transition intensity information from TEN96 (see Tab. 7.3). The nearby candidate has a too low predicted Einstein B_{lu} coefficient and so the expected line intensity is well below the current sensitivity limit of the experiment.

7.3. Deviations between theory and experiment

The comparison of all 37 measured transition frequencies to the theoretical values from the TEN96, ALI03, and ALI03$_c$ line lists, as introduced in Chap. 3, is displayed in Fig. 7.4 as $\Delta\nu = \nu_t - \nu_m$ for transition frequencies above 12000 cm^{-1}. The differences $\Delta\nu$ are also listed in Tab. 7.5. Since for low lying states close to the equilibrium

Table 7.4. – Comparison between the transition frequencies ν_m presented here that were also measured by Oka and co., ν_{Oka} [31]. The experimental uncertainty in both experiments is maximally $0.010\,\mathrm{cm}^{-1}$. All units are in cm^{-1}.

ν_m	ν_{Oka} [31]	$\nu_m - \nu_{Oka}$
10752.161(05)	10752.369(10)	-0.208
10798.777(05)	10798.785(10)	-0.008
10831.681(05)	10831.677(10)	0.004
11228.598(10)	11228.601(10)	-0.003
11244.350(10)	11244.353(10)	-0.003
11707.257(10)	11707.268(10)	-0.011
11707.797(10)	11707.801(10)	-0.004
12419.127(10)	12419.140(10)	-0.013
12897.877(10)	12897.888(10)	-0.011
13055.994(10)	13056.013(10)	-0.019

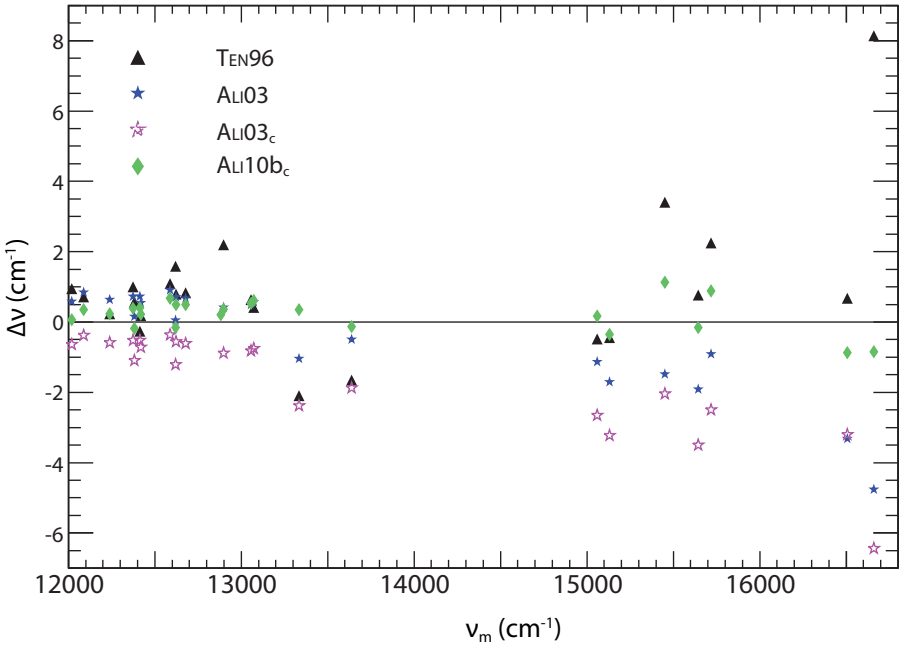

Figure 7.4. – Frequency deviations between theory and experiment $\Delta\nu = \nu_t - \nu_m$ for the given line lists. Note that the scale ν_m starts at $12000\,\mathrm{cm}^{-1}$, way above the barrier to linearity.

theoretical calculations and experiments agree within spectroscopic accuracy, the discrepancies in transition frequencies are ascribed to inaccuracies of the predictions on the *upper* energy level. The TEN96 calculations tend to overestimate the upper energy levels. The deviations are outside the predicted accuracy (see Sec. 3.3.1) of up to $\pm 1\,\mathrm{cm}^{-1}$ at $15000\,\mathrm{cm}^{-1}$ [88]. Previous publications [30, 117, 32, 31] have reported that the uncorrected calculation ALI03 systematically overestimates the transition frequency by up to $1\,\mathrm{cm}^{-1}$. This is however only valid below $\sim$13100 cm^{-1}; higher predicted transition energies are systematically too low. As the predictions are based on variational calculations, they are expected to be higher than the true values indicating that the PES is slightly too wide in this energy region [6]. The corrected predictions from ALI03$_c$ deliver spectroscopic accuracy for transitions below $9000\,\mathrm{cm}^{-1}$ (Fig. 4 in [29]). For energy levels above $10000\,\mathrm{cm}^{-1}$, the correction is overshooting and all values systematically underestimate the real transition frequencies with increasing discrepancy towards higher states.

Ali10b$_c$

Recently, a new line list has been published [6] using all measured data [32, 31], including the present ones, to arrive to an updated empirical correction. The line list resulting from the improved values is referred to as ALI10b$_c$. Because the underlying PES is the same as for the ALI03 line list, the uncorrected values ALI10b correspond to ALI03. In contrast to the simple approach in ALI03, the empirical correction formula (see Eq. (3.19)) has been adapted to describe also higher energy levels up to dissociation. The higher energies require a more sophisticated correction formula as illustrated by the known H_2 [118, 119] non-adiabatic corrections displayed in Fig. 7.5. The energy shift due to non-adiabatic corrections is only initially linear. At higher energies, it passes through a minimum and tends to zero at dissociation. Thus all available experimental data is employed to fit the deviations between calculation and experiment $\Delta = E_t - E_m$ to a quadratic function in E_t

$$\Delta = c_1 E_t + c_2 E_t^2, \tag{7.3}$$

leading to

$$E_c = (1 - c_1 - c_2 E_t) E_t. \tag{7.4}$$

Table 7.5. – Comparison of the measured center frequencies ν_m with various line lists. All units are in cm^{-1}.

ν_m (cm^{-1})	TEN96-ν_m	ALI03/10b-ν_m	ALI03C-ν_m	ALI10b$_c$-ν_m
10752.161(05)	1.256	0.489	-0.594	-0.551
10798.777(05)	-0.245	1.043	-0.046	0.013
10831.681(05)	-0.190	0.999	-0.089	-0.011
11228.598(10)	0.245	1.072	-0.060	0.182
11244.350(10)	0.229	1.120	-0.015	0.230
11258.975(10)	1.592	0.645	-0.494	-0.245
11342.587(10)	1.609	0.663	-0.483	-0.187
11465.505(10)	1.672	0.605	-0.557	-0.195
11511.373(10)	1.618	0.677	-0.485	-0.103
11594.276(10)	0.876	0.764	-0.412	0.024
11707.257(10)	1.015	1.033	-0.152	0.343
11707.797(10)	1.058	0.763	-0.422	0.073
11882.376(10)	0.945	0.584	-0.616	-0.016
12018.812(10)	0.947	0.588	-0.626	0.068
12086.738(10)	0.713	0.842	-0.379	0.352
12239.242(10)	0.230	0.638	-0.598	0.228
12373.526(10)	1.002	0.734	-0.516	0.394
12381.137(10)	0.568	0.153	-1.095	-0.187
12413.247(10)	-0.256	0.733	-0.526	0.403
12419.127(10)	0.185	0.543	-0.711	0.233
12588.951(05)	1.086	0.909	-0.366	0.679
12620.223(05)	1.589	0.057	-1.214	-0.153
12623.160(10)	0.797	0.710	-0.564	0.500
12678.688(10)	0.834	0.672	-0.608	0.492
12881.635(05)	2.250	0.275	-1.023	0.205
12897.877(10)	2.200	0.413	-0.888	0.363
13055.994(10)	0.636	0.496	-0.822	0.536
13071.590(10)	0.413	0.570	-0.751	0.610
13332.884(10)	-2.094	-1.043	-1.183	0.346[a]
13638.251(05)	-1.646	-0.491	-1.872	-0.131
15058.680(05)	-0.488	-1.131	-2.653	0.169
15130.480(05)	-0.438	-1.700	-3.234	-0.350
15450.112(05)	3.405	-1.482	-1.304	1.128
15643.052(05)	0.763	-1.912	-1.914	-0.162
15716.813(05)	2.252	-0.913	-2.501	0.887
16506.139(05)	0.672	-4.982	-3.199	-0,869
16660.240(05)	8.143	-5.089	-6.440	-0,850

[a] ambivalent assignment, an alternative candidate deviates by only -0.834 cm^{-1}.

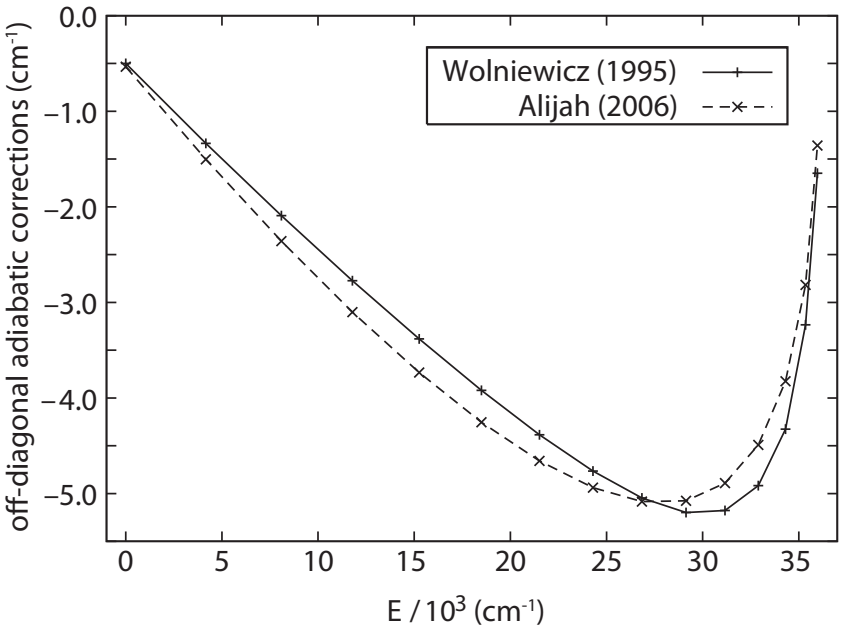

Figure 7.5. – Non-adiabatic corrections in H_2. Figure taken from Ref. 120

The coefficients are $c_1 = 3.84773 \times 10^{-8} \pm 10.7\%$ and $c_2 = 5.05287 \times 10^{-4}\,cm \pm 11.1\%$ [6]. A correction formula valid over the whole energy range up to $17\,000\,\mathrm{cm}^{-1}$ is obtained by joining Eq. (3.19) and Eq. (7.4) by the switching function

$$T(E) = \left[1 - e^{\gamma(E-E_0)}\right]^{-1} \tag{7.5}$$

with switching energy E_0 =10 700 cm^{-1} and the smoothness parameter γ =0.002 cm [6]. This leads to

$$E_c^{(v)} = [(1-b_1)E_t]T(E_t) + [(1-c_1-c_2E_t)E_t][1-T(E_t)]. \tag{7.6}$$

The new corrections proposed by A. Alijah cannot be claimed to result from non-adiabatic interactions alone but also have to originate from shortcomings of the PES at higher energies [6].

The comparison between the updated line list ALI10b$_c$ and the present measurements is also displayed in Fig. 7.4 (green diamonds). The deviations of the predictions are significantly smaller and scatter below and above the experimental values (see also Tab. 7.5). Up to 15000 cm^{-1} all values lie within 0.7 cm^{-1} of the experimental values, five of them are even better than 0.08 cm^{-1}. The assignment of

our measured transitions based on ALI10b$_c$ is equivalent to the one based on ALI03$_c$ (see Tab. 7.2), only one transition now has an ambivalent assignment as the new line list offers a second candidate for the 13332.884 cm^{-1} transition. The deviation of the first candidate to the measurement is however still smaller ($\Delta\nu$ =0.346 cm^{-1}) than that of the second candidate ($\Delta\nu$ =−0.834 cm^{-1}), favoring the original assignment (see Tab. 7.5). The highest transition frequency 16660.240 cm^{-1} seems to be badly reproduced by all calculations except ALI10b$_c$ that already includes this line in the empirical correction. This line is the only one so far measured involving 9 vibrational quanta. The new line list ALI10b$_c$ also offers some vibrational quantum numbers for states above 15000 cm^{-1}, not provided before by ALI03$_c$ (see Tab. 7.2). However, three measured transitions are still missing explicit vibrational quantum number assignment. Energetic considerations suggest that the upper states of the three exceptions involve at least 6 vibrational quanta.

None of the calculations are able to provide the reported estimated accuracy (see Sec. 3.3). Direct comparisons to the supposed superior line lists TEN09 and ALI10a (see Chap. 3) are not listed. Neither the TEN09 predictions using a mass scaling approach for simulating non-adiabatic effects, nor the values from ALI10a, using an accurate global PES suited to study non-adiabatic effects, allow for clear assignment as deviations between theory and experiment scatter randomly with deviations up to 20 cm^{-1}. This is a surprising result and further investigations will have to enlighten the issues afflicting these next-phase calculations, where non-adiabatic effects are *ab initio* taken into account.

8. Transition intensities

In the previous chapter accurate transition frequencies have been presented enlighting the higher energy region of the PES, comparing calculated eigenvalues with experiment. This chapter reports first measured Einstein B_{lu} coefficients for H_3^+ above the barrier to linearity, allowing not only to compare calculated eigenvalues, but to go one step further and also allow for comparison of calculated eigenfunctions with experiment. As the calculations from A. Alijah do not obtain eigenfunctions, all results are compared with the calculation TEN96 from J. Tennyson. Below, the experimental procedure to derive the measured transition intensities is described followed by the results and a discussion comparing the obtained intensities with theory.

8.1. Determination of transition intensities

As mentioned before in Sec. 5.3, the line lists TEN96 and TEN09 contain Einstein A_{ul} coefficients that can be converted into Einstein B_{lu} coefficients (see Eq. (5.9)). These Einstein B_{lu} coefficients provide a measure for the transition intensities. The experimental Einstein B_{lu} coefficients presented in this thesis are obtained in two steps. First, relative transition intensities are measured. Then absolute intensities are derived by normalization to a well known reference transition. About 6 transitions can be normalized during 10 days of continuous trap operation period, defined as the time between cooling down and warming up of the 22-pole trap.

8.1.1. Relative intensities

The amount of laser-induced ArH^+ is direct proportional to the Einstein B_{lu} coefficient (see Eq. (5.7)). The Einstein B_{lu} coefficient can be expressed as

$$B_{lu} = C' \frac{N_{ArH^+} \nu_0 \sqrt{T}}{N_{H_3^+} p_{(J,G)} P_L \tau_{ArH^+} \left(1 - e^{-\tau_{LIT}/\tau_{ArH^+}}\right)} \tag{8.1}$$

with

$$C' = \frac{A_{trap}\sqrt{2\pi k_B}}{\sqrt{m}}. \tag{8.2}$$

and with N_{ArH^+} the number of laser-induced ArH^+, $N_{H_3^+}$ the number of H_3^+, $p_{(J,G)}$ the population of the lower state, P_L the laser power, T the temperature, ν_0 the center frequency, τ_{ArH^+} the ArH^+ lifetime, τ_{LIT} the laser interaction time, m the H_3^+ mass, and A_{trap} the trap cross section.

Most parameters are set or can be measured. The τ_{LIT}, set via the computer control, is constantly 100 ms for all measurements. The amount of $N_{H_3^+}$ is kept as constant as possible and is permanently monitored. The same holds for the P_L, where a beam sample is recorded throughout the experiment. Transition frequencies ν_0 are accurately determined (see Chap. 7). The ArH^+ as well as the H_3^+ lifetime are regularly measured before and after each line measurement. Test measurements where the lifetime is determined every 20 min while slightly changing the H_2 pressure, have confirmed the expected correlation between pressure changes and lifetime. Further tests revealed that changes in the total pressure results mainly from changes in the H_2 pressure. Therefore, the permanent monitored total pressure is a qualitatively measure how constant the ArH^+ lifetime stays during a line measurement. In average the total pressure stayed constant within $\pm$ 5 % and so did the lifetimes. This is in good agreement with the lifetime measurements before and after each line measurement.

The N_{ArH^+} cannot be measured directly. The amount of detected ArH^+ always contains a non-laser induced background (see Sec. 5.2), and in the case of NIR transitions, an additional background from the laser photons that are counted by the PMT as no dedicated optical filter blocks the laser light in this wavelength region (see description of the Daly-type detection system Sec. 4.1). This laser photon background depends on the particular laser frequency and hence has to be determined

for each line separately.

All intensity measurements are normalized to the H_3^+ number as well as the laser power, that is changing with the frequency and, for the dye laser, also with time (see Fig. 4.4). Remember that the H_3^+ ions are not equally distributed over the trap volume, requiring a fixed H_3^+ number and interaction region between the laser and the ions (see Sec. 4.2). Equation 8.1 is not taking this inhomogeneity into account and therefore only relative intensity measurements can be performed.

8.1.2. Absolute intensities

The absolute intensity is obtained by normalization to the well known reference transition ($3\nu_2^1 \leftarrow 0$ R(1,1)) in the NIR at 7144.235 cm^{-1} with a theoretical Einstein B_{lu} coefficient of $5.6 \times 10^{20}\,cm^3 J^{-1} s^{-2}$ [121, 29, 88]. The theoretical value is assumed true as theory is quite accurate for low overtone transitions. The reference line is measured before and after each intensity measurement (see Fig. 8.1). The high transition strength of this line provides enough intensity information after 2 runs only.

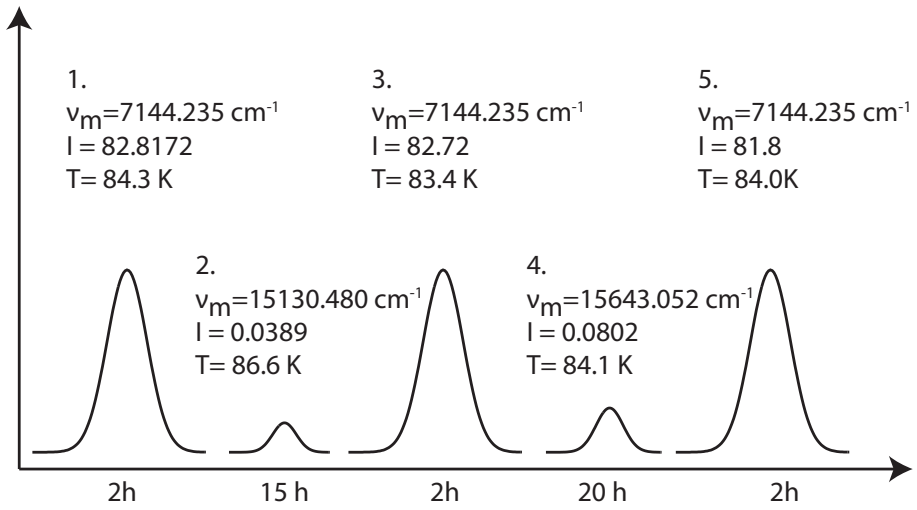

Figure 8.1. – Showcase of a measurement cycle for intensity determinations. For all 5 schematically represented measurements the respective center frequency ν_m, the line intensity I, normalized to 10^4 H_3^+ ions and 500 mW, the temperature T , and the duration of the measurements are given. The reference line is measured for about 2 hours before and after each NIR or VIS transition, which is measured for several hours. This scheme is repeated for all normalized measurements.

The reference line is a para-H_3^+ transition starting from the lowest para-H_3^+ state (J,G)=(1,1). Hence, the population term $p_{(J,G)}$ in Eq. (8.1) cancels out for absolute normalization of para transitions starting from this lower state. A correction is required for transitions starting from the ortho (1,0) state, depending on the rotational population distribution. In the high-temperature equilibrium realized in the ion source, the ortho-to-para ratio is expected to be 1:1. The ratio in the cryogenic trap is dependent on the number of H_3^+ spin conversions by collisions with H_2 or chemical reactions, determining whether ortho/para equilibrium is attained or not. Appendix E gives an overview of the H_3^+ collision times with the different gases inside the trap. From Tab. E.1, it follows that each H_3^+ collides on average once with an H_2 per trap filling. The exact number of collisions required for conversion to equilibrium values depends on the particular theoretical model, but in all models, a few collisions are statistically necessary to attain equilibrium. Collisions with Ar happen 3 orders of magnitude more frequently and when an excited H_3^+ ion collides with Ar this leads to a chemical reaction. As the H_3^+ ions are coming hot from the ion source (see Sec. 5.2) they immediatly react with the Ar and back again. Together with the collisions between H_3^+ and H_2 the rotational levels are assumed to be thermally distributed. The energetic reaction barrier for the reactions H_3^+ +He is much higher than for Ar (see Tab. 2.2) and therefore these collisions are considered to be elastic and do not influence the ortho-to-para ratio.

Table 8.1. – Maxwell Boltzmann population for the lowest rotational states. Population is given in % for the three lowest rotational states. B indicates a Maxwell Boltzmann distribution with spin interconversions. For o=p an initial ortho/para ratio of 1:1 cooling down without allowing for nuclear spin conversion is assumed.

T (K)	(1,1)		(1,0)		(2,2)		higher states	
	B	o=p	B	o=p	B	o=p	B	o=p
60K	42.9	43.1	49.7	49.5	5.7	5.8	1.7	1.6
80K	36.9	37.6	48.9	48.1	9.3	9.5	4.9	4.8
85K	35.6	36.3	48.4	47.6	10.0	10.2	6.0	5.9
90K	34.4	35.1	47.8	46.9	10.7	10.9	7.1	7.0

In Tab. 8.1 the relative populations of the lowest rotational states is listed for the two cases of either allowing ortho/para nuclear spin conversion or not. As can be seen, the relative population for the given temperatures are within a few tenth

of a percent the same. This leads to an negligible additional uncertainty for ortho transitions.

8.2. Results

Transition intensities in the form of Einstein B_{lu} coefficients have been derived for 18 transitions listed in Tab. 8.2. Four transitions are ortho transitions, not starting from the same lower state as the reference line. Energetically, 3 transitions are measured in the long-wave Ti:sapphire laser mirror spectral region, 6 in the mid-wave region and 2 in the short-wave region. In the VIS spectral region all 7 found transitions, measured with the Dye laser, have been normalized. Among the 18 transitions, 5 transitions connecting the vibrational ground state with the horseshoe states, expected to possess high transition probabilities, have been measured. In Fig. 8.2 four line profiles normalized to 10^4 H_3^+ ions and 500 mW laser power are shown. Figures 8.2a and b show NIR transitions, displaying the strongest measured transition and one of the horseshoe transitions, respectively. Figures 8.2c and d depict VIS transitions. Both are horseshoe transitions, Fig. 8.2d belonging to the transition with the highest frequency. From Fig. 8.2a to 8.2d the transition probability decreases. This is reflected by decreasing statistics of the measurement. Each line is normalized according to the previous section, the line intensity given by the fitted area of the Gaussian profile.

The error from fitting each individual line intensity varies between a few up to $\sim$50% in the worst case shown in Fig. 8.2d. To reduce the error in the fits, the following restrictions are made: The center frequency parameter range is set according to the precise frequency measurements presented in Chap. 7. In addition, for each trap operation period, the mean translational temperature is derived from all reference transition measurements. In the case of all 5 DCM lines this results in an average temperature of (84.8$\pm$2.4) K. This translational temperature must be the same for the transition intensity measurements performed in between the reference measurements. The parameter range for the Doppler width in the fit is thus limited according to Eq. 5.4. A fit is finally obtained including these restrictions giving a more accurate intensity value.

Another error is introduced by the deviations between different reference measure-

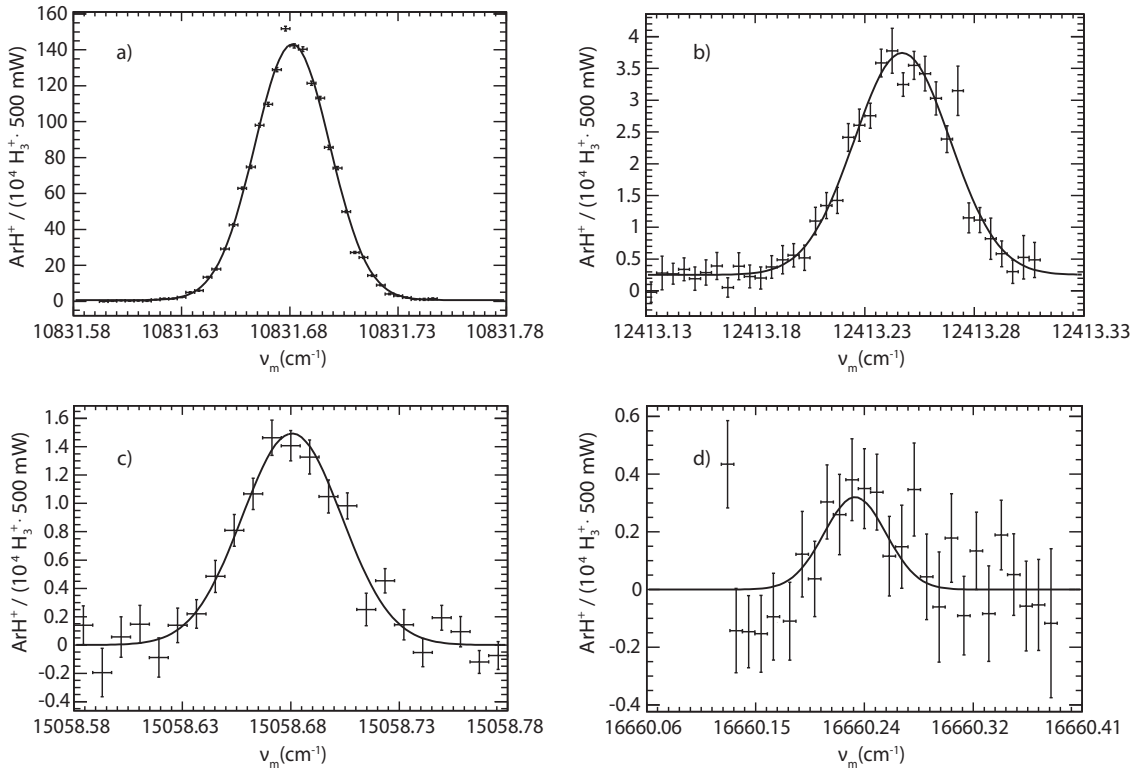

Figure 8.2. – Normalized transition line profiles. Figure a) shows the strongest measured transition. Figure b) and c) depict transitions to horseshoe states. The weakest, highest in transition frequency and at the same time also a horseshoe transition is shown in Fig. d).

ments. These reference line intensities agree with each other within a few percent up to ∼14% in the worst case. Transitions in the NIR contain an additional uncertainty resulting from the detected laser photons. This has to be accounted for when determining the line intensity. Other systematic errors such as the uncertainty in the laser power calibration (see Sec. 4.2.1) or the constancy of ArH^+ lifetime are negligible. The individual errors for each transition are listed in Tab. 8.2.

Table 8.2. – The normalized measured transitions and their derived absolute transition intensities. The assignments are as in Tab. 7.2

Assignment Vibration	Assignment Rotation	ν_m (cm^{-1})	$B_{lu,m}$ $cm^3J^{-1}s^{-2}$	$B_{lu,\text{TEN96}}$ $cm^3J^{-1}s^{-2}$	$B_{lu,\text{TEN96}}/B_{lu,m}$
$2\nu_1+2\nu_2^3\leftarrow 0$	P(1,0)^{o}	10752.161(05)	$2.64\pm0.58\times10^{19}$	2.18×10^{19}	0.83
$5\nu_2^1\leftarrow 0$	P(1,1)	10798.777(05)^{h}	$9.62\pm1.09\times10^{18}$	3.00×10^{20}	31.19
$5\nu_2^1\leftarrow 0$	Q(1,0)^{o}	10831.681(05)	$4.06\pm0.58\times10^{19}$	9.40×10^{19}	2.32
$2\nu_1+3\nu_2^1\leftarrow 0$	Q(1,1)	12373.526(10)	$1.55\pm0.36\times10^{18}$	4.04×10^{18}	2.61
$2\nu_1+3\nu_2^1\leftarrow 0$	R(1,1)	12381.137(10)	$1.50\pm0.37\times10^{18}$	1.48×10^{18}	0.99
$6\nu_2^2\leftarrow 0$	P(1,1)	12413.247(10)^{h}	$1.67\pm0.42\times10^{18}$	3.36×10^{19}	20.12
$2\nu_1+3\nu_2^1\leftarrow 0$	R(1,1)	12588.951(05)	$4.01\pm1.39\times10^{17}$	3.09×10^{17}	0.77
$2\nu_1+3\nu_2^3\leftarrow 0$	^{n}R(1,1)	12620.223(05)	$2.28\pm0.45\times10^{18}$	1.75×10^{18}	0.77
$6\nu_2^2\leftarrow 0$	^{t}R(1,1)	12678.688(10)	$3.11\pm0.61\times10^{18}$	2.88×10^{18}	0.93
$3\nu_1+1\nu_2^2\leftarrow 0$	^{t}R(1,1)	13332.884(10)	$1.46\pm0.47\times10^{18}$	9.24×10^{17}	0.63
$7\nu_2^1\leftarrow 0$	^{x}P(1,1)	13638.251(05)^{h}	$1.42\pm0.53\times10^{18}$	3.72×10^{19}	26.20
$8\nu_2^2\leftarrow 0$	^{n}P(1,1)	15058.680(05)^{h}	$5.58\pm1.21\times10^{17}$	1.46×10^{19}	26.16
$1\nu_1+6\nu_2^2\leftarrow 0$	^{n}Q(1,1)	15130.480(05)	$2.63\pm0.58\times10^{17}$	7.12×10^{17}	2.71
$1\nu_1+6\nu_2^2\leftarrow 0$	^{t}R(1,0)^{o}	15450.112(05)	$2.74\pm0.37\times10^{17}$	2.79×10^{17}	0.99
≥ 6	^{x}R(1,0)^{o}	15643.052(05)	$4.02\pm0.55\times10^{17}$	3.65×10^{17}	0.91
≥ 6	^{x}Q(1,1)	15716.813(05)	$5.80\pm1.86\times10^{17}$	1.40×10^{18}	2.41
≥ 6	^{x}R(1,0)^{o}	16506.139(05)	$4.67\pm1.81\times10^{17}$	5.31×10^{17}	1.14
$9\nu_2^1\leftarrow 0^{a}$	^{x}P(1,1)	16660.240(05)^{h}	$1.37\pm0.69\times10^{17}$	4.90×10^{18}	27.07
reference: $3\nu_2^1\leftarrow 0$ R(1,1) 7144.235 cm^{-1} $B_{lu,\text{TEN96}}=5.60\times10^{20}$ ($cm^3J^{-1}s^{-2}$) [29]					

^{o} transition starting from lowest ortho $(J,G)=(1,0)$ state.
^{h} upper level is a horseshoe state.

8.3. Discussion

The results from Tab. 8.2 are graphically represented in Fig. 8.3. Theoretical Ein-

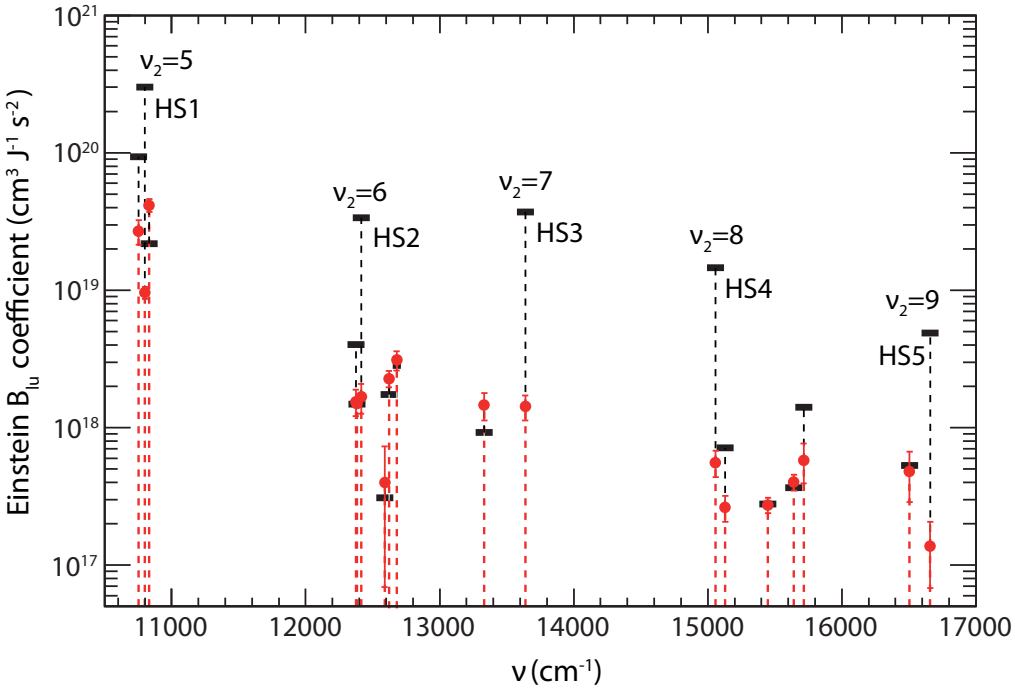

Figure 8.3. – The measured Einstein $B_{lu,m}$ coefficients and their related predicted values. Calculated Einstein $B_{lu,Ten96}$ coefficients at calculated transition frequencies ν_t are denoted by black bars. The measured Einstein $B_{lu,m}$ coefficients at measured transition frequencies ν_m are indicated in red filled circles with according error bars. The vibrational quantum number for the 5 horseshoe transitions (HS1..HS5) is given.

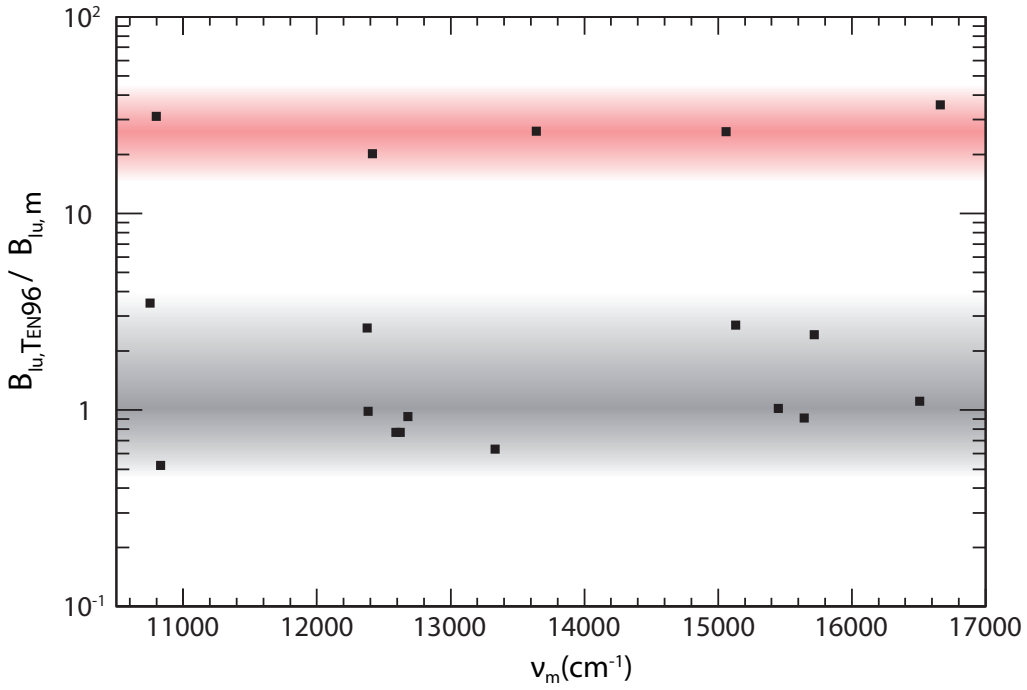

Figure 8.4. – Ratio $B_{lu,\text{TEN96}}$ divided by $B_{lu,m}$

stein $B_{lu,\text{TEN96}}$ coefficients are indicated by black bars. The experimentally derived values including their error bars are depicted in red. The general trend of decreasing transition intensity with increasing transition frequency can be observed for the experimental as well as the theoretical values. Six measured transition intensities agree within the error bars with theoretical predictions. Two more measured transition intensities lie pretty close to the calculated values. Clearly, the Einstein B_{lu} coefficients for five transitions deviate strongly from the theoretical ones. The ratio $B_{lu,\text{TEN96}}$ divided by $B_{lu,m}$ is shown in Fig. 8.4. Obviously, the five measured lines deviating the most are missing an order of magnitude in intensity compared to theoretical predictions. These five lines are the horseshoe transitions, connecting the vibrational ground state with the horseshoe states as upper level. The Einstein B_{lu} coefficients for transitions with a final energy level in the bulk are either in good agreement or show minor deviations.

The measured low transition probability for the horseshoe transitions is surprising. The level of agreement between experiment and theory when considering the frequency or the intensity of the bulk states, suggests that the PES and its eigenvalues and functions are fairly good. Theoretical calculations, over decades, using various

PES and/or different algorithms, consistently predict high transition probabilities for the transitions involving horseshoe states [60, 88, 90, 62, 72]. The experimental non-confirmation of these states requires further theoretical investigations. Although the horseshoe states are predicted to exist for J=0, one might speculate whether, in comparison to the Carrington measurement near dissociation where an intensity modulation has been seen and attributed to the horseshoe states, the absence of a rotational barrier can be connected with the low transition intensity.

On the experimental side, issues such as saturation and possible wrong assumptions must be considered. During a trap operation period, both bulk states and at least one horseshoe state are always measured. Repeated measurements of the same transitions in different trap operation periods give the same results. The non-observation of high intensities may point to saturation effects. This is however not the case, as the observation of the high-intensity lower-overtone bulk state transitions confirms that higher intensities can be measured. These lower overtones are still stronger than all higher-overtone transitions to horseshoe states.

An assumption made for the ArH^+ formation process (see Eq. 5.1) is that the reaction rate is independent of the specific excitation of the H_3^+ ion. So far none of the measurements presented here, nor any previous experiments give any indication that this could be the case. Actually, the good agreement between experiment and theoretical intensity predictions for transitions to bulk states having about the same amount of internal excitation as nearby horseshoe states over the whole measured energy range from $10752 - 16660\,\mathrm{cm}^{-1}$ is an indication that the formation rate is independent on the amount of excitation of the H_3^+ ion. In App. E the collision ($10^{-1}\,\mathrm{ms}$) and decay times ($10^0 - 10^1\,\mathrm{ms}$) are given. The ArH^+ formation predominantly occurs with the specific laser-excited H_3^+ state and only to a minor extent with subsequent radiatively decayed states. The effective lifetime before the laser-excited H_3^+ ion decays to an energy level below the Ar reaction barrier is expected to be long enough in all cases, so that each laser-excited H_3^+ ion finally leads to an ArH^+ ion. The absence of a trend in the intensity deviation with increasing number of vibrational quanta also points against an excited state dependence.

Recent theoretical studies using global PES with correct long-range behavior at dissociation, associated with a proton polarizing an H_2 molecule, demonstrate that for high energies at dissociation the horseshoe states are less pronounced. Instead, a new type of state, the asymptotic vibrational state, is introduced and related to

the regular structure of the Carrington dissociation spectrum (shortly mentioned in Sec. 2.4) [62, 72]. However, at low up to $\frac{2}{3}$ of the dissociation energy the authors do report the expected bright horseshoe states.

9. Conclusion and Outlook

In this thesis, successful advances in H_3^+ spectroscopy are demonstrated. Where classical absorption spectroscopy breaks down, the highly-sensitive method of chemical reaction spectroscopy in a cryogenic ion trap allows for ongoing investigation of the visible spectral region. Energy levels that lie more than one and a half times higher than the barrier to linearity, about half the way to dissociation, have been reported. This involved for the first time rovibrational states with 9 vibrational quanta, 3 more than previously reported. The presented energy levels are presently, and will be in the future, used to empirically correct predicted energies as done by Alijah [6]. The new predictions will directly help experimentalists in the ongoing exploration of the complete H_3^+ spectrum. Even more important, these experimentally determined energy levels are used to develop high-accuracy *ab initio* calculations beyond the Born-Oppenheimer approximation suitable to also handle non-adiabatic effects. Recent publications of a high-accuracy *ab initio* PES of H_3^+ acclaim the good agreement in the NIR region [122, 123]. The quality of these new calculations in the VIS region still needs to be verified. So far, the presented results show that the accuracy of here treated theoretical calculations [88, 36, 6] are still far from reaching spectroscopic accuracy for states reaching half the way to dissociation.

Also of major importance, first experimental determined Einstein B_{lu} coefficients for H_3^+ transitions from cold lower levels to final levels above the barrier to linearity were reported. Deviations from theory stay within one order of magnitude for most measured transitions. Interestingly, however, the high intensity predicted for the transitions connecting the vibrational ground state with horseshoe states could not be confirmed for all 5 measured transitions of this kind. This unexpected experimental result is now a challenge for theory and experiment to investigate. The traditional fruitful interplay between theoreticians and experimentalists enlighting the simplest polyatomic molecule H_3^+ is continued.

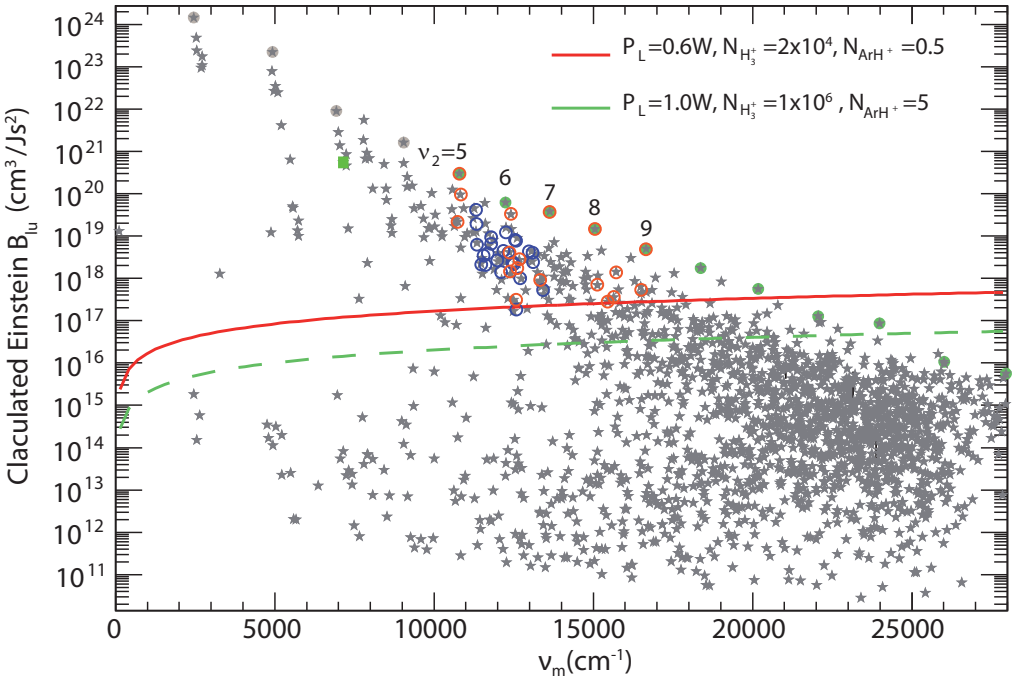

Figure 9.1. – Sensitivity estimation: Einstein B_{lu} coefficients from Ref. [88] vs. transition frequency. All transitions starting from the vibrational ground state (J=1,G=0,1) are indicated by grey stars. The red solid line shows the current expected sensitivity of our setup. The green dashed line shows the expected sensitivity after further improvements on the setup. The green square indicates the reference line for absolute normalization. Orange open circles mark the measured transitions for that also Einstein B_{lu} coefficients have been derived and open blue circles indicate the measured non-normalized transitions. All measured transitions are denoted at their measured frequency but with calculated Einstein B_{lu} coefficients.

The chemical reaction spectroscopy has not reached its sensitivity limit yet. With the current sensitivity, we expect to be able to advance up to 18000 cm^{-1} (see red line Fig. 9.1). To approach the dissociation limit further, additional sensitivity improvements have to and can be applied. A major enhancement of the sensitivity can be attained by increasing the amount of H_3^+ ions and the ArH^+ lifetime whilst suppressing the non-laser induced ArH^+. The H_3^+ ion number can be increased to the maximum storage capacity of the trap of 10^6 ions, avoiding saturation effects by modifying the ion extraction scheme further. The option of replacing the existent PMT with a fast microchannel plate detector is being investigated to avoid any possible background created by the laser photons. A pulsed valve, presently being tested, can be applied to dose the Ar gas into the trap after the H_3^+ ions are cool,

preventing the initially excited H_3^+ from reacting with the Ar and creating non-laser induced ArH^+. The initial H_3^+ excitation and thereby the H_2 pressure in the source is thus not restricted anymore. This allows for the ArH^+ lifetime to be increased by lowering the H_2 trap pressure and gain maximum signal height once laser induced ArH^+ is produced. The expected sensitivity after these improvements is illustrated by the green dashed line in Fig. 9.1 paving the way to above $20000\,cm^{-1}$.

Ne or He can be used as reactant gas instead of Ar when probing energy levels above $20000\,cm^{-1}$ (see Fig. 5.1). The activation energies for H_3^+ reacting with Ne or He require at least 10 vibrational quanta of internal excitation in the H_3^+ ion. The initial H_3^+ excitation produced by the ion source is not expected to provide this amount of energy and a nearly background-free measurement is to be expected even without pulsed valve.

The modifications are not only of importance for the investigation of the visible to ultra-violet rovibrational spectrum of H_3^+. They will also help advance the study on the ortho-to-para ratio of H_3^+ in space along with the ortho/para reaction rates in space. The implementation of a pulsed valve also opens up the way to a controlled investigation of the ortho/para-H_3^+ + ortho/para-H_2 scrambling [112, 124]. As the reactant gas Ar can be dosed after cooling of the H_3^+ ions into the 22-pole trap, no nuclear spin conversions due to the initial chemical reactions with Ar (see Eq. 5.1) are expected to occur. In combination with the differential pumping section, a variable number (even less than one on average) of collisions between H_3^+ +H_2 can be chosen and the resulting ortho-to-para ratio can be measured.

The dissociative recombination (DR) of H_3^+ is the dominant destruction mechanism in interstellar clouds. Investigations on the ortho/para dependence of the reactions are carried out [114]. For dissociative recombination experiments (mentioned in Sec. 2.3), probing of the rotational state population is of particular interest [125, 126]. The populations produced by ion sources, that are characterized in separate experiments, are reported to be modified during storage in the ring [114, 51]. State selective photodissociation would allow for in-situ determination of the rotational population. As no direct photodissociation from the lowest rotational levels is possible (see Ref. 125, 126) intermediate known energy levels are needed to perform a resonant multi-colour photodissociation (REMPD). These intermediate states can be determined from the high energy spectroscopy experiments.

For a better overall understanding on polyatomic molecules, measurements of the

H_3^+ isotopologues are of great interest. Recently a high precision line list for H_2D^+ [127] has been published. A complete set of experimental transition frequencies for H_3^+, H_2D^+, D_2H^+, and D_3^+ would allow to systematically investigate and separate pure mass- and symmetry-dependent effects.

Finally, a two-color photon absorption scheme is currently under investigation to reach excited states above $21000\,\mathrm{cm}^{-1}$. The available laser power limits the observations of transitions closer to the dissociation limit as it declines with increasing laser frequency moving into the blue region. A two-step process circumvents this issue. The here measured strong transitions can be used as first step with the second step going all the way up to dissociation.

Appendix

A. Vibrational transitions

There are 5 types of vibrational transitions that can be distinguished (see Fig. A.1). First, the fundamental band ($\nu_2 \leftarrow 0$), which has been experimentally detected by T. Oka [24]. Second, overtone bands also starting from the vibrational ground state, but addressing multiple excited levels of the ν_2 mode ($n\nu_2 \leftarrow 0$). The third type of transitions are so called hot bands, starting from vibrationally excited states ($m\nu_1 + n\nu_2 \leftarrow o\nu_1 + p\nu_2;\ m+n > o+p$). Transitions that only change the number of quanta in the ν_1 mode are called forbidden transitions, making up the fourth group ($m\nu_1 \leftarrow 0$). And last, there are transitions called combination bands, which start from the ground state to a state which is excited in both modes ($m\nu_1 + n\nu_2 \leftarrow 0$).

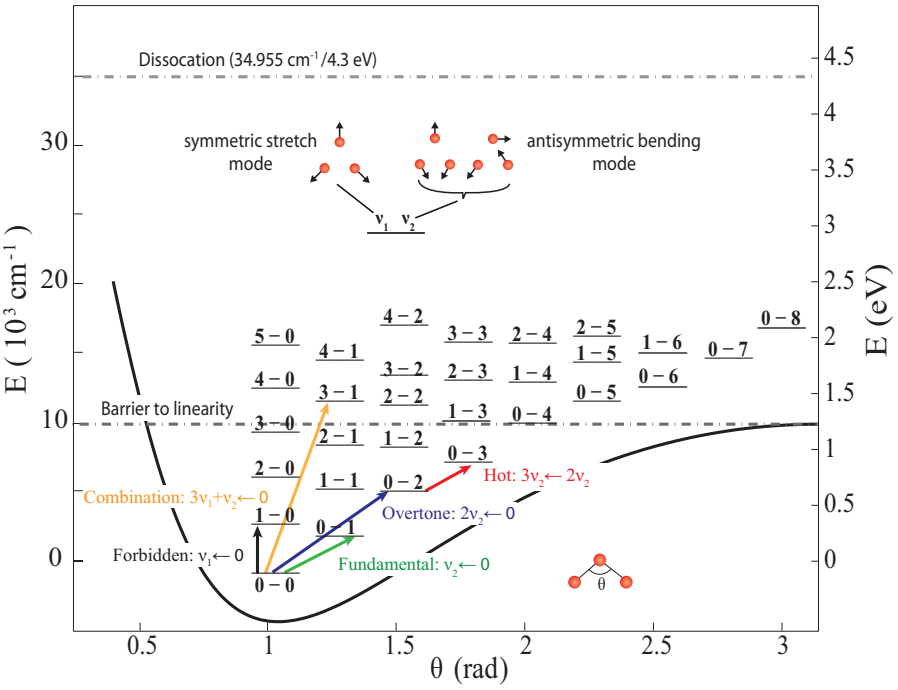

Figure A.1. – Vibrational transitions

B. Spectroscopy experiments

Selected spectroscopic studies are listed in Tab. B.1.

Year and Reference	cm^{-1}	Observed	Assignment	Method of Assignment	Technique
1980 Oka [24]	2450-2950	15 lines	$\nu_2 \leftarrow 0$	Pertubation Hamiltonian	AS in H_2 discharge
1981 Oka [128]	2450-3030	15 new lines	$\nu_2 \leftarrow 0$	Pertubation Hamiltonian	AS in H_2 discharge
1982 Carrington *et al.* [54]		First observation of IR predissociation spectra	no assignment		MS fragments
1984 Watson *et al.* [129]	2210-3030	16 new lines 30 known lines	$\nu_2 \leftarrow 0$	Pertubation Hamiltonian	AS in H_2 discharge
1984 Carrington *et al.* [55]		27 000 lines	Predissociating states near dissociation	Classical trajectory calculation	MS fragments
1987 Majewski *et al.* [130]	1800-3300	113 lines	$\nu_2 \leftarrow 0$	Pertubation Hamiltonian Supermatrix calculation	FTIR
1989 Majewski *et al.* [27]	4500-5100	49 newlines	$\nu_2 \leftarrow 0$	Pertubation Hamiltonian Variational calculation	FTIR
1990 Bawendi *et al.* [26]	2080-2950	14 new lines 70 lines 14 lines 21 lines 136 lines	$\nu_2 \leftarrow 0$ $2\nu_2(l=2) \leftarrow \nu_2$ $2\nu_2(l=0) \leftarrow \nu_2$ $\nu_1+\nu_2 \leftarrow \nu_1$ unassigned	Variational calculation Previous experiments	direct absorption spectroscopy using a newly extended tunable difference frequency spectrometer
1990 Xu *et al.* [131]	4550-6000	6 new lines 28 re-measured	$2\nu_2(l=2) \leftarrow 02$	Variational calculation Previous experiments	AS in H_2 discharge
1990 Nakanaga *et al.* [132]	2400-2800	13 re-measured	$\nu_2 \leftarrow 0$	Previous experiments	FTIR

Continued on next page

Continued from previous page

Year and Reference	cm^{-1}	Observed	Assignment	Method of Assignment	Technique
1991 Lee *et al.* [133]	6860-6900	4 new lines	$3\nu_2(l=1) \leftarrow 0$	Variational calculation	AS in H_2 discharge
1992 Xu *et al.* [28]	2400-3300	9 new lines	$\nu_1 \leftarrow 0$	Variational calculation	AS in H_2 discharge
		21 new lines	$\nu_1 + \nu_2 \leftarrow \nu_2$		
		30 new lines	$\nu_2 \leftarrow 0$		
		13 new lines	$2\nu_2(l=2) \leftarrow \nu_2$		
		89 new lines	unassigned		
2003 Gottfried *et al.* [30]	11000-12500	$\nu_1 + 4\nu_2^2$	22 new lines	Variational Calculation	AS in H_2 discharge
		$2\nu_1 + 2\nu_2^2$			
		$2\nu_1 + 3\nu_2^1$			
		$3\nu_1 + \nu_2^1$			
		$5\nu_2^1$			
		$5\nu_2^5$			
		$6\nu_2^2$			
2004 Mikosch *et al.* [101]	7193-7242	3 new lines	$3\nu_2^1 \leftarrow 0$	Variational Calculation	Chemical probing
2008 Kreckel *et al.* [32]	11300-13300	17 new lines	$3\nu_1 + 1\nu_2^1$	Variational Calculation	Chemical probing
		6 previously	$2\nu_1 + 3\nu_2^1$		
		measured	$2\nu_1 + 3\nu_2^3$		
			$2\nu_1 + 2\nu_2^2$		
			$1\nu_1 + 4\nu_2^0$		
			$1\nu_1 + 4\nu_2^2$		
			$1\nu_1 + 4\nu_2^4$		
			$5\nu_2^1$		
			$6\nu_2^2$		

Continued on next page

Continued from previous page

Year and Reference	cm^{-1}	Observed	Assignment	Method of Assignment	Technique
2009 Morong *et al.* [31]	10300-13700	121 new lines	$\nu_1 + 4\nu_2^0$ $\nu_1 + 4\nu_2^2$ $\nu_1 + 4\nu_2^4$ $2\nu_1 + 2\nu_2^2$ $2\nu_1 + 3\nu_2^1$ $2\nu_1 + 2\nu_2^0$ $3\nu_1 + \nu_2^1$ ν_2^4 $4\nu_2^4$ $5\nu_2^1$ $5\nu_2^3$ $5\nu_2^5$ $6\nu_2^2$	Variational Calculation	AS in H_2 discharge

Table B.1. – H_3^+ spectroscopy experiments

C. Theoretical studies

Selected theoretical studies on H_3^+.

Year	Authors	Title/Comment	Reference
1919	N. Bohr	Triatomic hydrogen molecule - first theoretical paper mentioning H_3	Nobelinst. Meddel. **5**(No. 28), 1 (1919)
1931	H. S. W. Massey	Triatomic hydrogen ion, H_3^+ -pertubation method finds H_3^+ to be unstable	Proc. Cambridge Phil. Soc. **27**, 451 (1931)
1935	C. A. Coulson	The electronic structure of H_3^+ - used molecular orbital theory to correctly predict the equilibrium structure of H_3^+ to be an equilateral triangle with a bond length of 0.85 A	Proc. Cambridge Philos. Soc. **31**, 244 (1935)
1936	J. Hirschfelder, H. Eyring, and N. Rosen	II. Calculation of Energy of H_3^+ Ion - potential energies of symmetrical linear H_3^+	J. Chem. Phys. **4**(2), 130 (1936)
1937	J. Hirschfelder, H. Diamond, and H. Eyring	Calculation of the energy of H_3 and of H_3^+. III	J. Chem. Phys. **5**(9), 695 (1937)
1937	D. Stevenson and J. Hirschfelder	The Structure of H_3, H_3^+, and of H_3^-. IV - calculated force constant for bending linear H_3^+	J. Chem. Phys. **5**(12), 933 (1937)
1938	J. Hirschfelder	The Energy of the Triatomic Hydrogen Molecule and Ion, V. - concluded triangular H_3^+ has the lowest energy	J. Chem. Phys. **6**(12), 795 (1938)

Continued on next page

Continued from previous page

Year	Authors	Title/Comment	Reference
1948	R. G. Pearson	Energy of H_3^+ and H_3 by the Method of Molecular Orbitals	J. Chem. Phys. **16**(5), 502 (1948)
1950	J. M. Walsh, R. A. Moore, and F. A. Matsen	Molecular Orbitals for H_3^+	J. Chem. Phys. **18**(8), 1070 (1950)
1954	R. S. Barker and H. Eyring	Approxiamte Integral Evaluations Used in the Molecular Qauntum Mechanics of Nonlinear Molecules - exact and approximate intergals for H_3^+ calculations compared	J. Chem. Phys. **22**(12), 2072 (1954)
1955	R. S. Barker, J. C. Giddings, and H. Eyring	Energy Calculations for the Linear H_3^+ Ion System	J. Chem. Phys. **23**(2), 344 (1955)
1957	G. S. Handler and J. R. Arnold	Use of Polar Coordinates for Molecules Wave Functions -quoted Eyring as referring to H_3^+ as "the scandal of modern chemistry“	J. Chem. Phys. **27**(1), 144 (1957)
1963	F. O. Ellison, N. T. Huff, and J. C. Patel	A Method of Diatomics in Molecules II. H and H_3^+ - DIM method applied to H_3^+	J. Am. Chem. Soc. **85**(22), 3544
1964	H. Conroy	Potential Energy Surfaces for the H_3^+ Molecule-Ion - calculated a rudimentary PES for H_3^+	J. Chem. Phys. **40**(2), 603 (1964)
1964	R. E. Christoffersen	Configuration-interaction study of ground state of H_3^+ molecule - most stable nuclear geometry of H_3^+ found to an equilateral triangle	J. Chem. Phys. **41**(4), 960 (1964)
1964	H. Conroy	Molecular Schrödinger Equation. IV. Results for One- and Two-Electron Systems - CI calculations on linear and triangular H_3^+	J. Chem. Phys. **41**(5), 1341 (1964)
1964	J. R. Hoyland	Two-Center Wavefunctions for ABH_n Systems. Illustrative Calculations on H_3^+ and H_3	J. Chem. Phys. **41**(5), 1370 (1964)

Continued on next page

Continued from previous page

Year	Authors	Title/Comment	Reference
1964	H. Conroy	Erratum: Potential Energy Surfaces for the H_3^+ Molecule-Ion	J. Chem. Phys. **40**(10), 3121 (1964)
1966	B. D. Joshi	Study of the H_3^+ molecule Using Self-Consistent-Field One-Center Expressions Approximation	J. Chem. Phys. **44**(9), 3627 (1966)
1967	W.-Kutzelnigg, R. Ahlrichs, I. Labib-Iskander, and W. A. Bingel	The Hartree-fock and the correlation energies of the H_3^+ ion and their dependence on the nuclear configuration	Chem. Phys. Lett. **1**(10), 477 (1967)
1967	G. V. Pfeiffer, N. T. Huff, E. M. Greenawalt, and F. O. Ellison	Method of diatomics in molecules. IV. Ground and excited states of H_3^+, H_4^+, H_5^+ and H_6^+	J. Chem. Phys. **46**(2), 821 (1967)
1967	J. P. Considine and E. F. Hayes	Single-Center Wavefunctions for H_3^+ and H_3	J. Chem. Phys. **46**(3), 1119 (1967)
1967	F. Grein and M. H. Hawton	Molecular One-Center Two-Electron Integrals Containing a Function of the Interelectronic Distance - applied to ground and lowest excited state of H_3^+	J. Chem. Phys. **46**(10), 4121 (1967)
1967	M. E. Schwartz and L. J. Schaad	An initio Studies of Small Molecules Using 1s Gaussian Basis Functions. II H_3^+	J. Chem. Phys. **47**(12), 5325 (1967)
1968	A. J. A. Wu and F. O. Ellison	Method of Diatomics-in-Molecules. VII. Excited Singlet States of H_3^+ - applied DIM method to singlet H_3^+, calculated potential energy surfaces for all states	J. Chem. Phys. **48**(4), 1491 (1968)
1968	R. E. Christofferson and H. Shull	Nature of the two-electron chemical bond. VII. Multicenter bonds and H_3^+ - found that H_3^+ clossely resembles its united-atom analog Li^+	J. Chem. Phys. **48**(4), 1790 (1968)

Continued on next page

Continued from previous page

Year	Authors	Title/Comment	Reference
1968	K. E. Banyard and A. D. Tait	Quantum-Mechanical Study of Some Three-Center Two-Electron Systems. II. A Natural-Orbital, Electron-Population, and Energy Analysis	J. Chem. Phys. **49**(7), 3050 (1968)
1968	A.-j. A. Wu and F. O. Ellison	Method of diatomics-in-molecules. VIII. Excited triplet states of H_3^+ - applied DIM method to triplet H_3^+, calculated potential energy surfaces	J. Chem. Phys. **48**(11), 5032 (1968)
1968	F. Grein and T. C. Chang	Correlated one-center wavefunctions for two-electron molecules. III. Correlated self-consitent field functions and applications to H_3^+	Theor. Chim. Acta **12**(3), 243 (1968)
1969	R. D. Poshusta, J. A. Haugen, and D. F. Zetik	Ab Initio Predictions for Very Small Ions - predicts H_3^+ to be stable	J. Chem. Phys. **51**(8), 3343 (1969)
1969	H. Conroy	Molecular Schrödinger Equation. X. Potential Surfaces for Ground and Excited States of Isosceles H_3^{2+} and H_3^+ - calculated PES for the ground and excited states	J. Chem. Phys. **51**(9), 3979 (1969)
1970	R. L. Somorjai and C. P. Yue	Integral transform Gaussian wave function for H_3^{2+} and H_3^+	J. Chem. Phys. **53**(5), 1657 (1970)
1970	R. F. Borkman	Single-center configuration-interaction calculations on the ground state of H_3^+	J. Chem. Phys. **53**(8), 3153 (1970)
1970	I. G. Csizmadia, R. E. Kari, J. C. Polanyi, A. C. Roach, *et al.*	Ab initio SCFMOCI Calculations for H^-, H_2, and H_3^+ Using Gaussian Basis Sets - computed exact SCF PES for reaction $H^+ + H_2$	J. Chem. Phys. **52**(12), 6205 (1970)
1970	T. C. Chang and F. Grein	Correlated one-center wavefunctions for two-electron molecules. IV. Integrals for a cutoff correlation factor. Application to H_3^+	Theor. Chim. Acta **17**(5), 371 (1970)

Continued on next page

Continued from previous page

Year	Authors	Title/Comment	Reference
1971	R. F. Borkman	Electronic quadrupole moments for H_2^+, H_2 and H_3^+ from point charge model	Chem. Phys. Lett. **9**(6), 624 (1971)
1971	A. J. Duben and J. P. Lowe	Correlation Studies on H_3^+. I. The Wavefunctions	J. Chem. Phys. **55**(9), 4270 (1971)
1971	A. J. Duben and J. P. Lowe	Correlation Studies on H_3^+. II. Electron Densities and Expectation Values	J. Chem. Phys. **55**(9), 4276 (1971)
1971	R. K. Preston and J. C. Tully	Effects of Surface Crossing in Chemical Reactions: The H_3^+ System - semiempirical DIM PES (qualitatively correct)	J. Chem. Phys. **54**(10), 4297 (1971)
1971	K. Kawaoka and R. F. Borkman	Electric, Magnetic, and Spectral Properties of H_3^+ Ground State Calculated from Single-Center Wavefunctions - concluded that it was unlikely to achieve sufficient concentration of H_3^+ to be observable	J. Chem. Phys. **55**(9), 4637 (1971)
1971	J.-T. J. Huang	Simple Diatomics-in-Molecules Energy Expression for M_3^+ and Its Application to H_3^+	J. Chem. Phys. **55**(10), 5136 (1971)
1972	R. W. Patch	On the Observability of the H_3^+ Fundamental Spectrum - predicted that H_3^+ would be difficult to observe in the laboratory but may be observable in spectra of stars or planets	J. Chem. Phys. **57**(6), 2594 (1972)
1972	J.-T. J. Huang	Analytical Self-Consistent-Field Energy Expression for Ground-State H_3^+ Ion - approximate SCF PES	J. Chem. Phys. **56**(6), 3176 (1972)
1973	C. W. Bauschlicher, Jr., S. V. O'Neil, R. K. Preston, H. F. Schaefer III, *et al.*	Avoided intersection of potential energy surfaces: The ($H^+ + H_2$, $H + H_2$) system -nonempirical electronic structure calculations on the two lowest $^1A_1$ states of H_3^+	J. Chem. Phys. **59**(3), 1286 (1972)

Continued on next page

Continued from previous page

Year	Authors	Title/Comment	Reference
1973	L. Salmon and R. D. Poshusta	Correlated Gaussian wavefunctions for H_3^+ -calculated vibrational frequencies as $\nu_1 = 3272\,\mathrm{cm}^{-1}$ and $\nu_2 = \mathrm{cm}^{-1}$	J. Chem. Phys. **59**(7), 3497 (1973)
1973	N. C. Handy	Correlated Gaussian wavefunctions - present variationally optimized correlated wavefunctions for H_3^+	Mol. Phys. **26**(1), 169 (1973)
1974	L. J. Schaad and W. V. Hicks	Gaussian basis configuration interaction calculations on twenty electronic states of H_3^+. - calculated a stable triplet state	J. Chem. Phys. **61**(5), 1934 (1974)
1974	G. D. Carney and R. N. Porter	H_3^+ geometry dependence of electronic properties - first accurate *ab initio* potential energy surface, CI using generalized Morse functions	J. Chem. Phys. **60**(11), 4251 (1974)
1974	C. F. Giese and W. R. Gentry	Classical trajectory treatment of inelastic scattering in collisions of H^+ with H_2, HD, and D_2 - analytical fit to the CI energies of Csizmandia *et al.* (1970)	Phys. Rev. A **10**(6), 2156 (1974)
1975	J. B. Anderson	A random-walk simulation of the Schrödinger Equation	J. Chem. Phys. **63**(4), 1499 (1975)
1976	G. D. Carney and R. N. Porter	H_3^+-*ab initio* calculation of the vibration spectrum - first calculated rovibrational energies of H_3^+	J. Chem. Phys. **65**(9), 3547 (1976)
1977	G. D. Carney and R. N. Porter	The lowest rotation states of H_3^+ and symmetry considerations in dissociative e^- capture	J. Chem. Phys. **66**(6), 2756 (1977)
1977	R. Ahlrichs, C. Votava, and C. Zirz	Comment: The bound $^3\Sigma_u^+$ excited level of H_3^+	J. Chem. Phys. **66**(6), 2771 (1977)
1977	C. S. Warke and A. K. Dutta	Variational approach to the calculation of the structure and properties of H_3^+ ions in strong magnetic fields	Phys. Rev. A **16**(5), 1747 (1977)

Continued on next page

Continued from previous page

Year	Authors	Title/Comment	Reference
1978	R. D. Bardo and M. Wolfsberg	The adiabatic correction for non-linear triatomic molecules: Techniques and calculations - used a SCF wavefunctions to estimate the adiabatic correction for H_3^+	J. Chem. Phys. **68**(6), 2686 (1978)
1978	C. E. Dykstra, A. S. Gaylord, W. D. Gwinn, W. C. Swope, *et al.*	The uncoupled symmetric streching frequency of H_3^+ - *ab initio* PES calculated using method of self-consistent electron pairs	J. Chem. Phys. **68**(8), 3951 (1978)
1979	C. E. Dykstra and W. C. Swope	The H_3^+ potential surface - potential surface calculated using full configuration expansion with a basis set of 68 contracted Gaussian functions	J. Chem. Phys. **70**(1), 1 (1979)
1980	R. Schinke, M. Dupuis, and W. A. Lester Jr.	Proton-H_2 scattering on an *ab initio* CI potential energy surface. I. Vibrational excitation at 10 eV - full CI surface appropriate for scattering calculations and spectroscopy	J. Chem. Phys. **72**(7), 3909 (1980)
1980	G. D. Carney	Refinements in the vibration frequencies of trihydrogen(1+) and trideuterium(1+) - refined fundamental frequencies and determined Einstein A coefficients	Mol. Phys. **39**(4), 923 (1980)
1980	G. D. Carney and R. N. Porter	*Ab initio* prediction of the rotation-vibration spectrum of H_3^+ and D_3^+ - calculated several lines of the observed fundamental with an accuracy better than 1%	Phys. Rev. Lett. **44**(7), 537 (1980)
1981	J. D. Doll	Monte Carlo based electronic structure techniques: analysis and applications - examined Monte Carlo based variational electronic structure techniques, illustrated with H_3^+	Chem. Phys. Lett. **81**(2), 335 (1981)

Continued on next page

Continued from previous page

Year	Authors	Title/Comment	Reference
1981	F. Mentch and J. B. Andreson	Quantum chemistry by random walk: importance sampling for triatomic hydrogen(+) - numerical uncertainty of $50\,cm^{-1}$ makes this method not well suited for rovibrational calculations	J. Chem. Phys. **74**(11), 6307 (1981)
1982	A. Preiskorn and W. Woznicki	Superposition of correlated configurations method. The ground state of H_3^+ - variational calculations using correlated wave functions	Chem. Phys. Lett. **86**(4), 369 (1982)
1983	O. S. Van Roosmalen, F. Iachello, R. D. Levine, and A. E. L. Dieperink	Algebraic approach to molecular rotation-vibration spectra. II. Triatomic molecules - application to H_3^+ considered	J. Chem. Phys. **79**(6), 2515 (1983)
1984	M. R. Aliev and V. M. Mikhailov	Forbidden rotational and vibrational-rotational transitions in triatomic hydrogen(1+) ion - dipole moments and line strength formulas for forbidden rotational transitions	Acta Physica Hungarica **55**(1-4), 293 (1984)
1984	P. G. Burton, E. Von Nagy-Felsobuki, G. Doherty, and M. Hamilton	Vibration spectrum of triatomic hydrogen ion (H_3^+): a model hamiltonian - variational calculations using a slightly modified Watson model Hamiltonian and a new *ab initio* PES	Chem. Phys. **83**(1-2), 83 (1984)
1984	P. G. Burton, E. Von Nagy-Felsobuki, and G. Doherty	The vibration spectrum of triatomic hydrogen (1+) and triatomic deuterium (1+). Three-dimensional basis selection and convergence of the low-lying vibrational CI wavefunctions	Chem. Phys. **104**(2), 323 (1984)

Continued on next page

Continued from previous page

Year	Authors	Title/Comment	Reference
1984	J. K. G. Watson	Higher-Order Vibration-Rotation Energies of the X_3 Molecule - higher-order pertubations calculations, discussion of quantum numbers and selection rules	J. Mol. Spectrosc. **103**(2), 350 (1984)
1984	J. Tennyson and B. T. Sutcliffe	On the rovibrational levels of the H_3^+ and H_2D^+ molecules - variationally exact rovibrational levels for H_3^+	Mol. Phys. **51**(4), 887 (1984)
1984	A. Preiskorn and W. Woznicki	Variational calculations for the ground state of triatomic hydrogen ion (H_3^+) - additional calculations based on superposition of correlated configurations method	Mol. Phys. **52**(6), 1291 (1984)
1985	B. Martire and P. G. Burton	The vibrational spectra of H_3^+ and D_3^+: Improved values from new representations of *ab initio* surfaces - comparison of several PES	Chem. Phys. Lett. **121**(6), 479 (1985)
1985	V. Špirko, P. Jensen, P. R. Bunker, and A. Cejchan	The development of a new Morse-oscillator based rotation-vibration Hamiltonian for H_3^+ - analytical fit to published *ab initio* PES using a symmetry-adapted Morse-oscillator basis set	J. Mol. Spectrosc. **112**(1), 183 (1985)
1985	P. G. Burton, E. Von Nagy-Felsobuki, G. Doherty, and M. Hamilton	The vibration spectrm of triatomic hydrogen(1+). A PNO-CI *ab initio* potential energy surface and its analytical representation - reexamined their PES, calculated band origins	Mol. Phys. **55**(3), 527 (1985)
1985	J. Tennyson and B. T. Sutcliffe	A calculation of the rovibrational spectra of the H_3^+, H_2D^+ and D_2H^+ molecules - variational calculations using the Burton potential energy data	Mol. Phys. **56**(5), 1175 (1985)

Continued on next page

Continued from previous page

Year	Authors	Title/Comment	Reference
1986	F. S. Pan and T. Oka	Calculated forbidden rotational spectra of the hydrogen ion (H_3^+)	Astrophys. J. **305**(1), 518 (1986)
1986	W. Meyer, P. Botschwina, and P. Burton	Ab initio calculations of near-equilibrium potential and multipole moment surfaces and vibrational frequencies of H_3^+ and its isotopomers - various full CI *ab initio* PES using Morse-type coordinate	J. Chem. Phys. **84**(2), 891 (1986)
1986	P. Jensen and V. Špirko	A new Morse-ocillator based Hamiltonian for H_3^+: Calculation of line strengths - method for calculating rovibrational line strengths of H_3^+	J. Mol. Spectrosc. **118**(1), 208 (1986)
1987	I. Hamilton	Vibrational spacings for triatomic hydrogen ion(1+)	J. Chem. Phys. **87**(1), 774 (1987)
1987	B. R. Johnson	Semicalssical vibrational eigenvalues of hydrogen, deuterium, and tritium triatomic ions(1+)(H_3^+, D_3^+, and T_3^+)by the adiabatic switching method - first application of hyperspherical coordinates to H_3^+	J. Chem. Phys. **86**(3), 1445 (1987)
1987	J. B. Anderson	Simplified samoling in quantum Monte Carlo: application to hydrogen triatomic ion(1+)	J. Chem. Phys. **86**(5), 2839 (1987)
1987	S. Miller and J. Tennyson	1st Principles Calculation of the Molecular Constants of H_3^+, H_2D^+, D_2H^+, and D_3^+ - demonstrated the power of the variational approach using MBB surface	J. Mol. Spectrosc. **126**(1), 183 (1987)
1987	V. Špirko, A. Cejchan, and P. Jensen	A new Morse-oscillator based Hamiltonian for H_3^+: Explicit expressions for some vibrational matrix elements	J. Mol. Spectrosc. **124**(2), 430 (1987)
1988	S. Miller and J. Tennyson	Calculated rotational and rovibrational transitions in the spectrum of hydrogen triatomic ion(1+) - used variational approach to calculated transitions to spectroscopic accuracy	Astrophys. J. **335**(1, Pt. 1), 486 (1988)

Continued on next page

Continued from previous page

Year	Authors	Title/Comment	Reference
1988	J. Oddershede and J. R. Sabin	Calculation of Rotational g-factors and Magnetic Succesptibilities of H_3^+ - the components of the g tensor can be used to estimate the rotation-dependent terms of the nonadiabatic corrections	Chem. Phys. **112**(2), 291 (1988)
1988	C. Urdaneta, A. Largo-Cabrerizo, J. Lievin, G. G. Lie, *et al.*	Gaussian functions in Hylleraas-CI calculations. I. Ground state energies for molecular hydrogen, hydrohelium(1+)(HeH^+), and hydrogen triatomic ion(1+) - Hylleraas CI approach using a Cartesian Gaussian basis	J. Chem. Phys. **88**(3), 2091 (1988)
1988	D. Talbi and R. P. Saxon	Theoretical study of excited singlet states of hydrogen triatomic monopositive ion: potential surfaces and transition moments	J. Chem. Phys. **89**(4), 2235 (1988)
1988	R. M. Whitnell and J. C. Light	Symmetry-adapted discrete variable representations	J. Chem. Phys. **89**(6), 3674 (1988)
1988	S. Miller and J. Tennyson	Overtone Bands of H_3^+ − 1st Principle Calculations	J. Mol. Spectrosc. **128**(2), 530 (1988)
1989	J. J. Soares Neto, S. B. Padkjaer, and J. Linderberg	Hyperspherical coordinates in the study of rovibrational levels of the hydrogen triatomic monopositive ion and its isotopomers - variational calculation using hyperspherical coordinates	Int. J. Quant. Chem. **23**, 120 (1989)
1980	R. M. Whitnell and J. C. Light	Efficient Pointwise Representations For Vibrational Wace-Functions − Eigenfunctions of H_3^+ - application of full symmetry adapted DVR to H_3^+ using hyperspherical coordinates and the MBB surface	J. Chem. Phys. **90**(3), 1774 (1989)
1989	P. E. S. Wormer and F. de Groot	The potential energy surface of triplet H_3^+: A representation in hyperspherical coordinates - full CI calculation of the triplet PES using hyperspherical coordinates	J. Chem. Phys. **90**(4), 2344 (1989)

Continued on next page

Continued from previous page

Year	Authors	Title/Comment	Reference
1989	J. Tennyson and J. R. Henderson	Highly excited rovibrational states using a discrete variable representation: The H_3^+ molecular ion - formulation of the rovibrational problem in Jacobi coordinates using DVR	J. Chem. Phys. **91**(7), 3815 (1989)
1989	S. Miller and J. Tennyson	Hot Band Transition Frequencies and Line Strengths in H_3^+ – 1st Principle Calculation	J. Mol. Spectrosc. **136**(2), 223 (1989)
1990	J. R. Henderson and J. Tennyson	All the vibrational bound states of H_3^+ - vibrational calculations for three PES using DVR, all J=0 bound states converged to within $10\,cm^{-1}$	Chem. Phys. Lett. **173**(2-3), 133 (1990)
1990	O. Brass, J. Tennyson, and E. Pollak	Spectroscopy and dynamics of the highly excited nonrotating three-dimensional hydrogen triatomic monopositive ion - wave functions for the MBB surface and a DIM surface	J. Chem. Phys. **92**(6), 3377 (1990)
1990	D. Frye, A. Preiskorn, G. C. Lie, and E. Clementi	Gaussian functions in Hylleraas-configuration interaction calculations. V. An accurate ab initio hydrogen triatomic monopositive ion potential-energy surface	J. Chem. Phys. **92**(8), 4948 (1990)
1990	S. Carter and W. Meyer	A variational method for the calculation of vibrational energy levels of triatomic molecules using Hamiltonian in hyperspherical coordinates - new variational procedure using hyperspherical coordinates applied to H_3^+	J. Chem. Phys. **93**(12), 8902 (1990)
1990	S. Miller, J. Tennyson, and B. T. Sutcliffe	Forbidden rotational and rovibrational transitions in hydrogen ion (H_3^+): first principles calculations	J. Mol. Spectrosc. **141**(1), 104 (1990)
1990	J. R. Henderson, S. Miller, and J. Tennyson	Discrete variable representations of large-amplitude rovibrational states in a generalized coordinate system	J. Chem. Soc. Farad. Trans. **86**(11), 1963 (1990)

Continued on next page

Continued from previous page

Year	Authors	Title/Comment	Reference
1990	P. Bartlett and B. J. Howard	The rotational-vibrational spectrum of symmetrical nonrigid triatomics in hyperspherical coordinates - the H_3^+ molecule - used MBB surface to calculated the first rovibrational energy levels of H_3^+ using hyperspherical coordinates (J=0)	Mol. Phys. **70**(6), 1001 (1990)
1991	Z. Bačić and J. Z. H. Zhang	A new D_{3h} symmetry-adaptedmmethod for highly excited vibrational levels of floppy triatomics: the H_3^+ molecule	Chem. Phys. Lett. **184**(5-6), 513 (1991)
1991	P. N. Day and D. G. Truhlar	The calculation of highly excited bound-state energy levels for a triatomic molecule by using three-arrangement basis sets and contracted basis functions	J. Chem. Phys. **95**(9), 6615 (1991)
1991	A. Preiskorn, D. Freye, and E. Clementi	Gaussian functions in Hylleraas-configuration-interaction calculations. VI. The first excited state of the hydrogen triatomic monopositive Ion	J. Chem. Phys. **94**(11), 7204 (1991)
1992	S. B. Padkjaer, J. J. Soares Neto, and J. Linderberg	Non-zero total angular momentum calculations of rovibrational levels for triatomic molecules using generator coordinates	Chem. Phys. **161**, 419 (1992)
1992	S. A. Alexander, R. L. Coldwell, and G. Aissing	Calculating atomic and molecular properties using variational Monte Carlo methods	Int. J. Quant. Chem. **26**, 213 (1992)
1992	S. Carter and W. Meyer	Comment on: Discrepancies between variationally calculated vibrational energies of H_3^+	J. Chem. Phys. **96**(3), 2424 (1992)
1992	J. R. Henderson, J. Tennyson, and B. T. Sutcliffe	Reply to "Comment on discrepancies between variationally calculated vibrational energies of the hydrogen triatomic monopositive ion"	J. Chem. Phys. **96**(3), 2426 (1992)
1992	J. B. Anderson	Quantum-Chemistry by Random-Walk Higher Accuracy for H_3^+	J. Chem. Phys. **96**(5), 3702 (1992)

Continued on next page

Continued from previous page

Year	Authors	Title/Comment	Reference
1992	Z. Bačić and J. Z. H. Zhang	High-lying rovibrational states of floppy X_3 triatomics by a new D_{3h} symmetry adapted method: Application to the H_3^+ molecule	J. Chem. Phys. Lett. **86**(5), 3707 (1992)
1992	G. C. Lie and D. Frye	Vibrational analysis of a Hylleraas-configuration interaction potential for H_3^+ - Hylleraas CI using Morse-Dunham coordinates	J. Chem. Phys. **96**(9), 6784 (1992)
1992	M. Berblinger, C. Schlier, J. Tennyson, and S. Miller	Accurate specific molecular state densities by phase space integration. II. Comparison with quantum calculations on H_3^+ and HD_2^+ - semi-calssical determination of the specific number and density of quantum states	J. Chem. Phys. **96**(9), 6842 (1992)
1992	B. M. Dinelli, S. Miller, and J. Tennyson	Bands of triatomic hydrogen(1+) (H_3^+) up to $4\nu_2$: rovibrational transitions from first principles calculations - band origins and Einstein A coefficients for all transitions up to $4\nu_2^4$	J. Mol. Spectrosc. **153**(1-2), 718 (1992)
1992	C. R. LeSueur, S. Miller, J. Tennyson, and B. T. Sutcliffe	On the use of variational wave functions in calculating vibrational band intensities	Mol. Phys. **76**(5), 1147 (1992)
1993	C. R. LeSueur, J. R. Henderson, and J. Tennyson	Gateway states and bath states in the vibrational spectrum of hydrogen molecular cation (H_3^+)	Chem. Phys. Lett. **206**(5-6), 429 (1993)
1993	D. A. Sadovskii, N. G. Fulton, J. R. Henderson, J. Tennyson, *et al.*	Nonlinear normal modes and local bending vibrations of hydrogen and deuterium triatomic monopositive ions (H_3^+ and D_3^+)	J. Chem. Phys. **99**(2), 906 (1993)

Continued on next page

Continued from previous page

Year	Authors	Title/Comment	Reference
1993	J. R. Henderson, J. Tennyson, and B. T. Sutcliffe	All the bound, vibrational states of the hydrogen triatomic monopositive ion: a reapraisal - computed all vibrational band origins up to $35\,000\,\mathrm{cm}^{-1}$ (converged to within $2\,\mathrm{cm}^{-1}$)	J. Chem. Phys. **98**(9), 7191 (1993)
1993	M. J. Bramley, and T. Carrington Jr.	A general discrete variable methods to calculate vibrational energy levels of three- and four-atom molecules	J. Chem. Phys. **99**(11), 8519 (1993)
1993	R. Röhse, W. Klopper, and W. Kutzelnigg	Configuration interaction calculations with terms linear in the interelectronic coordinate for the ground state of H_3^+. A benchmark study - Hylleras CI, estimated relativistic corrections	J. Chem. Phys. **99**(11), 8830 (1993)
1994	J. K. G. Watson	Vibration-Rotation Calculations for H_3^+ Using a Morse-Based Discrete Variable Representation - semi-empirical surface based on MBB potential	Can. J. Phys. **72**(9-10), 702 (1994)
1994	W. A. Majewski, A. R. W. McKellar, D. Sadovskii, and J. K. G. Watson	New observations and analysis of the infrared vibration-rotation spectrum of H_3^+ - observed 52 lines from 1800-2550 cm^{-1} and 71 lines from 2900-5000 cm^{-1} using FTIR emission, calculated lines from adjusted MBB surface	Can. J. Phys. **72**, 1016 (1994)
1994	H. Yu, A. D. Bandrauk, and V. Sonnad	Three-dimensional finite element method for electronic properties of small polyatomic molecules: H_2^+, H_2, H_3^{2+} and H_3^+	Chem. Phys. Lett. **222**(4), 387 (1994)
1994	H. Wei and T. Carrington Jr.	Discrete variable representations of complicated kinetic energy operators	J. Chem. Phys. **101**(2), 1343 (1994)

Continued on next page

Continued from previous page

Year	Authors	Title/Comment	Reference
1994	S. Carter and W. Meyer	A variational method for the calculation of rovibrational energy levels of triatomic molecules using a Hamiltonian in hyperspherical coordinates: Applications to H_3^+ and Na_3^+ - calculated rovibrational energy levels (up to J=2) of H_3^+ using the MBB surface	J. Chem. Phys. **100**(3), 2104 (1994)
1994	R. Röhse, W. Kutzelnigg, R. Jaquet, and W. Klopper	Potential energy surface of the H_3^+ ground state in the neighbourhood of the minimum with microhatree accuracy and vibrational frequencies derived from it - *ab initio* PES with microhatree accuracy (RKJK)	J. Chem. Phys. **100**(3), 2104 (1994)
1994	M. J. Bramley, J. W. Tromp, T. Carrington Jr., and G. C. Corey	Efficient calculation of highly excited vibrational energy levels of floppy molecules: the band origins of H_3^+ up to $35\,000\,cm^{-1}$	J. Chem. Phys. **100**(9), 6175 (1994)
1994	L. Wolniewicz and J. Hinze	Rotation-vibration states of H_3^+ computed using hyperspherical coordinates and harmonics - performed calculations for H_3^+ up to J=4	J. Chem. Phys. **101**(11), 9817 (1994)
1994	J. R. Alvarez-Collado	Normal coordinates-finite elements calculated of 3D vibrational energy levels: Henon-Heilers and Eckart potentials, H_3^+ molecule	J. Comput. Chem. **15**(4), 377 (1994)
1994	B. M. Dinelli, S. Miller, and J. Tennyson	A Specctroscopically Determined Potential Energy Surface for H_3^+ - adjusted parameters of the LF surface with succesive refinements using variational calculations to reproduce experimental data	J. Mol. Spectrosc. **163**(1), 71 (1994)

Continued on next page

Continued from previous page

Year	Authors	Title/Comment	Reference
1994	J. Tennyson and O. L. Polyanski	Non-Born-Oppenheimer correction to the H_3^+ potential from experimental data - demonstrated that major error in the LF potential is due to the Born-oppenheimer approximation, constructed adiabatic surface good to within $0.03\,cm^{-1}$	Phys. Rev. A **50**(1), 314 (1994)
1995	A. Alijah, J. hinze, and L. Wolniewicz	Rotation-vibrational states of H_3^+ using hyperspherical coordinates and harmonics - compared results of variational calculations using the MBB and RKJK surfaces	Ber. Bunsenges. Phys. Chem. **99**(3), 251 (1995)
1995	J. K. G. Watson	The vibration-rotation spectrum and anharmonic potential of H_3^+ - semi-empirical adjustment of the MBB surface, artificial wall	Chem. Phys. **190**, 291 (1995)
1995	J. Troe	Simplified models for anharmonic numbers and densities of vibrational states. I. Application to NO_2 and H_3^+	Chem. Phys. **190**, 381 (1995)
1995	B. M. Dinelli, C. R. LeSueur, J. Tennyson, and R. D. Amos	Ab-initio ro-vibrational levels of H_3^+ beyond the Born-Oppenheimer approximation - calculated rovibrational energy levels using mass-dependent adiabatic correction	Chem. Phys. Lett. **232**, 295 (1995)
1995	W. Cencek, J. Komasa, and J. Rychlewski	Benchmark claculations for two-electron systems using explicitly correlated Gaussian functions	Chem. Phys. Lett. **246**(4,5), 417 (1995)
1995	A. Ichihara and K. Yokoyama	Ab initio potential energy surfaces for the lowest $^1A'$ states of H_3^+	Chem. Phys. Lett. **103**(6), 2109 (1995)
1995	B. M. Dinelli, O. L. Polyanski, and J. Tennyson	Spectroscopically determined Born-Oppenheimer and adiabatic surfaces for H_3^+, H_2D^+, and D_3^+ - semi-empirical mass-dependent surface with adiabatic corrections	J. Chem. Phys. **103**(24), 10433 (1995)
1995	R. Jaquet and R. Röhse	Rovibrational energy levels and transitions fro H_3^+ computed from a new highly accurate PES	Mol. Phys. **84**(2), 291 (1995)

Continued on next page

Continued from previous page

Year	Authors	Title/Comment	Reference
1995	J. Tennyson, B. M. Dinelli, and O. L. Polyanski	On the determination of PES of spectroscopic accuracy	Theochem. **341**, 133 (1995)

D. Symmetry considerations

This appendix provides the character- and the multiplication table for the D_{3h} molecular symmetry (MS) group. For H_3^+ the MS group is isomorphic to the molecular point group and therefore the name of the MS group is that of point group followed by (M). For further details and definitions on symmetry groups see Ref. 42 and Ref. 134.

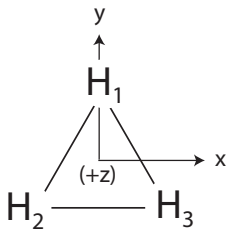

Figure D.1. – D_{3h} — H_3^+.

The triatomic hydrogen ion H_3^+ consists of three protons and therefore the nuclei obey the Fermi-Dirac statistic. The complete wave function must change its sign under the odd permutations of the nuclei (12), (23), (31) and be invariant to the even permutations (123) and (132). According to the character table D.1 the complete wave function of H_3^+ must therefore have either A_2' or A_2'' symmetry (indicated in red).

For analysis of possible combinations of the decomposited wave function the multiplication table D.2 for D_{3h} is given. The results leading to A_2' or A_2'' symmetry are indicated in red. The possible combinations of rovibronic (rve) wave functions and nuclear spin are listed in Tab. D.3. The electronic ground state of H_3^+ is totally symmetric (A_1'). Therefore, rovibrational (rv) levels with A_1' symmetry (J even, $G = 0$) are not allowed.

Table D.1. – Character table D_{3h}. For each class of the molecular symmetry group one symmetry element is given. The number of symmetry elements in the class is indicated underneath. The equivalent element of the molecular point group is also shown. The symmetry for the dipole moment operator μ_A along a space-fixed direction A is also indicated. A more detailed character table can be found in [42]

$D_{3h}(M)$:	E	(123)	(12)	E^*	$(123)^*$	$(12)^*$	
	1	2	3	1	2	3	
D_{3h}:	E	$2C_3$	$3C_2$	σ_h	$2S_3$	$3\sigma_v$	
A_1'	1	1	1	1	1	1	
A_2'	1	1	-1	1	1		
A_1''	1	1	1	-1	-1	-1	$\Gamma(\mu_A)$
A_2''	1	1	-1	-1	-1	1	
E'	2	-1	0	2	-1	0	
E''	2	-1	0	-2	1	0	

Table D.2. – Multiplication table for D_{3h}

	A_1'	A_2'	A_1''	A_2''	E'	E''
A_1'	A_1'	A_2'	A_1''	A_2''	E'	E''
A_2'		A_2'	A_2''	A_1''	E'	E''
A_1''			A_1'	A_2'	E''	E'
A_2''				A_1'	E''	E'
E'					A_1', A_2', E'	A_1'', A_2'', E''
E''						A_1', A_2', E'

Table D.3. – Spin statistical weights for H_3^+

Γ_{rve}	Γ_{rv}	Γ_{ns}	Γ_{tot}	g_{ns}
A_1'	A_1'	—	—	—
A_1''	A_1''	—	—	—
A_2'	A_2'	$4A_1'$	A_2'	4
A_2''	A_2''	$4A_1'$	A_2''	4
E'	E'	$2E'$	A_2'	2
E''	E''	$2E'$	A_2''	2

E. Time constants

The interaction between an ion with charge q and a neutral collision partner with polarizability α can be described by the Langevin theory. A short summary is given in appendix A of Ref. 109. The Langevin rate coefficient is given by

$$k_L = q\sqrt{\frac{\pi\alpha}{\epsilon_0\mu}}, \tag{E.1}$$

or in practical units (α in Å^3, μ in u) by

$$k_L = 2.342\sqrt{\frac{\alpha}{\mu}}10^{-9}\mathrm{cm^3s^{-1}}. \tag{E.2}$$

Time constants τ for collisions of the type H_3^+ + X (X =N_2, H_2, Ar, He) at typical 22-pole trap conditions (see Tab. 5.1) are given in Tab. E.1.

Table E.1. – Collision reaction rates for H_3^+ + X

X	α[a] (Å^3)	μ (u)	k_L (cm^{3}s^{-1})	N/V (cm^{-3})	rate (s^{-1})	τ (s)
N_2	1.710	2.71	1.86	$2.27{\cdot}10^{08}$	$4.22{\cdot}10^{-1}$	2.37
H_2	0.787	1.20	1.90	$1.96{\cdot}10^{09}$	3.72	$2.69{\cdot}10^{-1}$
Ar	1.664	2.79	1.81	$1.27{\cdot}10^{12}$	$2.30{\cdot}10^{+3}$	$4.35{\cdot}10^{-4}$
He	0.208	1.71	0.82	$2.68{\cdot}10^{14}$	$2.18{\cdot}10^{+5}$	$4.58{\cdot}10^{-6}$

[a] NIST Standard Reference Database Number 101 Release 15a, April2010.

Table E.2 shows for selected transitions the effective lifetime of the upper state, taking all possible radiative decay pathways of Ten96 into account. When using Ar as reactant gas, the chemical probing spectroscopy is sensitive to excited states down to 4436 cm^{-1}. Radiative decay from the upper level to states below this

Table E.2. – Timings for selected states. The number of decay paths (d.p.) is given with the corresponding effective lifetime of the upper state. The fastest single decay pathway (fastest d.) is shown as well as the number of critical decay pathways and the critical effective lifetimes. Shaded red columns indicate horseshoe (all para) transitions and light blue columns belong to ortho transitions

transition (cm^{-1})	d.p.	lifetime (ms)	fastest d. (ms)	crit. d.p.	crit. lifetime (ms)
10798.777	(18)	1.9	4.5	(3)	75.3
12413.247	(25)	1.5	5.8	(3)	516.4
13638.251	(37)	3.2	10.7	(3)	282.9
15058.680	(56)	1.9	9.1	(3)	666.3
15130.480	(114)	1.4	8.8	(7)	846.4
15450.112	(197)	1.4	8.7	(15)	1477.8
15643.052	(201)	1.1	11.8	(15)	1472.0
15716.813	(125)	1.1	7.6	(8)	626.4
16660.240	(63)	1.0	4.3	(4)	1221.2

energetic threshold is indicated as critical as these ions are not detected and the critical lifetime according to the possible critical decay pathways are given in Tab. E.2 also. The time-consuming analysis of the fastest total decay paths via several intermediate states is not done, as already the fastest single decay path is more than an order of magnitude slower than the collision time constant for collisions with Ar reactant gas.

Because the reaction H_3^+ + Ar proceeds with a faster time constant (0.4 ms^{-1}) than the effective lifetime of the upper state, it is well reasonable to assume that the chemical reaction H_3^+ + Ar occurs predominantly with the specific laser excited state of H_3^+ and only to a minor extent with subsequent radiatively decayed states.

Glossary

CNPI group A Complete nuclear permutation inversion group (CNPI) consists of all permutations of identical nuclei, the inversion E^*, and the product of E^* with all permutations of identical nuclei. It is a symmetry group of the molecule. 125

hot band transition A transition starting from any vibrational excited state. 47

Langevin rate reaction rate for ion-neutral reactions without potential barriers other than a centrifugal energy barrier. See App. E. 6, 16

MS group In the case of H_3^+ the molecular symmetry (MS) group is isomorphic to its point group and it is labeled $D_{3h}(M)$. 125

period A trap operation period is defined as the time between cooling down and warming up of the 22-pole trap. 83

spectroscopic accuracy for *ab initio* calculations the term spectroscopic accuracy means that energy levels are precise to $0.1\,cm^{-1}$. That is more than a magnitude worse than high resolution spectroscopic measurements provides.. 1, 31, 78

Bibliography

[1] J. Laane, ed., *Frontiers of Molecular Spectroscopy* (Elsevier, 2009).

[2] J. J. Thomson, Philosophical Magazine **21**, 225 (1911).

[3] J. J. Thomson, Philosophical Magazine **24**, 209 (1912).

[4] Discussion meeting of the Royal Society organized and edited by E. Herbst, S. Miller, T. Oka and J. K. G. Watson, Philos. Trans. R. Soc. London A 358, 2363 (2000).

[5] Discussion meeting of the Royal Society organized and edited by T. R. Geballe, D. Gerlich, J. Tennyson and T. Oka, Philos. Trans. R. Soc. London A 364, 2847 (2006).

[6] A. Alijah, submitted to Journal of Molecular Spectroscopy (2010).

[7] A. J. Dempster, Philosophical Magazine Series 6 **31**, 438 (1916).

[8] T. R. Hogness and E. G. Lunn, Physical Review **26**, 44 (1925).

[9] H. C. Urey, F. G. Brickwedde, and G. M. Murphy, Physical Review **39**, 164 (1932).

[10] J. J. Thomson, Nature **133**, 280 (1934).

[11] J. Hirschfelder, H. Eyring, and N. Rosen, The Journal of Chemical Physics **4**, 121 (1936).

[12] J. Hirschfelder, H. Eyring, and N. Rosen, The Journal of Chemical Physics **4**, 130 (1936).

[13] J. Hirschfelder, H. Diamond, and H. Eyring, The Journal of Chemical Physics **5**, 695 (1937).

[14] D. Stevenson and J. Hirschfelder, The Journal of Chemical Physics **5**, 933 (1937).

[15] J. O. Hirschfelder, The Journal of Chemical Physics **6**, 795 (1938).

[16] D. W. Martin, E. W. McDaniel, and M. L. Meeks, The Astrophysical Journal **134**, 1012 (1961).

[17] J. T. Hougen, The Journal of Chemical Physics **37**, 1433 (1962).

[18] J. T. Hougen, The Journal of Chemical Physics **39**, 358 (1963).

[19] J. K. G. Watson, Journal of Molecular Spectroscopy **103**, 350 (1984).

[20] R. E. Christoffersen, The Journal of Chemical Physics **41**, 960 (1964).

[21] M. Gaillard, D. Gemmell, G. Goldring, I. Levine, W. Pietsch, J. Poizat, A. Ratkowski, J. Remillieux, Z. Vager, and B. Zabransky, Physical Review A **17**, 1797 (1978).

[22] U. Galster, P. Kaminski, M. Beckert, H. Helm, and U. Müller, The European Physical Journal D **17**, 12 (2001).

[23] G. D. Carney and R. N. Porter, The Journal of Chemical Physics **65**, 3547 (1976).

[24] T. Oka, Physical Review Letters **45**, 531 (1980).

[25] W. Meyer, P. Botschwina, and P. Burton, The Journal of Chemical Physics **84**, 891 (1986).

[26] M. G. Bawendi, B. D. Rehfuss, and T. Oka, The Journal of Chemical Physics **93**, 6200 (1990).

[27] W. A. Majewski, P. A. Feldman, J. K. G. Watson, S. Miller, and J. Tennyson, Astrophys. J. Lett. **347**, L51 (1989).

[28] L.-W. Xu, M. Rösslein, C. M. Gabrys, and T. Oka, Journal of Molecular Spectroscopy **153**, 726 (1992).

[29] C. Lindsay and B. J. McCall, Journal of Molecular Spectroscopy **210**, 60 (2001).

[30] J. L. Gottfried, B. J. McCall, and T. Oka, The Journal of Chemical Physics **118**, 10890 (2003).

[31] C. P. Morong, J. L. Gottfried, and T. Oka, Journal of Molecular Spectroscopy **255**, 13 (2009).

[32] H. Kreckel, D. Bing, S. Reinhardt, A. Petrignani, M. Berg, and A. Wolf, The Journal of Chemical Physics **129**, 164312 (2008).

[33] R. Röhse, W. Kutzelnigg, R. Jaquet, and W. Klopper, The Journal of Chemical Physics **101**, 2231 (1994).

[34] A. Alijah, private communication.

[35] J. Tennyson and B. T. Sutcliffe, Molecular Physics: An International Journal at the Interface Between Chemistry and Physics **51**, 887 (1984).

[36] P. Schiffels, A. Alijah, and J. Hinze, Molecular Physics: An International Journal at the Interface Between Chemistry and Physics **101**, 189 (2003).

[37] F. Pan and T. Oka, The Astrophysical Journal **305**, 518 (1986).

[38] S. Miller and J. Tennyson, The Astrophysical Journal **335**, 486 (1988).

[39] P. J. Philip R. Bunker, *Molecular Symmetry and Spectroscopy* (NRC Research Press, Ottawa, 1998).

[40] I. R. McNab, Advances in Chemical Physics **LXXXIX** (1995).

[41] G. Herzberg, *Molecular Spectra and Molecular Structure*, vol. II (Krieger, Malabar, Florida, 1991).

[42] P. J. Philip R. Bunker, *Fundamentals of molecular symmetry* (Institut of Physics Publishing, 2005).

[43] B. J. McCall, Ph.D. thesis, University of Chicago (2001).

[44] *The cologne database for molecular spectroscopy*, http://www.cdms.de/.

[45] E. Herbst and W. Klemperer, Astrophysical Journal **185**, 505 (1973).

[46] E. P. Hunter, *NIST Chemistry WebBook, NIST Standard Reference Database Number 69* (P.J. Linstrom and W.G. Mallard, 2010).

[47] D. R. Flower, Journal of Physics B: Atomic, Molecular and Optical Physics p. 2319 (1989).

[48] M. Larsson and A. E. Orel, *Dissociative recombination of molecular ions* (University Press, Cambridge, 2008).

[49] M. Larsson, B. McCall, and A. Orel, Chemical Physics Letters **462**, 145 (2008).

[50] B. A. Tom, V. Zhaunerchyk, M. B. Wiczer, A. A. Mills, K. N. Crabtree, M. Kaminska, W. D. Geppert, M. Hamberg, M. af Ugglas, E. Vigren, et al., The Journal of Chemical Physics **130**, 031101 (2009).

[51] A. Petrignani, S. Altevogt, M. H. Berg, D. Bing, M. Grieser, J. Hoffman, B. Jordan-Thaden, C. Krantz, M. Mendes, O. Novotny, et al., arXiv:1012.1441v1.

[52] T. Millar, Space Science Reviews **106**, 73 (2003).

[53] quoted in: G. Handler and J. R. Arnold, J. Chem. Phys., 27, 144 (1957).

[54] A. Carrington, J. Buttenshaw, and R. Kennedy, Molecular Physics: An International Journal at the Interface Between Chemistry and Physics **45**, 753 (1982).

[55] A. Carrington and R. A. Kennedy, The Journal of Chemical Physics **81**, 91 (1984).

[56] A. Carrington and I. R. McNab, Accounts of Chemical Research **22**, 218 (1989).

[57] N. J. Murrell and S. D. Bosanac, *Introduction to the Theory of Atomic and Molecular Collisisions* (John Wiley & Sons Ltd, 1989), chap. 5.

[58] C. Schlier and U. Vix, Chemical Physics **95**, 401 (1985).

[59] A. Carrington, I. R. McNab, and Y. D. West, The Journal of Chemical Physics **98**, 1073 (1993).

[60] C. R. L. Sueur, J. R. Henderson, and J. Tennyson, Chemical Physics Letters **206**, 429 (1993).

[61] J. Tennyson, Reports on Progress in Physics **58**, 421 (1995).

[62] J. J. Munro, J. Ramanlal, and J. Tennyson, New Journal of Physics **7**, 196 (2005).

[63] B. C. Silva, P. Barletta, J. J. Munro, and J. f, The Journal of Chemical Physics **128**, 244312 (2008).

[64] M. Berblinger, E. Pollak, and C. Schlier, The Journal of Chemical Physics **88**, 5643 (1988).

[65] M. Berblinger, C. Schlier, and E. Pollak, The Journal of Physical Chemistry **93**, 2319 (1989).

[66] J. M. G. Llorente and E. Pollak, The Journal of Chemical Physics **89**, 1195 (1988).

[67] J. M. G. Llorente and E. Pollak, The Journal of Chemical Physics **90**, 5406 (1989).

[68] E. Pollak and C. Schlier, Accounts of Chemical Research **22**, 223 (1989).

[69] P. Drossart, J. Maillard, J. Caldwell, S. J. Kim, J. K. G. Watson, W. A. Majewski, J. Tennyson, S. Miller, S. K. Atreya, J. T. Clarke, et al., Nature **340**, 539 (1989).

[70] E. Pollak, The Journal of Chemical Physics **86**, 1645 (1987).

[71] S. Miller and J. Tennyson, Chemical Physics Letters **145**, 117 (1988).

[72] J. J. Munro, J. Ramanlal, J. Tennyson, and H. Y. Mussa, Molecular Physics: An International Journal at the Interface Between Chemistry and Physics **104**, 115 (2006).

[73] N. J. Wright and J. M. Hutson, The Journal of Chemical Physics **112**, 3214 (2000).

[74] J. R. Henderson, H. A. Lam, and J. Tennyson, Journal of the Chemical Society, Faraday Transactions **88**, 3287 (1992).

[75] P. D. Chowdary and M. Gruebele, Physical Review Letters **101**, 250603 (2008).

[76] P. D. Chowdary and M. Gruebele, The Journal of Chemical Physics **130**, 024305 (2009).

[77] P. A. M. Dirac, Proceedings of the Royal Society of London. Series A, Containing Papers of a Mathematical and Physical Character **123**, 714 (1929).

[78] J. C. D. E. B. Wilson Jr. and P. C. Cross, *Molecular Vibrations: The Theory of Infrared and Raman Vibrational Spectra* (Dover, 1980).

[79] C. H. Townes and A. L. Schawlow, *Microwave Spectroscopy* (McGraw-Hill, 1955).

[80] J. Tennyson, Journal of the Chemical Society, Faraday Transactions **88**, 3271 (1992).

[81] W. Demtröder, *Molekülphysik* (Oldenburg Wissenschaftsverlag, 2003).

[82] G. E. Moore, Electronics (1965).

[83] P. Bartlett and B. J. Howard, Molecular Physics **70**, 1001 (1990).

[84] B. R. Johnson, The Journal of Chemical Physics **79**, 1916 (1938).

[85] L. Wolniewicz and J. Hinze, The Journal of Chemical Physics **101**, 9817 (1994).

[86] A. Alijah, J. Hinze, and L. Wolniewicz, Ber. Bunsenges. Phys. Chem. **99**, 251 (1995).

[87] J. K. G. Watson, Philosophical Transactions: Mathematical, Physical and Engineering Sciences **358**, 2371 (2000).

[88] L. Neale, S. Miller, and J. Tennyson, Astrophysical Journal **464**, 516 (1996).

[89] B. M. Dinelli, L. Neale, O. L. Polyansky, and J. Tennyson, Journal of Molecular Spectroscopy **181**, 142 (1997).

[90] J. Tennyson, private communication.

[91] W. Cencek, J. Rychlewski, R. Jaquet, and W. Kutzelnigg, The Journal of Chemical Physics **108**, 2831 (1998).

[92] B. M. Dinelli, O. L. Polyansky, and J. Tennyson, The Journal of Chemical Physics **103**, 10433 (1995).

[93] A. Alijah, L. Wolniewicz, and J. Hinze, Molecular Physics: An International Journal at the Interface Between Chemistry and Physics **85**, 1125 (1995).

[94] L. P. Viegas, A. Alijah, and A. J. C. Varandas, The Journal of Chemical Physics **126**, 074309 (2007).

[95] D. Gerlich, Physica Scripta **T59**, 256 (1995).

[96] D. Gerlich and M. Smith, Physica Scripta **73**, C25 (2006).

[97] S. Trippel, J. Mikosch, R. Berhane, R. Otto, M. Weidemüller, and R. Wester, Physical Review Letters **97**, 193003 (2006).

[98] A. Svendsen, U. J. Lorenz, O. V. Boyarkin, and T. R. Rizzo, Rev. Sci. Instrum. **81** (2010).

[99] M. Guidi, Ph.D. thesis, Ecole polytechnique fédérale de Lausanne (2010).

[100] H. Kreckel, Ph.D. thesis, Ruprecht Karls Universität Heidelberg (2003).

[101] J. Mikosch, H. Kreckel, R. Wester, R. Plasil, J. Glosik, D. Gerlich, D. Schwalm, and A. Wolf, The Journal of Chemical Physics **121**, 11030 (2004).

[102] M. Berg, *Diplomarbeit* (2007).

[103] R. Disch, *Diplomarbeit* (1987).

[104] D. Gerlich, Journal of Analytical Atomic Spectrometry **19**, 581 (2004).

[105] E. Teloy and D. Gerlich, Chemical Physics **4**, 417 (1974).

[106] D. Gerlich, *The study of cold collisions using ion guides and traps* (World Scientific Publishing, 2008), chap. 3.

[107] M. E. Gehm, *Properties of* ^{6}*li*, The current version of the document is available at http://www.phy.duke.edu/research/photon/qoptics/techdocs (2003).

[108] S. Schlemmer, T. Kuhn, E. Lescop, and D. Gerlich, International Journal of Mass Spectrometry **185-187**, 589 (1999).

[109] O. Asvany and S. Schlemmer, International Journal of Mass Spectrometry **279**, 147 (2009).

[110] F. Pobell, *Matter and Methods at Low Temperatures* (Springer, 1996).

[111] H. Kreckel, M. Motsch, J. Mikosch, J. Glosik, R. Plasil, S. Altevogt, V. Andrianarijaona, H. Buhr, J. Hoffmann, L. Lammich, et al., Physical Review Letters **95**, 263201 (2005).

[112] A. Petrignani, H. Kreckel, M. H. Berg, S. Altevogt, D. Bing, H. Buhr, M. Froese, M. Grieser, J. Hoffmann, B. Jordan-Thaden, et al., Journal of Physics: Conference Series **192**, 012022 (2009).

[113] T. M. Sorg, *Ion counting and imaging methods for experiments with stored and trapped ions* (2008).

[114] H. Kreckel, O. Novotny, K. N. Crabtree, H. Buhr, A. Petrignani, B. A. Tom, R. D. Thomas, M. H. Berg, D. Bing, M. Grieser, et al., Physical Review A **82**, 042715 (2010).

[115] K. Jousten, ed., *Handbook of Vacuum Technology* (WILEY-VCH, 2008).

[116] J. L. Gottfried, Ph.D. thesis, University of Chicago (2005).

[117] J. L. Gottfried, Philosophical Transactions of the Royal Society A: Mathematical, Physical and Engineering Sciences **364**, 2917 (2006).

[118] W. Kolos and L. Wolniewicz, Reviews of Modern Physics **35**, 473 (1963).

[119] L. Wolniewicz, The Journal of Chemical Physics **103**, 1792 (1995).

[120] A. Alijah, D. Andrae, and J. Hinze, Theoretical Chemistry Accounts: Theory, Computation, and Modeling (Theoretica Chimica Acta) **127**, 149 (2008).

[121] B. F. Ventrudo, D. T. Cassidy, Z. Y. Guo, S. Joo, S. S. Lee, and T. Oka, The Journal of Chemical Physics **100**, 6263 (1994).

[122] R. A. Bachorz, W. Cencek, R. Jaquet, and J. Komasa, The Journal of Chemical Physics **131**, 024105 (2009).

[123] R. Jaquet, Theoretical Chemistry Accounts: Theory, Computation, and Modeling (Theoretica Chimica Acta) p. 157 (2010).

[124] E. Hugo, O. Asvany, and S. Schlemmer, The Journal of Chemical Physics **130**, 164302 (2009).

[125] A. Petrignani, D. Bing, O. Novotny, M. H. Berg, H. Buhr, M. Grieser, C. K. B. Jordan-Thaden, M. B. Mendes, S. Menk, D. A. O. S. Novotny, et al., J. Phys. Chem. A **114**, 4864 (2010).

[126] D. Bing, Ph.D. thesis, Universität Heidelberg (2010).

[127] T. Sochi and J. Tennyson, arXiv: 1002.2073 (2010).

[128] T. Oka, *Laser Spectroscopy V* (Springer-Verlag, 1981), p. 320.

[129] J. K. G. Watson, S. C. Foster, A. R. W. McKellar, P. Bernath, T. Amano, F. S. Pan, M. W. Crofton, R. S. Altman, and T. Oka, Can. J. Phys. **62**, 84 (1984).

[130] W. A. Majewski, M. D. Marshall, A. R. W. McKellar, J. W. C. Johns, and J. K. G. Watson, Journal of Molecular Spectroscopy **122**, 341 (1987).

[131] C. M. G. Li-Wei Xu and T. Oka, **93**, 6210 (1990).

[132] T. Nakanaga, F. Ito, K. Sugawara, H. Takeo, and C. Matsumura, Chemical Physics Letters **169**, 269 (1990).

[133] S. S. Lee, B. F. Ventrudo, D. T. Cassidy, T. Oka, S. Miller, and J. Tennyson, **145**, 222 (1991).

[134] F. Engelke, *Afbau der Moleküle* (Teubner Studienbücher, 1995).

Selbständigkeitserklärung

Ich versichere, dass ich die von mir vorgelegte Dissertation selbständig angefertigt, die benutzten Quellen und Hilfsmittel vollständig angegeben und die Stellen der Arbeit - einschließlich Tabellen, Karten und Abbildungen-, die anderen Werken im Wortlaut oder dem Sinn nach entnommen sind, in jedem Einzelfall als Entlehnung kenntlich gemacht habe; dass diese Dissertation noch keiner anderen Fakultät oder Universität zur Prüfung vorgelegen hat; dass sie - abgesehen von unten angegebenen Teilpublikationen - noch nicht veröffentlicht worden ist sowie, dass ich eine solche Veröffentlichung vor Abschluss des Promotionsverfahrens nicht vornehmen werde. Die Bestimmungen der Promotionsordnung sind mir bekannt. Die von mir vorgelegte Dissertation ist von Herrn Prof. Dr. Stephan Schlemmer betreut worden.